

UCSF

UC San Francisco Electronic Theses and Dissertations

Title

The vascular contribution to gradient-echo BOLD fMRI

Permalink

<https://escholarship.org/uc/item/8kg9h578>

Author

Vu, An Thanh

Publication Date

2011

Peer reviewed|Thesis/dissertation

The vascular contribution to gradient-echo BOLD fMRI

by

An Thanh Vu

DISSERTATION

Submitted in partial satisfaction of the requirements for the degree of

DOCTOR OF PHILOSOPHY

in

Bioengineering

in the

GRADUATE DIVISION

of the

UNIVERSITY OF CALIFORNIA, SAN FRANCISCO

AND

UNIVERSITY OF CALIFORNIA, BERKELEY

Acknowledgments

This dissertation is the result of the incredible kindness, patience, and support of many many people. Luckily there appears to be no page limit for acknowledgements so I'll try to include everyone. First and foremost, thanks to my research advisor Jack Gallant. His ability to imbue his students with his incredible work ethic, scientific standard and desire for the highest quality data is an honor to have experienced. Much of his time, patience, frustration, and effort goes into serving his students with their best interests in mind. I feel very fortunate to have had the opportunity to join the Gallant Lab. I'd like to also thank the present and former members of the Gallant Lab. Kendrick Kay for his mentorship on fMRI data collection/analysis and inspiration as a scientific writer (and of course for his daughter's baked goods!). Ryan Prenger and Michael Wu for their discussions on statistics, life, and graduation. Thomas Naselaris and Shinji Nishimoto for their collaborations on several projects and discussions on how to be a scientist and survive in the Gallant Lab. Tolga Cukur for his help on MR physics, numerous comments on this dissertation, and help with coding up the best fMRI pulse sequences ever! Alex Huth for numerous discussions on projects/analysis, willingness to scan at odd hours and for never hesitating to pointing out my errors. Michael Oliver for numerous discussions on regression and maintenance of Matlab/STRFlab. James Gao for his crucial service as lab administrator and source of technological information. Natalia Bilenko for her comments on this dissertation, help with brain segmentation and incredibly delicious baked goods. Dustin Stansbury for helping me with my mentoring skills and conference poster presentations.

Of course, none of this would be possible without the Berkeley Imaging Center staff. Thanks to Ben Inglis for his mentorship and support of the scanner. Daniel Sheltraw for help and encouragement on pulse sequence improvements. Miguel Perez and Rick Redfern for making sure the stimuli could be presented properly and conveniently to subjects. Mike Trumpis for his encouragement to study parallel imaging and Python as well as helping with reconstructing both phase and magnitude components from the 4 Tesla scanner using Recon Tools. Without his help, this dissertation would definitely not be possible.

Thanks to my thesis committee: Michael Silver and Adam Gazzaley. Their patience and flexibility in scheduling meetings as well as their advice on my projects really helped make graduation a smooth process. Thanks to the Joint Graduate Group in Bioengineering for making such a great program. Especially my graduate advisor Christoph Schreiner for making sure my requirements were met and whose appreciation for engineers in neuroscience encouraged me to join the program in the first place. Steve Conolly for inspiring me with MRI, helping sort out my future career goals, and also being a good mentor. SarahJane Taylor and Rebecca Pauling for all their administrative support from class enrollment reminders to setting up graduate group events. Also thanks to the National Science Foundation for funding the majority of my time as a PhD student. Without their funding, I may not have been able to pursue the great projects in this dissertation.

I also want to thank a few teachers in my past for inspiring me to be the scientist I am today. Eugene Cassvan – my Milpitas High School honors chemistry teacher who

taught me that making connections is key to mastering any subject. Henri Krutten, Rita Korsunsky, Lam Le for inspiring me to both enjoy and excel in math. Charles Schletzbaum for inspiring me to enjoy and excel in physics. Kathy Conradson and John Ribovich for inspiring me to enjoy and be reasonably proficient in English. Without the skills taught to me by these teachers this dissertation would not be possible. I'd also like to thank my legendary statistics professors: David Freedman and Stanton Glantz. Without them none of the p-values in this thesis would be significant.

Special thanks goes to my parents: Anh Quoc Vu and Betsey Elizabeth Vu. Without their encouragement, high standards and genes I would not be who I am today. And to all my siblings, family and friends for their patience and support during this long process.

Most of all, thanks to my loving wife: Chunli Ding Vu (Lily). Her patience, understanding, love, encouragement and experience with her own PhD enabled me to finish this dissertation in record time. Finally, to my future daughter to whom this dissertation is dedicated: thanks for waiting for me to finish.

Abstract

The vascular contribution to gradient-echo BOLD fMRI

by

An Thanh Vu

Joint Doctor of Philosophy

with the University of California, San Francisco

in Bioengineering

University of California, Berkeley

Professor Jack L. Gallant, Chair

Gradient-echo blood oxygen level dependent functional magnetic resonance imaging (BOLD fMRI) is one of the most powerful and widely used tools for studying neural processing in the human brain. However, BOLD fMRI is limited to measuring neural activity indirectly through blood oxygen concentration and is heavily biased toward large draining veins. Although this large vein bias is often ignored when interpreting results of BOLD fMRI experiments, it can lead to inaccurate estimates of the strength, location, and cortical extent of underlying neural activity. In this dissertation, novel methods utilizing the entire complex-valued BOLD signal are proposed. These methods provide robust localization of large veins and quantification of large vein contributions to studies using gradient-echo BOLD fMRI.

The BOLD fMRI signal is complex-valued consisting of both magnitude and phase components. Although most experiments using BOLD fMRI only analyze the

magnitude component, the phase component exhibits BOLD activity exclusively from large veins. Thus the phase component can either be used to enhance or suppress BOLD activity from large veins. The work here demonstrates that by using the phase component to enhance magnitude component BOLD activity, functional signal-to-noise ratio (fSNR) is improved equivalent to collecting 115% more data. This improvement is expected to increase at higher field strengths and spatial resolutions. By using the phase component to suppress large vein contributions, it is found that current understanding of semantic category representation may actually reflect vascular differences rather than neural differences across cortex. By suppressing large vein contributions using the methods proposed here, gradient-echo BOLD fMRI can more closely reflect underlying neural activity.

Table of Contents

Chapter 1. Background	
1. Fundamentals of magnetic resonance imaging	1
2. BOLD functional magnetic resonance imaging	16
3. Complex-valued magnetic resonance imaging	28
Chapter 2: Long echo time tri-segment phase transformation in magnetic resonance venography	
1. Background	38
2. Methods	44
3. Results	48
4. Discussion	55
Chapter 3: Combining phase and magnitude information for improved source localization in complex-valued fMRI	
1. Background	68
2. Methods	73
3. Results	77
4. Discussion	86
Chapter 4: The vascular contribution to object area localization in BOLD fMRI	
1. Background	95
2. Large vein suppression methods	97
3. Computer simulation study	102
4. FFA/PPA localization study	109

5. Results	114
6. Discussion	120
Appendices	
A.1 Susceptibility weighted venography theory	124
A.2 T2* Magnitude Contrast Optimization - TE_{opt}	126
A.3 Optimal weighting of magnitude and phase	127
References	129

List of Tables

Table 2.1 Contrast properties of venous blood and gray matter	39
---	----

List of Figures

Figure 1.1 Inducing magnetization vector \mathbf{m}	3
Figure 1.2 Spatially non-selective excitation	5
Figure 1.3 Slice selective excitation	6
Figure 1.4 Precession and relaxation	7
Figure 1.5 Encoding spatial position with precession frequency	9
Figure 1.6 Fourier relationship between k -space and image space	11
Figure 1.7 2DFT coverage of k -space	15
Figure 1.8 Biophysical source of venous susceptibility gradients	18
Figure 1.9 T2* contrast as a function of echo time	19
Figure 1.10 Venous susceptibility distribution	23
Figure 1.11 2DFT gradient-echo and spin-echo sequences	24
Figure 1.12 Refocusing transverse magnetization with spin-echo	27
Figure 1.13 Echo planar trajectory	28
Figure 1.14 Axial slice of complex-valued MRI volume	28
Figure 1.15 Spatial phase unwrapping	29
Figure 1.16 Homodyne filter algorithm for phase unwrapping	32
Figure 2.1 T2* contrast as a function of TE	40
Figure 2.2 Intravascular phase probability distributions	43

Figure 2.3 Phase transformations	44
Figure 2.4 Steps in susceptibility weighted venography	47
Figure 2.5 Phase transformation matching	48
Figure 2.6 Effect of extended TE on SWV	50
Figure 2.7 Cross section of vein near parallel with B_0	51
Figure 2.8 Effect of phase transformation on phase wrapping artifacts	54
Figure 2.9 Cross section of vein near perpendicular with B_0	55
Figure 2.10 Phase and magnitude as a function of TE	65
Figure 3.1 Coronal slice of complex-valued fMRI volume	69
Figure 3.2 Task-related phase and magnitude changes	69
Figure 3.3 Magnitude and phase fSNR as a function of voxel position	72
Figure 3.4 fSNR using one of four measures of BOLD activity	78
Figure 3.5 fSNR improvement relative to magnitude fSNR	80
Figure 3.6 Bias reduction using spamfMRI	85
Figure 3.7 Classification performance	86
Figure 4.1 Task-related phase and magnitude changes	98
Figure 4.2 Magnetic field off resonance distribution around a vein	99
Figure 4.3 Simulated large vein bias reduction with a large vein	105
Figure 4.4 Simulated large vein bias reduction without a large vein	106
Figure 4.5 Simulated large vein bias reduction adjacent to a large vein	107
Figure 4.6 Simulated large vein bias reduction as a function of fSNR	109
Figure 4.7 sPR t -values plotted against magnitude t -values	115

Figure 4.8 PPA t -values with and without large vein suppression	116
Figure 4.9 Quantification of large vein contributions to specific ROIs	117
Figure 4.10 ROI size, t -value and large vein contribution correlation	119
Figure 4.11 Hemisphere laterality with and without large vein suppression	119
Figure A.2.1 Frequency and phase spatial distributions around veins	125

Chapter 1: Background

Since its advent almost two decades ago, blood oxygen level dependent functional magnetic resonance imaging (BOLD fMRI) has advanced tremendously, becoming one of the most powerful and widely used tools for studying neural processing in the human brain. The work in this dissertation utilizes the complex-valued BOLD fMRI signal (both phase and magnitude components) to investigate the large vein contributions to gradient-echo BOLD fMRI. In order to best utilize the phase and magnitude components in this investigation we must first understand the fundamentals of BOLD fMRI. To accomplish this, the first section of this chapter reviews the fundamentals of magnetic resonance imaging (MRI) from the classical mechanics perspective (for treatment of MRI using quantum mechanics refer to Slichter, 1996 and Levitt, 2001). In this section, the idea of “ k -space” and how it can encode a complex-valued object is developed. The second section reviews the fundamentals of BOLD fMRI. In this section, the biophysical source of the complex-valued BOLD signal as well as basic pulse sequences used for collecting BOLD fMRI data are discussed. In the final section, current applications of complex-valued MRI as well as areas for improvement are presented.

1.1 Fundamentals of Magnetic Resonance Imaging

Magnetization vector \mathbf{m}

MRI measures the net magnetization vector \mathbf{m} at various spatial positions in a scanned object. This measurement is possible for all nuclei with an odd number of protons and/or neutrons (e.g. ^1H , ^{23}Na , and ^{31}P) because these nuclei have a non-zero

dipole magnetic moment μ . At thermal equilibrium, the magnetic moments are oriented randomly yielding no net magnetization (Fig 1.1A). However in the presence of a static magnetic field \mathbf{B}_0 , the magnetic moments tend to align with the field yielding the net magnetization vector $\mathbf{m} = \sum \mu$ (Fig 1.1B). In this way, the potential energy of the magnetic moment $E = -\mu \cdot \mathbf{B}_0$ is minimized (Fig 1.1C). The energy difference between the lowest energy orientation (μ parallel to \mathbf{B}_0) and the highest energy orientation (μ antiparallel to \mathbf{B}_0) is given by:

$$\Delta E = h \frac{\gamma}{2\pi} B_0 \quad [1.1]$$

where h is Plank's constant, γ is the gyromagnetic ratio specific to the nuclei scanned and B_0 is the strength of the magnetic field (Nishimura, 1996). The larger this energy difference is the more likely magnetic moments will align parallel to \mathbf{B}_0 . This is captured by the ratio of antiparallel (N_-) to parallel (N_+) magnetic moments given by the Boltzmann distribution:

$$\frac{N_-}{N_+} = e^{\frac{-\Delta E}{kT}} \approx 1 - \frac{\Delta E}{kT} \quad [1.2]$$

where k is Boltzmann's constant and T is temperature (Nishimura, 1996). The approximation in Eq [1.2] is possible because at body temperature $\Delta E/kT$ is close to zero (on the order of 10^{-5}). Following from Eqs [1.1-2] the net number of magnetic moments parallel to \mathbf{B}_0 is proportional to B_0 :

$$N_+ - N_- \propto \frac{h\gamma}{2\pi kT} B_0 \quad [1.3]$$

Thus, the size of the net magnetization vector \mathbf{m} is also proportional to the strength of the applied magnetic field \mathbf{B}_0 .

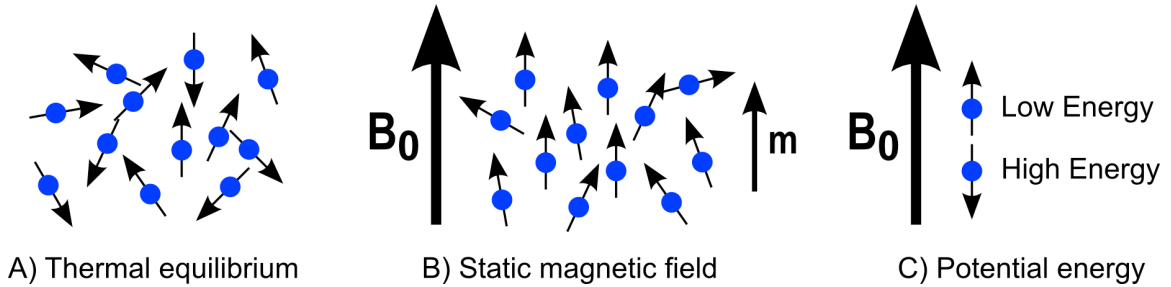


Figure 1.1. Inducing magnetization vector \mathbf{m} . A) Magnetic moments are oriented randomly at thermal equilibrium. B) When a static magnetic field is applied, a net magnetization vector \mathbf{m} is induced. C) The lowest energy orientation of a magnetic moment is parallel with \mathbf{B}_0 .

RF Excitation

Theoretically, magnetic resonance imaging (MRI) experiments could be done on the induced magnetization vector \mathbf{m} while it is parallel with \mathbf{B}_0 . In practice however, the amplitude of \mathbf{m} is on the order of one millionth the amplitude of \mathbf{B}_0 . Because of this, it is impractical to do MRI experiments on variations of \mathbf{m} while it is aligned with \mathbf{B}_0 . The solution to this problem is to tip \mathbf{m} away from \mathbf{B}_0 into the transverse (xy) plane (Fig 1.2). This is possible by applying another magnetic field, referred to as \mathbf{B}_1 , in the transverse plane. In general, the torque applied to the magnetization vector \mathbf{m} in the presence of a magnetic field \mathbf{B} can be expressed as:

$$\frac{d\mathbf{m}}{dt} = \mathbf{m} \times \gamma \mathbf{B} \quad [1.4]$$

This torque causes \mathbf{m} to precess around \mathbf{B}_1 such that it tips away from \mathbf{B}_0 at a rate of:

$$\omega = \gamma B_1 \text{ rad/s} \quad \text{or} \quad f = \frac{\gamma}{2\pi} B_1 \text{ Hz} \quad [1.5]$$

where B_1 is the strength of the applied \mathbf{B}_1 . The amount of tipping θ (also referred to as the flip angle) is then:

$$\theta = \int_0^t \omega(\tau) d\tau = \int_0^t \gamma B(\tau) d\tau \text{ rad} \quad [1.6]$$

where t is the duration \mathbf{B}_1 is applied. Thus, the amount of magnetization detectable in the transverse plane m_{xy} is $|\mathbf{m}|\sin(\theta)$.

The treatment of tipping \mathbf{m} away from \mathbf{B}_0 is accurate so far except for one thing. Once \mathbf{m} is no longer parallel with \mathbf{B}_0 , \mathbf{B}_0 also applies a torque on \mathbf{m} . This torque causes \mathbf{m} to precess about \mathbf{B}_0 (z-axis) at the Larmor frequency (also referred to as the resonance frequency):

$$\omega_0 = \gamma B_0 \text{ rad/s} \quad \text{or} \quad f_0 = \frac{\gamma}{2\pi} B_0 \text{ Hz} \quad [1.7]$$

To account for this, \mathbf{B}_1 can be applied such that it also rotates at the Larmor frequency. In this rotating frame of reference \mathbf{m} does not precess about the z-axis and \mathbf{B}_1 is always orthogonal to \mathbf{m} . In figures we denote this rotating frame of reference using x' and y' . For protons (H^1) in water molecules at a field strength of 3 Tesla, f_0 is roughly 128 MHz.

Thus, the applied rotating \mathbf{B}_1 field is often referred to as a radio frequency (RF) excitation

or RF pulse.

The constant amplitude RF pulse presented in Fig 1.2 is spatially non-selective and excites the magnetic moments in the entire volume scanned. By introducing a magnetic field gradient along the z-axis (G_z), we can excite a single slice (Fig 1.3). With G_z , precession frequency varies linearly with position along the z-axis. Thus, a specific slice can be excited with a sinc modulated RF pulse that excites a range of frequencies corresponding to the desired positions along the z-axis. Thinner slices can be achieved by increasing the strength of G_z (the slope of the field gradient) or by reducing the frequency bandwidth of the RF pulse.

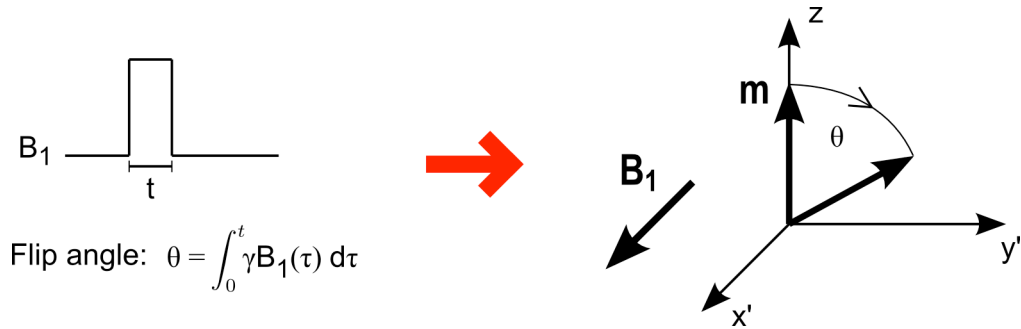


Figure 1.2. Spatially non-selective excitation. Excitation in general is achieved by applying a magnetic field B_1 orthogonal to the main magnetic field. Spatially non-selective excitation is achieved using a B_1 of constant strength and brief duration. The flip angle θ is proportional to the time integral of B_1 .

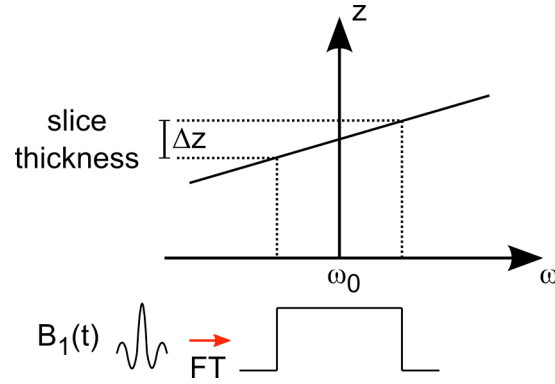


Figure 1.3. Slice selective excitation. Using G_z , precession frequency varies linearly with position along the z -axis. In the presence of G_z , applying an RF pulse that has a rectangular frequency profile excites a single slice. Increasing the strength of G_z or reducing the bandwidth of the RF pulse results in thinner slices.

Magnetization vector relaxation

Before RF excitation, the magnetization vector \mathbf{m} lies entirely along the z -axis and thus only has an m_z component. At equilibrium, the amplitude of \mathbf{m} and therefore m_z is denoted by m_0 . After RF excitation, m_z reduces to $m_0 \cos(\theta)$. But because the main magnetic field \mathbf{B}_0 is still present, m_z will recover back to m_0 at the rate of:

$$\frac{dm_z}{dt} = -\frac{m_z - m_0}{T1} \quad [1.8]$$

The solution to Eq [1.8] is an exponential recovery:

$$m_z(t) = m_0 + (m_z(0) - m_0) e^{-t/T1} \quad [1.9]$$

where $m_z(0)$ represents m_z right after excitation. Fig 1.4B shows the timecourse of m_z after \mathbf{m} has been completely tipped into the transverse plane ($\theta = 90^\circ$). This recovery is often referred to as T1 relaxation, longitudinal relaxation or spin-lattice relaxation. The relaxation constant T1 determines the rate at which m_z returns to thermal equilibrium.

The exact physical mechanisms behind T1 relaxation are quite complex and the interested reader is referred to more in-depth treatments of the subject (Slichter, 1996; Levitt, 2001). In practice, T1 is empirically determined for each tissue type and field strength of interest. At 3 Tesla, T1 values of protons in water molecules are typically around one second. T1 values tend to be larger and thus recovery tends to be slower at higher field strengths (Nishimura, 1996).

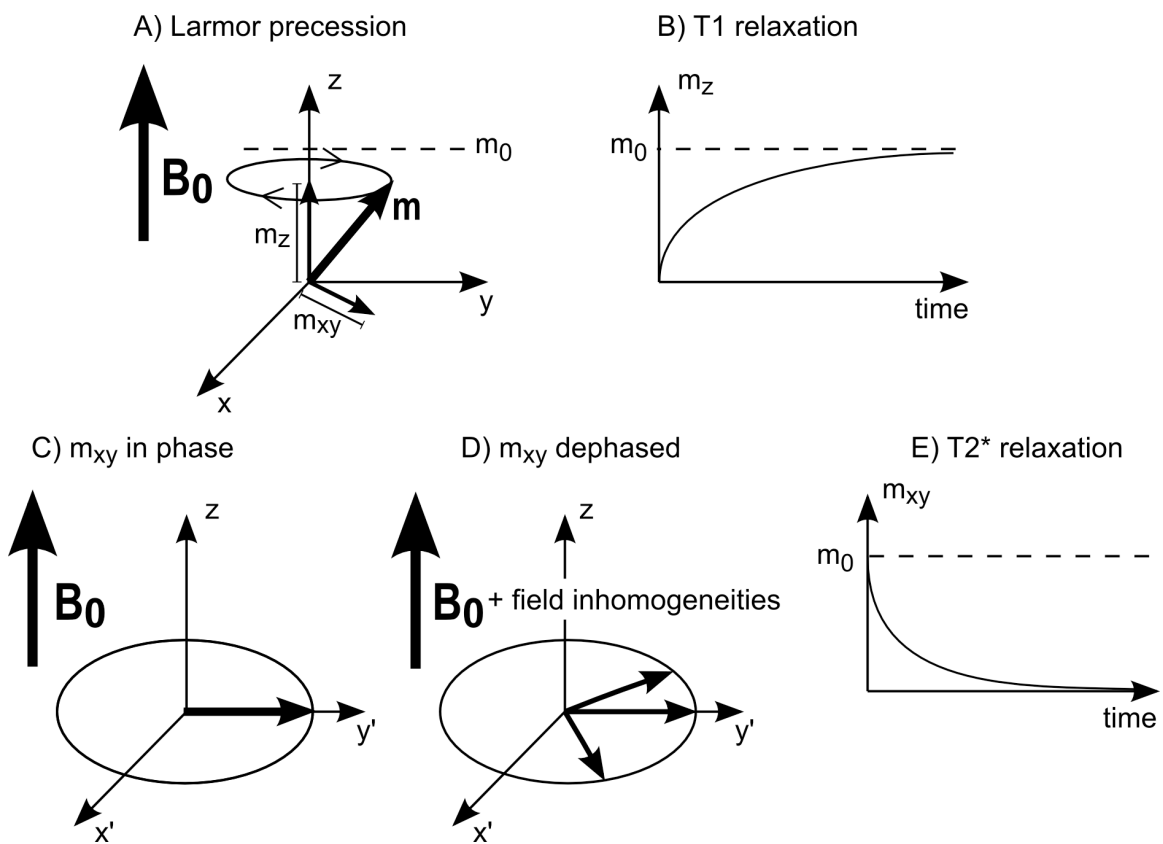


Figure 1.4. Precession and relaxation in the presence of main magnetic field B_0 pointing along the z-axis. A) When tipped away from the z-axis, the magnetization vector \mathbf{m} precesses about the z-axis. B) After being tipped away, the magnetization along the z-axis gradually returns to thermal equilibrium (T1 relaxation). C) After being tipped, the magnetization in the transverse plane (xy) is initially in phase. D) Due to local field inhomogeneities, different magnetization moments precess at slightly different

frequencies. This results in dephasing of the transverse magnetization over time. E) Due to this dephasing the transverse magnetization gradually returns to thermal equilibrium (T2* relaxation).

Tipping \mathbf{m} away from \mathbf{B}_0 also introduces a magnetization component in the transverse plane: m_{xy} . After excitation m_{xy} initially has a value of $m_0 \sin(\theta)$ but must also eventually return to thermal equilibrium ($m_{xy} = 0$). This form of relaxation can be interpreted as a dephasing phenomenon. Initially after excitation, the magnetic moments $\boldsymbol{\mu}$ that make up the magnetization vector \mathbf{m} are in phase pointing in the same direction as they precess around the z-axis (Fig 1.4C). However, due to magnetic field inhomogeneities within the excited volume, individual magnetic moments will precess at slightly different frequencies. This effectively divides m_{xy} into three components: one precessing faster, one precessing slower, and one precessing exactly at ω_0 (Fig 1.4D). Over time, these three components become increasingly out of phase resulting in m_{xy} decay. The rate of this decay is given by:

$$\frac{dm_{xy}}{dt} = -\frac{m_{xy}}{T2^*} \quad [1.10]$$

The solution to Eq [1.10] is an exponential decay:

$$m_{xy}(t) = m_{xy}(0) e^{-t/T2^*} \quad [1.11]$$

where $m_{xy}(0)$ represents m_{xy} right after excitation. This relaxation is referred to as T2* relaxation, T2* decay or transverse relaxation. T2* is a tissue specific exponential time constant related to both macroscopic and microscopic magnetic field inhomogeneities. At 3 Tesla, T2* values of protons in water molecules are typically on the order of tens of

milliseconds. $T2^*$ values tend to be smaller and thus m_{xy} decay tends to be faster at higher field strengths (Koopmans et al., 2008).

Combining the effects of precession (Eq [1.4]), T1 relaxation (Eq [1.8]), and T2* relaxation (Eq [1.10]) yields a complete description of the dynamics of the magnetization vector \mathbf{m} . This phenomenological description is known as the Bloch equation given by:

$$\frac{d\mathbf{m}}{dt} = \mathbf{m} \times \gamma \mathbf{B} - \frac{(m_z - m_0)\hat{z}}{T1} - \frac{m_x\hat{x} + m_y\hat{y}}{T2^*} \quad [1.12]$$

However, it should be noted that the exponential behavior of T1 and T2* are approximations. Chapter two of this dissertation touches on one example where the exponential approximation of T2* decay severely underestimates the benefit of optimal scan parameters in MR venography. It should also be noted that for conservation of energy T2* must be less than or equal to T1.

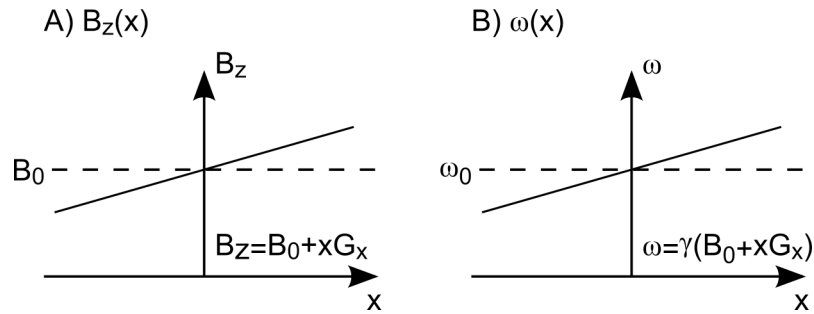


Figure 1.5. Encoding spatial position with precession frequency. A) Magnetic field as a function of spatial position in the presence of B_0 and a gradient field G_x . B) Precession frequency as a function of spatial position in the presence of B_0 and a gradient field G_x .

k-space representation

In MRI, only differences in the m_{xy} component of \mathbf{m} can be detected. Assuming a

slice has already been excited along the z-axis, the detected signal can be expressed as:

$$s(t) = \int_x \int_y m_{xy}(x, y, t) e^{-i\phi(x, y, t)} dx dy \quad [1.13]$$

where $\phi(x, y, t)$ is the phase of m_{xy} in the transverse plane. In general the phase of m_{xy} can be expressed as:

$$\phi(x, y, t) = \int_0^t \omega(x, y, \tau) d\tau = \gamma \int_0^t B(x, y, \tau) d\tau \quad [1.14]$$

Therefore, in the presence of the main magnetic field \mathbf{B}_0 , the signal equation becomes:

$$s(t) = e^{-i\omega_0 t} \int_x \int_y m_{xy}(x, y, t) dx dy \quad [1.15]$$

which is often demodulated to the baseband signal:

$$s_d(t) = \int_x \int_y m_{xy}(x, y, t) dx dy \quad [1.16]$$

Although the magnetization varies as a function of space according to the biological environment, the signal from Eq [1.16] does not preserve this spatial information. In order to preserve spatial information and create an image using MRI, magnetic field gradients are applied on top of the main magnetic field \mathbf{B}_0 . In doing so, the frequency of precession varies linearly as a function of space (Fig 1.5) and the baseband signal equation becomes:

$$s_d(t) = \int_x \int_y m_{xy}(x, y, t) e^{-i2\pi[k_x(t)x + k_y(t)y]} dx dy \quad [1.17]$$

where

$$k_x(t) = \frac{\gamma}{2\pi} \int_0^t G_x(\tau) d\tau \quad \text{and} \quad k_y(t) = \frac{\gamma}{2\pi} \int_0^t G_y(\tau) d\tau \quad . \quad [1.18]$$

Careful inspection of Eq [1.17] reveals that the baseband signal is actually M_{xy} , the 2D Fourier transform of m_{xy} :

$$s_d(t) = M_{xy}(k_x(t), k_y(t)) \quad [1.19]$$

with k_x and k_y in units of spatial frequency, typically cycles/cm. Thus, each sample of $s_d(t)$ is a sample of m_{xy} in Fourier space.

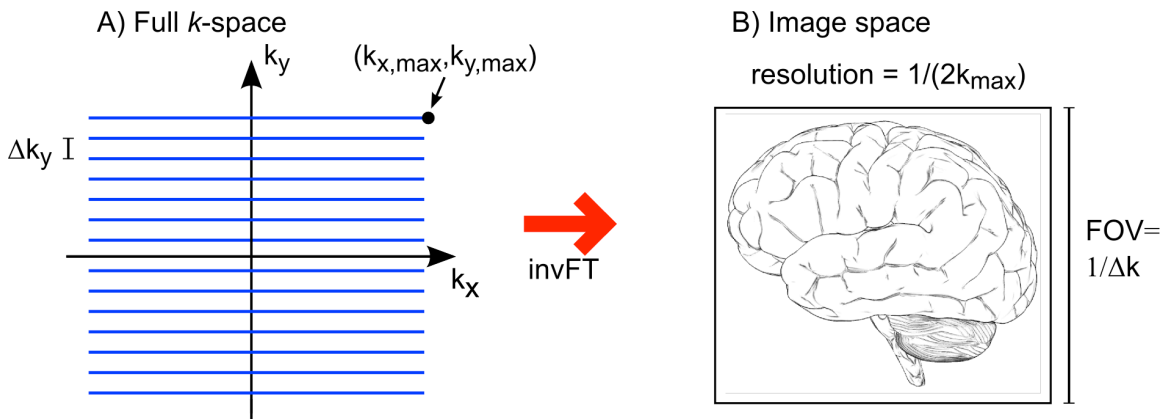


Figure 1.6. Fourier relationship between k -space and image space. A) An example of a full grid of k -space. B) The k -space data are inverse Fourier transformed to produce the image space representation of the scanned object. The field of view of the object in image space depends on how finely k -space is sampled. The resolution of the object in image space depends on the extent of k -space covered.

The 2D Fourier space in MRI is often called “ k -space” where k denotes the spatial frequency variable. From Eq [1.18], the position of k -space sampled depends on the strength and duration of the applied gradients G_x and G_y . By manipulating G_x and G_y to cover k -space, an image of the scanned object can be recovered using the inverse 2D

Fourier transform (Fig 1.6). For physical intuition, Fig 1.7 depicts the collection of one k -space line of an object with an m_{xy} value of one everywhere in a 1cm x 1cm square. At time point (1), immediately after RF excitation, the magnetization in the entire volume is in phase. This corresponds to the center of k -space and the baseband signal at this point is simply Eq [1.16]. At time point (2), midway through the negative lobe of G_x , the phase of m_{xy} along the x -axis has a spatial frequency of 0.5 cycles/cm. At time point (3), G_x is turned off and the phase of m_{xy} along the x -axis now has twice the spatial frequency it had at time point (2) (1 cycle/cm). At time point (4), the G_y gradient, often referred to as the phase encode gradient, has finished and the phase of m_{xy} has a spatial frequency of $\sqrt{2}$ cycles/cm along the $x+y$ axis. At this point, circuitry is activated to record the signal from the line of k -space (blue line). At time point (5), midway through positive lobe of G_x , the initial effects of the negative G_x lobe are rewound and the phase of m_{xy} is left with a spatial frequency of 1 cycle/cm along the y -axis. This time point, also known as the echo time (TE) is the time from excitation to the center of the k -space line. At time point (6), G_x is turned off and the phase of m_{xy} now has a spatial frequency of $\sqrt{2}$ cycles/cm along the $x-y$ axis. This is the same phase distribution as in time point (4) but reflected about the y -axis. The excitation, k -space traversal procedure described here is repeated until all the desired lines in k -space are collected. This method of sampling k -space is often referred to as 2DFT sampling.

From the above example, another way to view k -space becomes apparent. Each point in k -space can be thought of as the dot product between vectorized versions of m_{xy} and a filter with specific spatial frequency and orientation. Points further away from the

center of k -space are dot products of higher spatial frequency filters with m_{xy} . Using the Nyquist sampling criterion, the spatial resolution in image space is determined by the k -space points sampled farthest from the center (Fig 1.6):

$$\Delta x = \frac{1}{2 k_{x, max}} \quad \text{and} \quad \Delta y = \frac{1}{2 k_{y, max}} \quad . \quad [1.20]$$

Therefore to increase the spatial resolution in image space, $\frac{y}{2\pi} \int_0^t G(\tau) d\tau$ (Eq [1.18]) must also increase. In other words, spatial resolution is proportional to the area under the gradient timecourse curve (Fig 1.7A). Reciprocally, the maximum alias-free extent in image space or field of view (FOV) is proportional to the resolution at which k -space is sampled:

$$FOV_x = 2 x_{max} = \frac{1}{\Delta k_x} \quad \text{and} \quad FOV_y = 2 y_{max} = \frac{1}{\Delta k_y} \quad . \quad [1.21]$$

In practice, the resolution along the k_x -axis of k -space is only limited by the sampling rate of the ADC so FOV_x can be cropped arbitrarily without aliasing. However, the k_y -axis is sampled discretely (Fig 1.6A). In order to increase FOV_y while maintaining the same spatial resolution along the y -axis, the number of k -space lines collected must increase while the spacing between the lines must proportionately decrease. In practice, the FOV is set to be as large or larger than the object scanned to avoid aliasing. However, repeating the excitation k -space traversal procedure to scan the human brain at a reasonable resolution can take on the order of minutes. Part of the next section discusses another method of collecting k -space that reduces the scan time to just seconds.

So far it has been assumed that changes in the phase of m_{xy} are only due to the gradients G_x and G_y that we intentionally turn on. With this assumption, we expect the inverse Fourier transform of the collected k -space data to yield a real valued image of m_{xy} (Eqs [1.17, 19]). However, in practice unintentional magnetic field inhomogeneities will arise due to imperfect shimming or differences in magnetic susceptibility across tissue boundaries. These field inhomogeneities add an additional field term to Eq [1.14] and the baseband signal of Eq [1.17] becomes:

$$s_d(t) = \int_x \int_y |m_{xy}(x, y, t)| e^{-i\phi_{xy}(x, y, t)} e^{-i2\pi[k_x(t)x + k_y(t)y]} dx dy \quad [1.22]$$

where $\phi_{xy}(x, y, t)$ is the phase of m_{xy} due to field inhomogeneities other than those caused by G_x and G_y . This baseband signal is still the 2D Fourier transform of m_{xy} but now m_{xy} is complex-valued with phase $\phi_{xy}(x, y, t)$. For convenience, m_{xy} is often decomposed into real and imaginary components or expressed as a phasor:

$$m_{xy} = m_x + i m_y = |m_{xy}| e^{-i\phi_{xy}} \quad [1.23]$$

Thus, in general, MRI images are complex-valued with magnitude $|m_{xy}(x, y, t)|$ and phase $\phi_{xy}(x, y, t)$ components. Because field inhomogeneities from tissue susceptibility differences are tissue specific, the phase component of MRI images also contain tissue specific contrast (Ogg et al., 1999; Reichenbach et al., 2000; Hammond et al., 2008). The biophysical source of these spatial and temporal phase differences as well as their application is discussed in the remainder of this chapter.

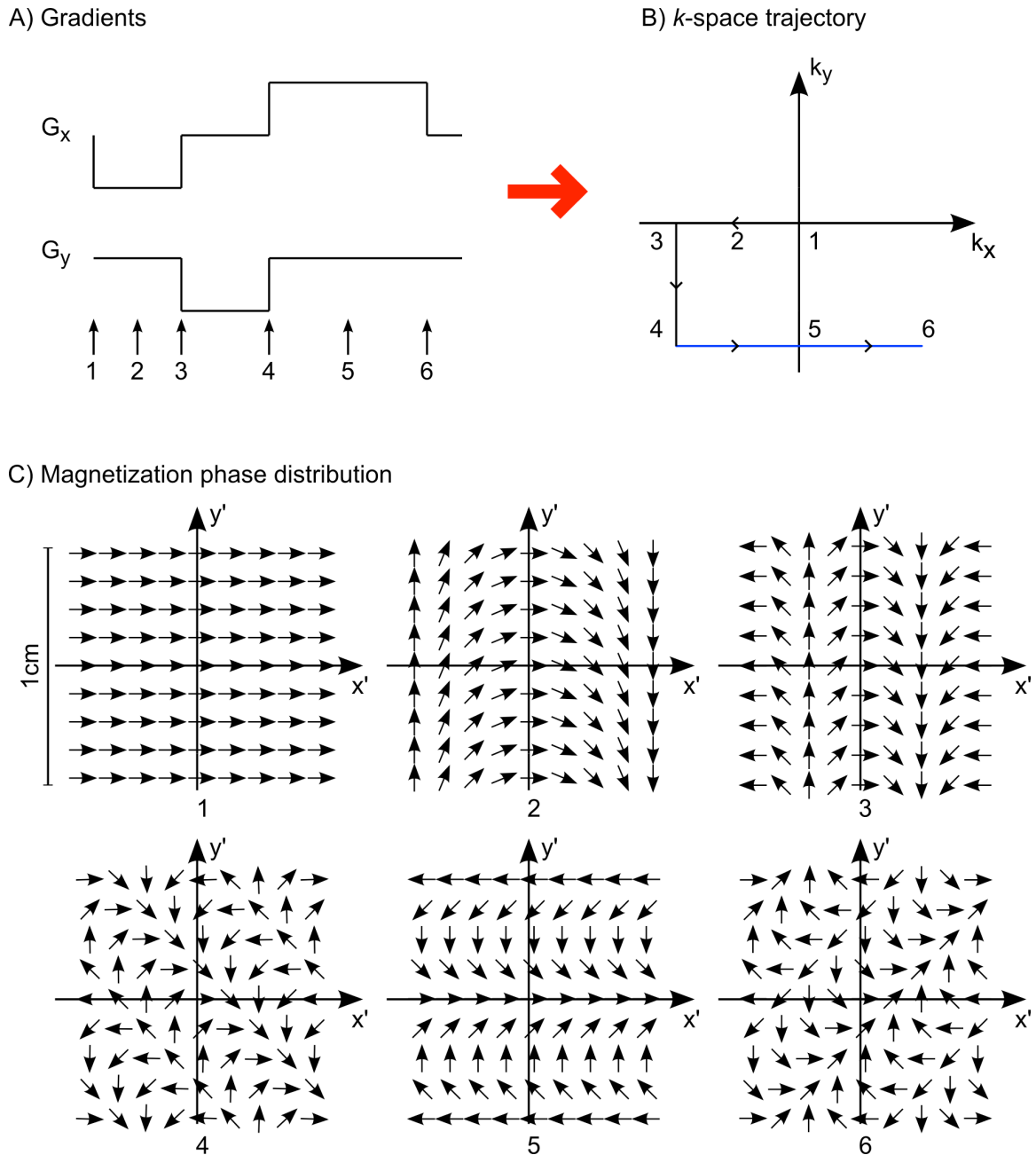


Figure 1.7. 2DFT coverage of k -space. A) Timecourse of x and y -gradients. B) Resulting k -space trajectory. To cover a grid of k -space, the gradient timecourses in (A) are repeated with the phase encode gradient G_y incrementally increased. C) Magnetization phase distribution corresponding to the six labeled time points. 1) Immediately after excitation all spins are in phase. 2) Midway through the negative lobe of G_x . 3) Just after G_x is turned off. 4) Just after the positive lobe of G_y is finished. After this time point, the detection circuitry is activated to acquire the k -space line (blue line in (B)). 5) Midway

through the positive lobe of G_x . 6) Just after the positive lobe of G_x is turned off.

1.2 BOLD Functional Magnetic Resonance Imaging

The previous section discussed how complex-valued m_{xy} is represented in k -space and converted back to image space. In practice the recovered m_{xy} is of a finite spatial resolution and is divided into discrete volumes referred to as voxels. The signal from a given voxel can be expressed as:

$$s_{\text{voxel}}(t) = \int_{\Delta x} \int_{\Delta y} \int_{\Delta z} |m_{xy}(x, y, z, t)| e^{-i\phi_{xy}(x, y, z, t)} dx dy dz \quad [1.24]$$

where Δx , Δy and Δz are the dimensions of the voxel. This section discusses the biophysical source of BOLD phase and magnitude changes in a given voxel. Common pulse sequences used to measure the BOLD signal are also discussed.

Due to field inhomogeneities within a voxel, the phase of magnetic moments that make up m_{xy} become increasingly out of phase. This dephasing results in $T2^*$ decay of the magnitude component of the voxel signal (Figs 1.4C-E). BOLD fMRI using the magnitude component of the voxel signal is possible because the strength of the inhomogeneities and thus the rate of $T2^*$ decay is different during baseline and activation states of neural activity. Fig 1.8 demonstrates the biophysical changes that occur during the activation state. At the baseline state, the concentration of deoxyhemoglobin in capillaries, venules, and veins is relatively high. During activation, the rate of oxygen metabolism increases and this signals the underlying blood vessels to expand (Fox and Raichle, 1986). This increases the flow of fully oxygenated blood into the capillary bed and results in a net reduction in deoxyhemoglobin concentration (Fox and Raichle, 1986;

Ogawa and Lee, 1990). Because the magnetic susceptibility of deoxyhemoglobin rich blood is different from surrounding tissue, in the presence of the main magnetic field \mathbf{B}_0 , field inhomogeneities arise (Ogawa and Lee, 1990; Ogawa et al., 1993). These inhomogeneities are often referred to as susceptibility gradients and are responsible for changes in the phase term in Eq [1.24] as well as the $T2^*$ decay in voxels containing capillaries, venules, and veins. The reduction in concentration of deoxyhemoglobin during the activation state reduces the strength of the susceptibility gradients which also results in slower $T2^*$ decay. Together, these changes yield larger magnitude signals during activation than baseline states in BOLD fMRI.

An example of this reduction in $T2^*$ decay for venous blood at 4 Tesla is shown in Fig 1.9. Voxel signal as a function of time after RF excitation is plotted for $T2^*$ values of 24ms (blue) and 41ms (green). These $T2^*$ values are typical for baseline and activation states of venous blood at 4T, respectively (Jezzard et al., 1996; Li et al., 1998). The signal difference between these two states, often referred to as $T2^*$ contrast, also varies as a function of time (red) and can be expressed as:

$$s_{a-b}(t) = m_{xy}(0) e^{-t/T2_a^*} - m_{xy}(0) e^{-t/T2_b^*} \quad [1.25]$$

where $m_{xy}(0)$ is the voxel signal immediately after RF excitation. $T2_a^*$ and $T2_b^*$ are the venous blood activation and baseline $T2^*$ values, respectively. Setting to zero the derivative of Eq [1.25] with respect to t and solving reveals that the peak signal difference between the two states occurs at a time between the two $T2^*$ values:

$$t = TE_{opt} = \ln \left(\frac{T2_b^*}{T2_a^*} \right) \left(\frac{1}{T2_a^*} - \frac{1}{T2_b^*} \right)^{-1} . \quad [1.26]$$

This time is referred to as the optimal echo time (TE_{opt}). This optimal time is denoted by the vertical black line in Fig 1.9.

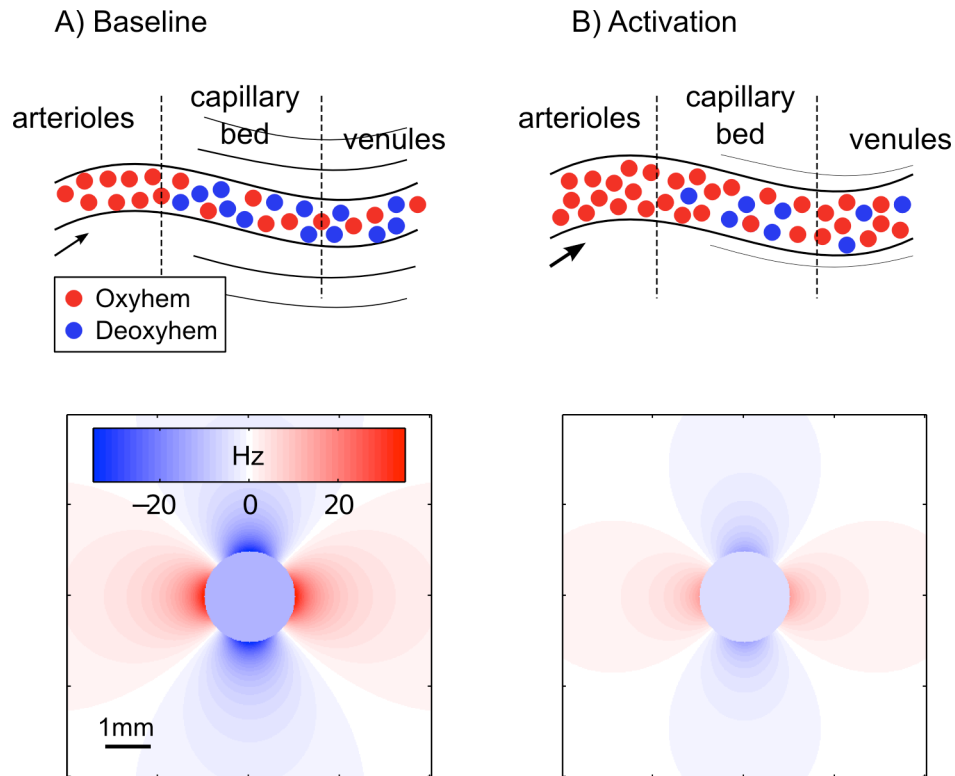


Figure 1.8. Biophysical source of venous susceptibility gradients. The first row shows the biophysical changes from baseline to activation states. The second row shows the susceptibility gradient distribution in the cross section of a vein during baseline and activation states. A) At baseline, the concentration of deoxyhemoglobin in the capillary bed, venules, and veins is relatively high. Because the strength of the susceptibility gradients is proportional to the concentration of deoxyhemoglobin, the susceptibility gradients during baseline are relatively strong. B) During activation, the vasculature expands increasing the flow of oxygenated blood into the capillary bed, venules and veins. This yields a net decrease in deoxyhemoglobin concentration which reduces the susceptibility gradients around veins. Thus, during activation the amount of dephasing is decreased ($T2_a^* > T2_b^*$).

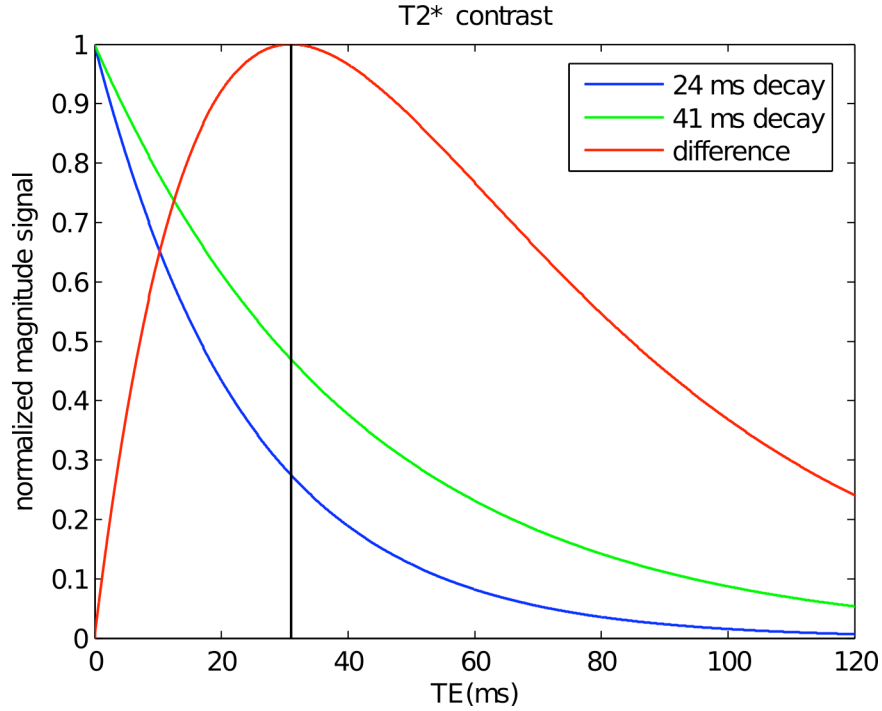


Figure 1.9. T2* contrast as a function of echo time. T2* decay is plotted for a tissue with a T2* of 24ms (blue) and for a tissue with a T2* of 41ms (green). These T2* values are typical of venous blood at baseline and activation states, respectively. The difference between these curves (red) shows that optimal T2* BOLD contrast is obtained at a echo time (TE) between the two T2* values. This optimal echo time is denoted by the vertical black line. In general, the optimal contrast is obtained when $TE = \ln(T2^*_a/T2^*_b)(1/T2^*_a - 1/T2^*_b)^{-1}$, where T2*_a and T2*_b are the venous blood activation and baseline T2* values, respectively.

For field inhomogeneities much larger than the voxel size, a net phase change rather than dephasing of the magnitude signal can result. Under these conditions the field inhomogeneities are roughly constant across the voxel and the voxel signal in Eq [1.24] becomes:

$$s_{\text{voxel}}(t) = e^{-i\phi_y(t)} \int_{\Delta x} \int_{\Delta y} \int_{\Delta z} |m_{xy}(x, y, z, t)| dx dy dz \quad [1.27]$$

In this case, changes in susceptibility gradient strength only change the phase of the voxel

signal. The magnitude of the voxel signal remains constant. In order to understand the conditions that result in BOLD phase changes, the factors that affect the size and strength of susceptibility gradient distributions around veins must be established.

Modeling a vein as an infinitely long cylinder filled with blood, the intra and extravascular susceptibility gradients, ΔB_{intra} and ΔB_{extra} can be expressed as:

$$\Delta B_{intra} = 2\pi\chi_{do}(1-Y)HctB_0(\cos^2\psi - 1/3) \quad [1.28]$$

$$\Delta B_{extra} = 2\pi\chi_{do}(1-Y)HctB_0\sin^2\theta\left(\frac{a}{r}\right)^2\cos 2\rho \quad [1.29]$$

where $\chi_{do} = 0.18 \times 10^{-6}$ is the susceptibility difference between deoxygenated and oxygenated blood (Ogawa and Lee, 1990; Weisskoff and Kiihne, 1992), ψ is the angle between the blood vessel and \mathbf{B}_0 , Y is the fractional oxygen saturation of the blood, Hct is the fractional volume of red blood cells, a is the radius of the vessel, r is distance away from the center of the vessel in the vessel cross section and ρ is the angle away from \mathbf{B}_0 in the cross section (Ogawa et al., 1993). A diagram of these angles and radii are depicted in Fig 1.10A. From Eqs [1.28-29] a few interesting points can be made. First, the strength of these susceptibility gradients is linearly proportional to $(1-Y)$ which can be interpreted as the concentration of deoxyhemoglobin. This explains why activation state $T2^*$ is greater than baseline state $T2^*$. Second, the strength of the susceptibility gradients are linearly proportional to the field strength B_0 . This combines with the linear relationship between \mathbf{m} and B_0 (Eq [1.3]) such that the BOLD contrast-to-noise ratio scales quadratically with field strength. Third, the strength of the extravascular susceptibility gradients are quadratically proportional to vessel radius. This is one reason why BOLD

fMRI experiments are biased toward large veins (Lai et al., 1993; Haacke et al., 1994; Kim et al., 1996; Jochimsen et al., 2004). Using typical physiological parameters (Hct = 0.4, Y = 0.56, B₀ = 4 Tesla and a = 1 mm) the cross section of these susceptibility gradients in units of Hz is plotted in the first row of Fig 1.10B for various values of ψ . Note that when ψ (the angle between the vessel and **B**₀) is ~54°, the intravascular susceptibility gradient is zero. This angle is known as the magic angle (Reichenbach et al., 2000).

Using Eq [1.14] the phase value in and around the vessel can be expressed as:

$$\phi(TE) = -\int_0^{TE} \Delta \omega d\tau = -\gamma \int_0^{TE} \Delta B d\tau = -\gamma \Delta B TE \quad [1.30]$$

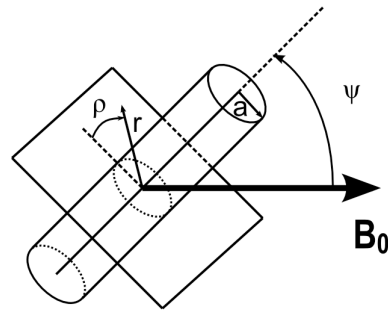
This distribution of phase is plotted in the second row of Fig 1.10B for TE = TE_{-pi}, the TE where the intravascular phase is - π radians for **B**₀ parallel vessels. TE values greater than this yield intravascular phase wrapping in **B**₀ parallel vessels, so in practice longer TEs are avoided.

Across the cross section of a vein, phase varies widely in strength and sign. However within specific regions, phase is relatively constant. For example, the entire intravascular region has the same phase value. Regions adjacent to a vein have fairly flat phase distributions as well. Therefore, for large veins relative to the size of voxels, it is possible to have net BOLD phase changes. Specifically, voxels sampling mainly intravascular regions or extravascular regions adjacent to large veins will follow Eq [1.27]. These voxels will have BOLD phase changes but little BOLD magnitude changes. On the other hand, voxels encompassing smaller veins will tend to sample both positive

and negative phase changes shown in [Fig 10B](#). These voxels will experience BOLD magnitude changes. However, because the extravascular phase changes are symmetric about zero these voxels encompassing smaller veins will have little to no net BOLD phase changes.

These insights on the effect of voxel size and position relative to a vein have very important implications for fMRI. For a BOLD fMRI experiment of a given spatial resolution, BOLD phase changes primarily reflect signal from veins roughly the size of a voxel or larger. We refer to veins in this size range as “large veins”. Given the smaller volume of intravascular regions relative that of extravascular regions, most BOLD phase changes will come primarily from voxels adjacent to large veins. BOLD magnitude changes on the other hand tend to reflect signals from capillaries, venules and veins of all sizes but not from regions adjacent to large veins. Together, these conclusions imply that phase BOLD changes coming from large veins will often be spatially offset from magnitude BOLD changes. This novel insight is key to the success of chapters three and four of this dissertation.

A) Vein diagram



B) Vein susceptibility distribution

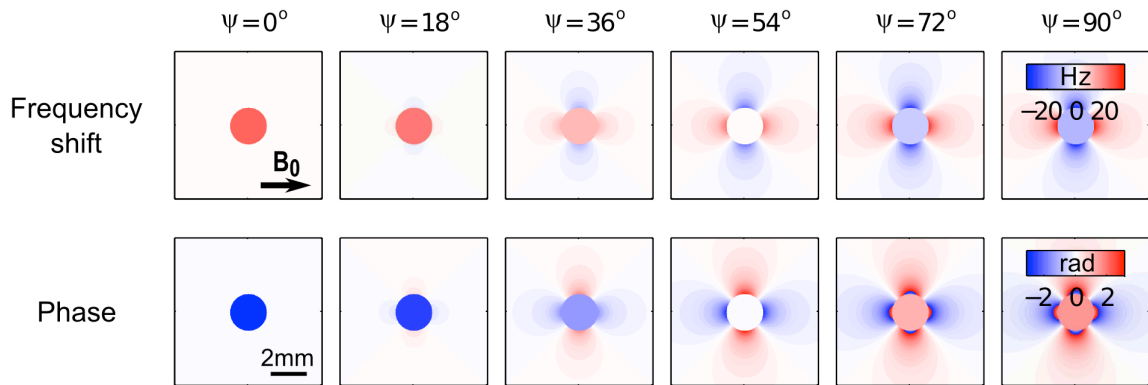


Figure 1.10. Venous susceptibility distribution. A) Vein diagram of radius vectors and angles used in Eqs [1.28-29]. B) Susceptibility distribution in the cross section of a vein as a function of vessel orientation with respect to \mathbf{B}_0 . First row shows susceptibility gradients as frequency shifts relative to f_0 . Second row shows the phase accrual at $TE = TE_{-\pi}$. $TE_{-\pi}$ is the TE required for the venous blood in veins parallel to \mathbf{B}_0 to accrue $-\pi$ radians of phase. TEs longer than this will result in phase wrapping.

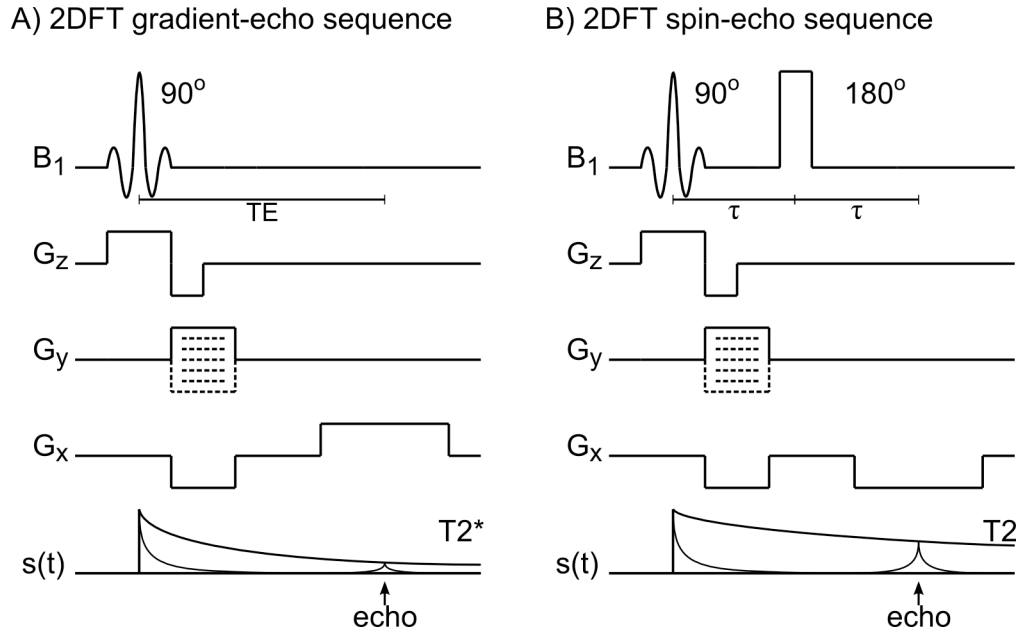


Figure 1.11. 2DFT gradient-echo and spin-echo sequences. B_1 and gradient timecourses are shown for one line in k -space. To cover a grid in k -space, each sequence is repeated with G_y incrementally reduced. A) The gradient-echo sequence only refocuses the phase shifts caused by the readout gradient G_x . Field inhomogeneities dephase the signal such that the echo is reduced by a factor of $\exp(-TE/T2^*)$. This reduction is referred to as $T2^*$ weighting. B) The spin-echo sequence refocuses both phase shifts caused by G_x as well as those caused by other static, large scale field inhomogeneities. Thus, the signal at the echo is only reduced by a factor of $\exp(-TE/T2)$. This reduction is referred to as $T2$ weighting.

BOLD fMRI pulse sequences

The method of collecting k -space using RF excitation followed by a series of pulsed gradients is referred to as a pulse sequence. The methods presented thus far are all a type of gradient-echo pulse sequence. After RF excitation, a negative lobe of G_x is used to travel in the $-k_x$ direction which is always followed by a positive lobe of G_x which travels in the $+k_x$ direction back to the center of the k -space line and beyond. The signal collected at the center of the k -space line is the gradient-echo which by definition occurs at the echo time (TE, Fig 1.11A). Although the positive lobe of G_x refocuses the

dephasing caused by the earlier negative lobe, nothing is done to refocus dephasing caused by other magnetic field inhomogeneities. As previously mentioned, this results in $T2^*$ decay of the baseband signal that is especially sensitive to large veins. These large veins receive drainage from large regions of cortex up to tens of millimeters away (Turner, 2002). This is a problem for BOLD fMRI studies on neural representation at the sub millimeter level as well as those requiring high fidelity information on position of neural activity in the brain. For these studies the ideal pulse sequence is one that records BOLD activity exclusively from the microvasculature (capillaries and venules).

A solution to this problem is the spin-echo pulse sequence (Bandettini et al., 1994; Boxerman et al., 1995; Fig 1.11B). In addition to refocusing dephasing caused by G_x , the spin-echo pulse sequence also refocuses dephasing due to static field inhomogeneities. The mechanism of this refocusing is presented in Fig 1.12. The first half of the sequence is identical to the gradient-echo pulse sequence. RF excitation results in m_{xy} magnetization and field inhomogeneities result in dephasing of m_{xy} . However, the second half is different. τ seconds midway between the RF excitation and the recorded echo is a 180° RF pulse (Fig 1.11B). This results in mirroring of the magnetization vectors across the x-axis such that after another τ seconds all the magnetization vectors are back in phase. The only other sequence difference between gradient-echo and spin-echo is that the positive lobe G_x of the gradient-echo sequence is flipped to be a negative. This is because the 180° RF pulse also rotates the position in k -space by 180° .

For the spin-echo pulse sequence to successfully refocus magnetization, the field inhomogeneity must be static. In other words, the rate of dephasing is assumed to be

constant over time. For magnetization moments that experience different magnetic fields over time, complete refocusing is not possible. This dynamic dephasing (which is much slower than $T2^*$ dephasing) is referred to as $T2$ relaxation or spin-spin relaxation (Fig 1.11B). Water molecules diffusing in and around the susceptibility gradients of vessels less than $20\ \mu\text{m}$ in diameter will experience different field strengths (Bandettini and Wong, 1995). Thus, the spin-echo sequence preserves BOLD contrast from capillaries and smaller venules and discards BOLD contrast from larger veins. To compensate for the loss of BOLD contrast, studies using spin-echo BOLD fMRI are often done at higher field strengths (e.g. 7 Tesla). A few studies have successfully used spin-echo to study neural representation at the sub-millimeter level (Yacoub et al., 2007; Yacoub et al., 2008). However, most studies cannot afford the loss in contrast. As a result, the large majority of BOLD fMRI studies are done using the gradient-echo pulse sequence at the risk of bias toward large veins.

Echo planar k -space trajectory

As previously mentioned, the 2DFT k -space trajectory involves one excitation per line of k -space collected. This results in whole brain scans which can take on the order of minutes to complete. For BOLD fMRI experiments, ideal repetition time (TR) between whole brain scans is on the order of a second if not less (Dale, 1999). To facilitate faster scans, the use of echo planar imaging (EPI) was proposed (Ordidge et al., 1981). An example of the echo planar k -space trajectory is shown in Fig 1.13. After just one slice selective RF excitation, G_x and G_y trace out an entire grid of k -space. This allows for

collection of whole brain images in two to three seconds. However this is at the cost of increased accumulation of phase errors due to imperfections in \mathbf{B}_0 , G_z , G_y , and subject movement. These phase errors result in increased geometric distortions and ghosting (Jezzard and Balaban, 1995; Hu and Tuong, 1996; Schmithorst et al., 2001). In spite of these artifacts, gradient-echo EPI is currently the most commonly used pulse sequence for BOLD fMRI experiments.

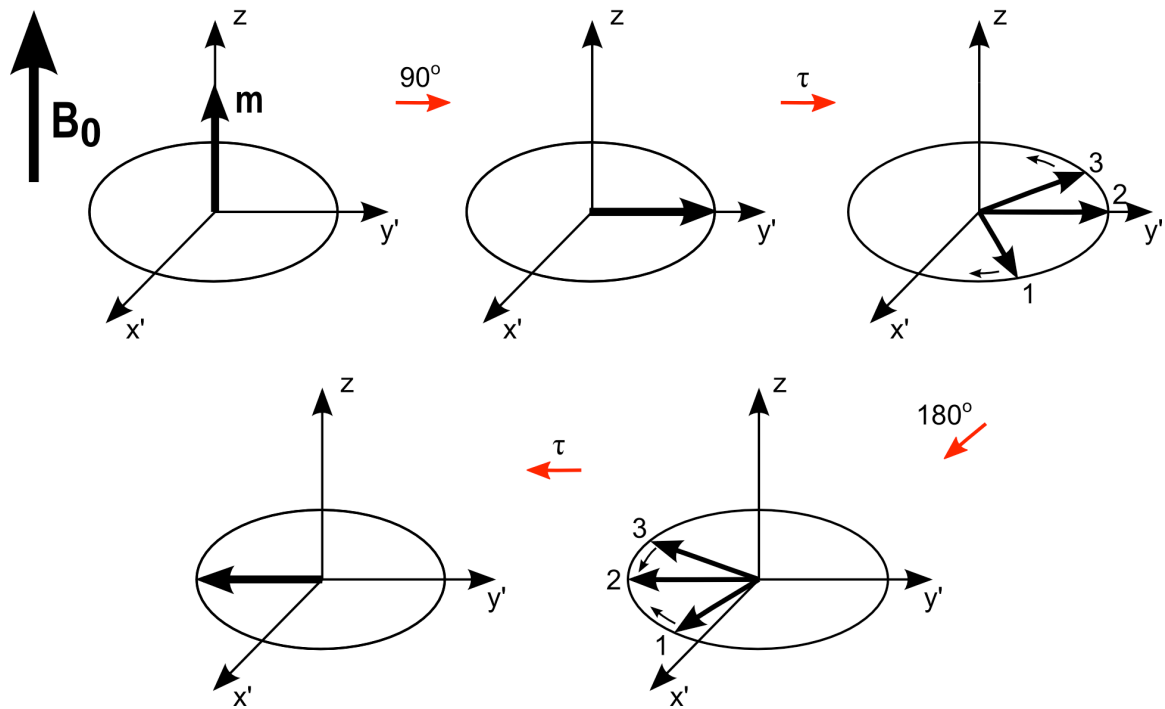
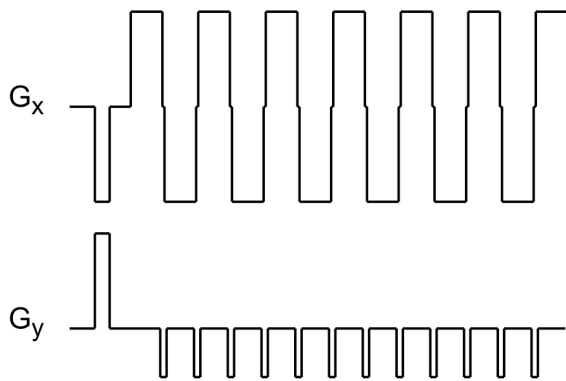


Figure 1.12. Refocusing transverse magnetization with the spin-echo pulse sequence. After the 90° tip, the magnetization in the transverse plane is initially in phase. Due to field inhomogeneities, different magnetic moments accrue different amounts of phase after τ seconds. By tipping the transverse magnetization 180° about the x -axis, the dephasing is refocused after another τ seconds. This refocusing of transverse magnetization is referred to as the spin-echo.

A) Gradients



B) Echo-planar trajectory

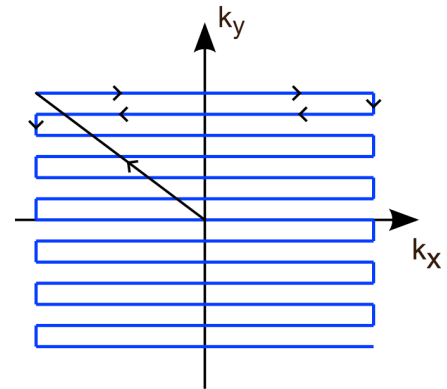
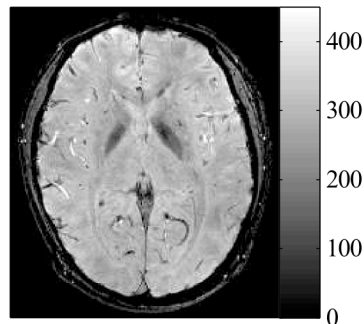


Figure 1.13. Echo planar trajectory. A) Readout G_x and phase encode G_y gradient timecourses. B) Corresponding k -space trajectory. The echo planar trajectory collects an entire grid of k -space after one excitation. Such single shot k -space trajectories are the fastest methods for collecting k -space.

1.3 Complex-valued Magnetic Resonance Imaging

A) Magnitude



B) Phase

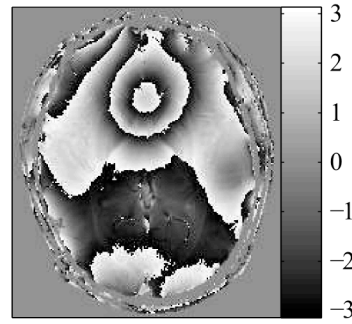


Figure 1.14. Axial slice of a complex-valued MRI volume. A) Magnitude component. B) Phase component. Due to field inhomogeneities, the phase component exhibits numerous phase discontinuities (wraps) between $-\pi$ and π .

Spatial phase unwrapping

As mentioned earlier, images obtained using MRI are generally complex-valued (Fig 1.14, Eq [1.23]). In practice large scale field inhomogeneities due to bone-air-tissue boundaries (e.g. near the fontal sinuses and ear canals) give rise to phase variations that dominate phase images. These field inhomogeneities introduce phase wraps (discontinuities from $-\pi$ to π) across the brain that obscure underlying phase tissue contrast (Fig 1.14B). In complex-valued BOLD fMRI this problem is particularly serious because these field inhomogeneities and thus phase signals vary with subject motion. Depending on the type of subject motion, additional temporal noise or artifactual task-related phase changes across the brain can be introduced (Pfeuffer et al., 2002; van Gelderen et al., 2007).

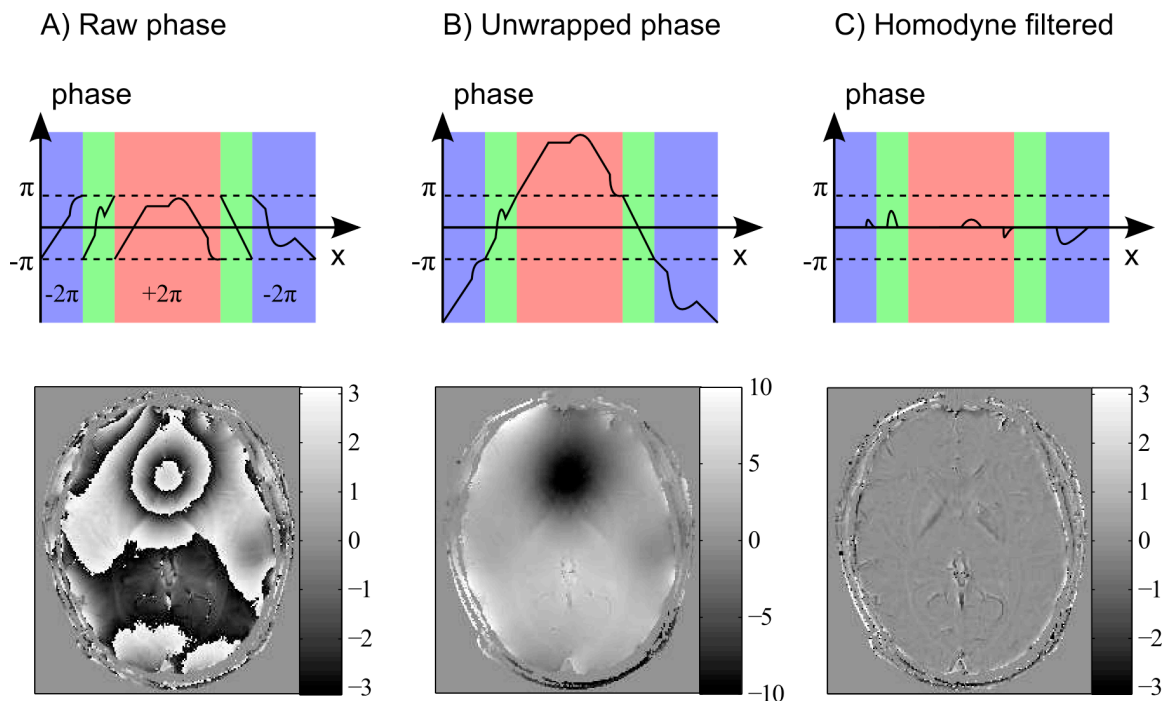


Figure 1.15. Spatial phase unwrapping using PRELUDE followed by homodyne filtering. First row shows a cartoon 1D example of the PRELUDE algorithm. Second row

shows the effect of PRELUDE on an axial slice of actual MRI data. A) The raw phase image exhibits desired tissue contrast as well as undesired spatial discontinuities between $-\pi$ and π (phase wraps). Because these discontinuities are caused by smooth large scale susceptibility gradients, the spatial phase can be unambiguously unwrapped by adding -2π or 2π to a given region of continuous phase. B) The unwrapped phase preserves the desired tissue contrast although the range of unwrapped phase dominates the contrast in the phase image. C) Homodyne filtering is applied to remove the phase contrast due to the smooth large scale susceptibility gradients. Only the desired higher spatial frequency tissue contrast remains.

In studies using phase to enhance spatial tissue contrast (a technique referred to as susceptibility weighted imaging or SWI), removal of large scale non-tissue specific phase accrual is crucial. One of the most popular methods for removing these phase wraps is called: Phase Region Expanding Labeler for Unwrapping Discrete Estimates or PRELUDE (Jenkinson, 2003). [Fig 1.15](#) illustrates the mechanism behind the PRELUDE algorithm. As implied by its full name, PRELUDE first labels regions of continuous phase. This is demonstrated in the first row of [Fig 1.15](#) with the red, green and blue regions. PRELUDE then takes advantage of the smooth large scale nature of the susceptibility gradients responsible for the phase wraps. Because the gradients are smooth the phase can be unambiguously unwrapped by adding -2π or 2π to adjacent phase regions. The sign of the 2π term is determined by the slope of the phase changes near the boundary between the two regions. [Fig 1.15B](#) shows that unwrapping the phase in this way preserves the local phase tissue contrast although the unwrapped phase values are still dominated by unwanted large scale susceptibility gradients.

To remove the effects of the large scale susceptibility gradients, homodyne filtering is performed on the unwrapped phase images (Noll et al., 1991; Reichenbach et al., 2000). [Fig 1.16](#) demonstrates this processes for an axial slice of the brain. First, the

entire complex-valued image is lowpass filtered and the phase component of this image is extracted (Fig 1.16B). This phase image only contains the effects of the large scale susceptibility gradients and is subtracted from the original phase image using complex division. The remaining phase image after the subtraction is the desired phase image. This image reflects only phase contrast from the fine scaled tissue susceptibility differences of interest (Fig 1.16C).

Unfortunately for BOLD fMRI studies, unwrapping phase using PRELUDE is prohibitively time consuming. Because PRELUDE is a region expanding algorithm, it can take several hours to unwrap a single phase volume. Given that BOLD fMRI data sets can consist of thousands of volumes, it would take months even with multiple computers to unwrap all phase volumes. Fortunately, homodyne filtering by itself can be used to unwrap a single phase volume in just a few seconds. Fig 1.16 shows the effect of homodyne filtering with and without PRELUDE (for a more in-depth comparison see Hammond et al., 2008). Homodyne filtering alone does remove most of the phase contrast from large scale susceptibility gradients while preserving the fine scale phase tissue contrast. However, it often fails to remove phase wraps due to stronger susceptibility gradients in the frontal and temporal lobes. To minimize these residual phase wraps, the size of the lowpass filter can be increased and more time can be spent on improving shim quality. The BOLD fMRI work in this dissertation uses only the homodyne filter algorithm to facilitate timely phase unwrapping of functional phase volumes. However, for unwrapping the phase of venograms, the PRELUDE – homodyne filter approach is used.

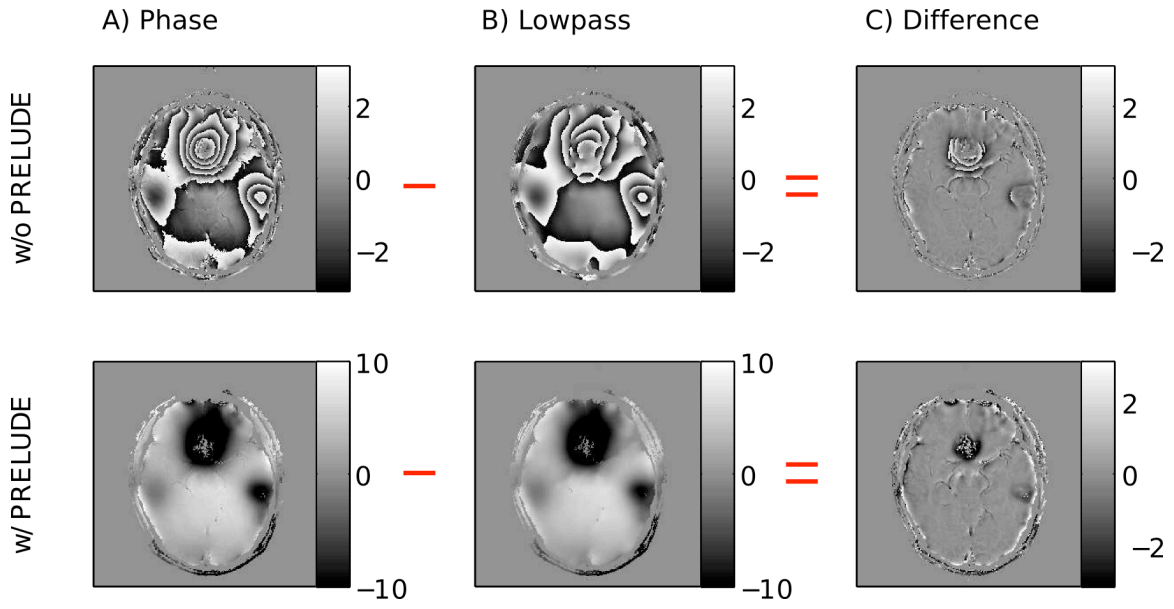


Figure 1.16. Homodyne filter algorithm for phase unwrapping. First row shows homodyne filtering applied on the raw phase image (without PRELUDE). Second row shows homodyne filtering applied after the PRELUDE algorithm. A) Phase image input to the homodyne filter. B) The first step of the homodyne filter is to extract the phase image of a lowpass filtered version of the original complex-valued image. This lowpass phase image captures the phase contrast due to large scale susceptibility gradients. C) By taking the difference between the phase images in (A) and (B), the phase contrast from large scale susceptibility gradients are removed. The homodyne filter algorithm alone can remove most of the phase contrast from large scale susceptibility gradients. However, it fails to remove phase wraps due to stronger susceptibility gradients in frontal and temporal cortex. Using PRELUDE helps remove the effect of these stronger gradients.

Susceptibility weighted venography

This dissertation focuses on the large vein contribution to the BOLD signal. An important step in this investigation is to non-invasively measure where cortical veins are with respect to BOLD activity. To do this, we utilize one method of susceptibility weighted imaging: susceptibility weighted venography (SWV). This technique uses the phase changes due to susceptibility gradients from veins to enhance the T2* contrast between veins and gray matter found in magnitude images (Reichenbach et al., 2000).

Because the $T2^*$ of venous blood is much smaller than the $T2^*$ of gray matter, veins will appear much darker than gray matter in MRI images with reasonably long TEs (Reichenbach et al., 1998). Of course in order to use the phase images, they must first be unwrapped using the techniques described above. In addition to this, phase values which range from $-\pi$ to π must be transformed to magnitude weightings ranging from zero to one. This way, vein–gray matter magnitude contrast is enhanced by element-wise multiplication of a magnitude image with its corresponding magnitude weightings. Thus, phase values indicative of a vein should have a weight close to zero to enhance the darkness of veins while phase values indicative of gray matter should have a weight close to one.

To determine the appropriate phase transformation, previous susceptibility weighted venography (SWV) studies realized that the extravascular region of veins had a net phase value of zero. Therefore, these studies based their phase transformations on intravascular phase values and two key facts. First, the phase of tissue outside of veins (e.g. gray matter) is by definition zero. Second, the absolute value of intravascular phase is proportional to deoxyhemoglobin concentration (Eq [1.28]). Given these two facts, all previously published phase transformations generally give phase values near zero a weight of one, and monotonically reduce the weight to zero for larger absolute phase values in the range of $-\pi$ to π (Reichenbach et al., 2000; Reichenbach and Haacke, 2001; Brainovich et al., 2008). However, in order for these phase transformations to weight veins appropriately, intravascular phase must not wrap (exceed $-\pi$ or π). Given that veins parallel to \mathbf{B}_0 have the largest absolute phase values of all possible orientations (Eq

[1.28]), SWV studies set $TE \leq TE_{-pi}$. This limits the intravascular phase of \mathbf{B}_0 parallel veins to $-\pi$ and prevents intravascular phase values from vessels of all orientations from wrapping.

The SWV methods just discussed have been shown to provide robust, high contrast-to-noise images of veins (Reichenbach et al., 2000; Reichenbach and Haacke, 2001; Brainovich et al., 2008). However, two limitations stand out. First, TE_{-pi} is generally less than TE_{opt} , the TE for optimal magnitude $T2^*$ contrast between venous blood and gray matter. Thus, current SWV methods prevent intravascular phase wrapping at the cost of magnitude contrast. Second, even when TE is less than TE_{-pi} phase wrapping can still occur. If the volume fraction of red blood cells (Hct) or the concentration of deoxyhemoglobin (1-Y) is underestimated, intravascular phase values may still wrap (Eq [1.28]). Also, depending on voxel size and position, extravascular phase sampled by a voxel will generally not sum to zero. This may also lead to phase wrapping (Eq [1.29]). In the presence of phase wrapping, phase transformations used in current SWV methods will lead to incorrect weighting of veins. Chapter two of this dissertation goes into more depth comparing prior phase transformations and resolves these two limitations of previous SWV methods by using a novel phase transformation robust to phase wrapping. We refer to this phase transformation as the tri-segment phase transformation.

Complex-valued BOLD fMRI

As mentioned earlier, BOLD fMRI data are originally complex-valued with both

magnitude and phase components able to exhibit BOLD signal changes. However most BOLD fMRI studies analyze only the magnitude component and ignore the phase component (Bandettini et al., 1993; Cox et al., 1995). Because the source of BOLD phase changes are large draining veins, it has been argued that including the phase component would bias BOLD activity away from sites of neural activity and decrease overall information available in the BOLD signal (Menon, 2002; Duong et al., 2003; Hulvershorn et al., 2004; Nencka and Rowe, 2007). It has also been assumed that phase does not exhibit BOLD signal changes and that it is merely a source of noise (Rowe and Logan, 2004).

More recently however, some studies have considered using both the magnitude and phase components for measuring BOLD signal changes with increased statistical power (Rowe, 2005; Lee et al., 2007). These studies fit stimulus parameters for the magnitude and phase components separately for each voxel and calculate BOLD activation from these parameters using multivariate versions of the F -statistic. These studies show increased sensitivity to BOLD activation from larger regions of cortex relative to standard magnitude measures of BOLD activity. However, three limitations stand out. First, although these studies doubled the amount of data by including the phase component of the BOLD signal, they also doubled the number of parameters that need to be fit. This doubling of parameters is unnecessary given that the source of the BOLD phase and magnitude changes tend to be the same (large veins). Doubling the number of parameters in this case results in suboptimal statistical power (Glantz, 2005). Second, the use of F -statistics to evaluate activation removes the sign of the BOLD response. From

the point of view of these studies, this is a necessary cost to incorporate the phase component, the sign of which depends on many unmeasured factors (Eqs [1.28-29]). However, for many studies this ambiguity is unacceptable. Third, as mentioned previously, BOLD phase changes will often be spatially offset from BOLD magnitude changes around large veins. Thus, the expanded regions of BOLD activity detected by these complex-valued fMRI methods may actually reflect increased bias toward large veins. Chapter three of this dissertation goes into more depth quantifying these limitations and resolves them using a novel method for combining the magnitude and phase components of the BOLD signal. We refer to this method as source-localized phase adjacent magnitude combination fMRI (spamfMRI).

Quantification of venous contributions to semantic category areas

Numerous studies have shown that gradient-echo BOLD fMRI is heavily biased toward contributions from large draining veins (Lai et al., 1993; Haacke et al., 1994; Kim et al., 1996; Jochimsen et al., 2004). However, the impact of this large vein bias in the localization and measurement of semantic category areas has not been examined. To address this issue, chapter four of this dissertation compares standard magnitude measures of BOLD activity to large vein suppressed measures of BOLD activity in face and place selective regions of the human brain (Kanwisher et al., 1997; Epstein et al., 1998). In practice, the contribution of large veins to the BOLD signal is difficult to quantify. Given the large vein suppression effects of spin-echo, a comparison between the BOLD activity from spin-echo and gradient-echo pulse sequences might sound

reasonable. However, given that the BOLD contrast mechanisms of spin-echo and gradient-echo are different (T_2 vs T_2^*), BOLD activity from the two sequences are not directly comparable. Because the intravascular contributions reflect only a small portion of the BOLD signal, other attempts to quantify venous contributions using diffusion and flow suppression of blood signals are also inconclusive (Gao et al., 1996; Kim et al., 1996; Duong et al., 2003).

More recent studies have developed methods for suppressing the large vein contribution to BOLD activity using standard gradient-echo pulse sequences (Menon, 2002; Nencka and Rowe, 2007). Realizing that BOLD phase changes come exclusively from large veins, these large vein suppression techniques penalize BOLD magnitude changes based on the amount of BOLD phase changes in a given voxel. These techniques are attractive because they do not require pulse sequence modification and suppress both intra and extravascular BOLD signals. Thus, they can be used to quantify large vein contributions to gradient-echo BOLD fMRI. However, these techniques are not without limitations. Nencka and Rowe (2007) cautioned against the use of these large vein suppression techniques given their tendency to over or under-correct for large vein contributions. Furthermore, these large vein suppression techniques assume that voxels containing large veins will exhibit strong BOLD phase changes. This assumption begins to breakdown for large veins roughly the size of the voxels, as well as for veins near the magic angle (Reichenbach et al., 2000). Chapter four of this dissertation discusses and quantifies these limitations in detail and resolves them using a novel method for large vein suppression. We refer to this method as source-localized phase regressor (sPR).

Chapter 2: Long echo time tri-segment phase transformation in magnetic resonance venography

The majority of brain activity detected in studies using blood oxygen level dependent (BOLD) fMRI comes from large draining veins. Thus, localization of large veins is important for interpretation of fMRI data. In this chapter, we review recent advances in a non-invasive MRI technique for localizing veins: susceptibility weighted venography (SWV). We propose a version of SWV that eliminates vulnerability to phase wrapping while allowing for increased vein-gray matter contrast-to-noise ratio (CNR). We also discuss the importance of extravascular frequency shifts in determining the echo time (TE) that will produce maximum vein-gray matter contrast.

2.1 Background

The most basic MR venogram is a gradient-echo T2* weighted venogram in which veins appear darker than the surrounding gray matter (Reichenbach et al., 1998). This tissue contrast comes from venous blood whose T2* is shorter than that of gray matter at standard clinical field strengths (Table 2.1). Thus the magnitude of the venous signal decays more rapidly than that of gray matter. Fig 2.1 demonstrates typical signal decay of venous blood (blue) and gray matter (green) as a function of TE. Their difference is plotted in red. The vertical solid black line depicts TE_{opt} , the TE that yields optimal magnitude contrast between venous blood and gray matter given the T2* of venous blood and gray matter at 3T.

T2* (ms)	1.5T	3T	4T	7T
Venous blood	56 ^b	35 ^f	24 ^c	13 ^c
Gray matter	65 ^d	49 ^{d,e}	41 ^{a,c}	25 ^c

TE (ms)	1.5T	3T	4T	7T
Optimal CNR : TE _{opt}	60	41	31	18
$\phi_{iv} = -\pi$: TE _{-pi}	56	28	21	12
$\phi_{iv} = -4\pi/3$: TE _{-4pi/3}	71	35	26	15

CNR relative to CNR at TE _{opt}	1.5T	3T	4T	7T
CNR at TE _{-pi}	99.8%	93.7%	93.6%	93.7%
CNR at TE _{-4pi/3}	98.8%	98.7%	98.6%	98.7%
CNR gain	-1.0%	+5.3%	+5.3%	+5.3%

a. Jezzard et al., 1996 b. Debiao Li et al., 1998 c. Yacoub et al., 2001
d. Kruger et al., 2001 e. Wansapura, 1999 f. interpolated

Table 2.1 Contrast properties of venous blood and gray matter. Top: Reported T2* values for venous blood and gray matter. Middle: Echo times: TE_{opt}, TE_{-pi} and TE_{-4pi/3}. TE_{opt} is the echo time for optimal CNR between venous blood and gray matter. TE_{-pi} and TE_{-4pi/3} are the echo times for $-\pi$ and $-4\pi/3$ intravascular phase accrual for veins parallel to B₀, respectively (see Eq [A.1.1] in Appendix). Bottom: Vein-gray matter contrast at TE_{-pi} and TE_{-4pi/3} relative to CNR at TE_{opt}. CNR gain was calculated as the ratio of relative CNR at TE_{-4pi/3} to relative CNR at TE_{-pi}. Using reported T2* values, TE_{-4pi/3} offers an estimated ~5% gain in vein-gray matter magnitude CNR over that of the conventional TE_{-pi} at field strengths greater than 1.5 T. Relative CNR = $\frac{diff(TE_{used})}{diff(TE_{opt})} \cdot 100\%$, where $diff(TE) = e^{-TE/T_2^*} - e^{-TE/T_2^*}$.

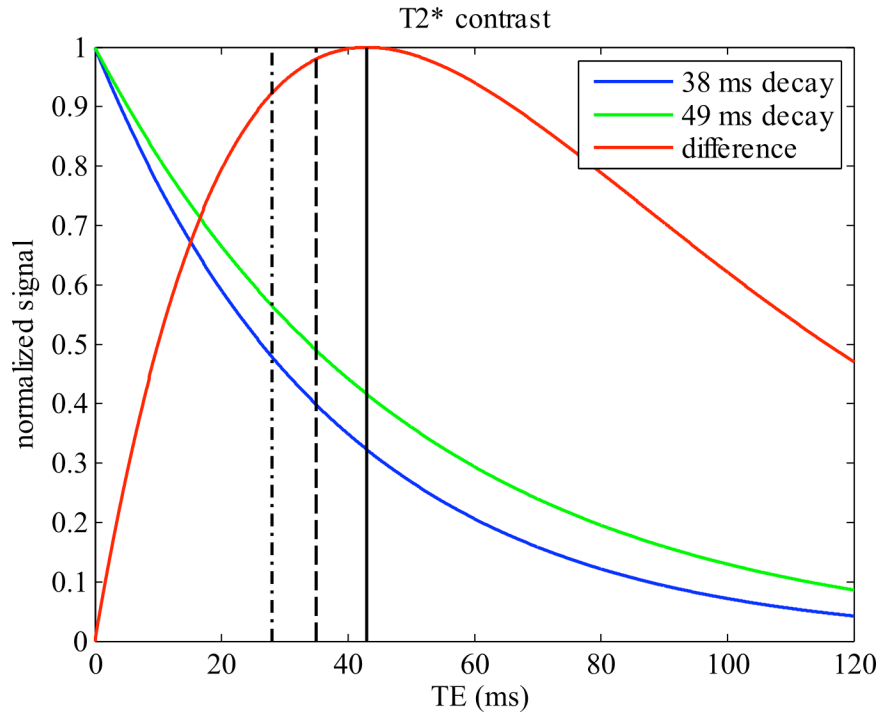


Figure 2.1. T2* contrast as a function of TE. Signal decay curves with T2* = 35ms for venous blood (blue) and T2* = 49ms for gray matter (green). The contrast between the two curves is shown in red. The vertical solid black line marks the peak at TE = TE_{opt}. The dashed and dashed dotted lines mark TE_{-π} and TE_{-4π/3} respectively. The venous-gray matter contrast is greater at TE_{-4π/3} than at TE_{-π}, but is it greatest TE_{opt}.

To further enhance venous-gray matter contrast, several studies have proposed utilizing the phase component of complex-valued MR images (Haacke et al., 1995; Reichenbach et al., 2000; Reichenbach and Haacke, 2001; Brainovich et al., 2008). Due to the magnetic susceptibility difference between venous blood and surrounding tissue, voxels containing large veins will tend to have non-zero phase values while those containing only gray matter will tend to have near-zero phase values (for details see Appendix A.1). Taking advantage of this, these studies transform the phase component of venograms (which range from $-\pi$ to π) to magnitude weightings ranging from zero to one.

By multiplying this transformed version of the phase element-wise with the magnitude component, veins can be made to appear darker.

Over the years much progress has been made on optimizing the phase transformation to appropriately weight large vein containing voxels (where “large vein” refers to veins roughly the size of the voxels scanned or larger). Assuming that the extravascular phase sums to zero, previous studies designed their phase transformations based on intravascular phase accrual. Given the distribution of intravascular phase values for a uniform distribution of vein orientations (Fig 2.2A, for derivations see Appendix A.1), three phase transformations have been proposed. Reichenbach et al. (2000) considered the phase accrual of veins near parallel to B_0 and developed a phase transformation that penalizes voxels with negative phase, leaving those with zero or positive phase unpenalized (Fig 2.3A). Later, Reichenbach et al. (2001) considered both positive and negative phase accrual by penalizing positively and negatively phased voxels with a symmetric phase transformation (Fig 2.3B). More recently, Brainovich et al. (2008) took into account the range of intravascular phase accrual across all vein orientations (Fig 2.2A). They noted that intravascular phase can range from $-\pi$ to $+\pi/2$ without wrapping. Thus, they proposed an asymmetric phase transformation (Fig 2.3C) which further improved vein-gray matter contrast. We refer to this phase transformation as the asymmetric phase transformation.

Common to all prior phase transformations is the assumption that phase accrual due to veins will not wrap beyond $-\pi$. For the asymmetric phase transformation it is assumed that venous phase will not accrue in the range $+\pi/2$ and $+\pi$ (Fig 2.3C). If this assumption

fails, applying the asymmetric phase transformation will result in incorrect weighting of susceptibility weighted magnitude intensities. This can happen in voxels where extravascular phase does not sum to zero (the center of the voxel and vein are not aligned) or when TE is set to a value that is too long. Thus prior studies on SWV often limited TE to prevent phase wrapping at the cost of vein-gray matter contrast. This cost exists because $TE_{-\pi}$ (the TE for B_0 parallel veins to accrue $-\pi$ radians of intravascular phase) is less than TE_{opt} (the TE for optimal vein-gray matter magnitude contrast) at all standard clinical field strengths (Table 2.1).

We assert that the TE can be extended beyond $TE_{-\pi}$ for improved vein-gray matter contrast without aliasing of phase. Ordinarily, if the maximum positive and negative rate of phase accrual (i.e. frequency shifts) were of equal magnitude, phase accrued beyond $-\pi$ would wrap and alias with phase near $+\pi$ and vice versa. However careful consideration of Eq [A.1.1] and Fig 2.2A reveals that this is not the case. The rate of intravascular phase accrual for veins parallel to B_0 is twice that of veins perpendicular to B_0 . Therefore, assuming no other sources of phase accrual, the TE can be extended for $-4\pi/3$ radians of phase accrual in veins parallel to B_0 without aliasing. This extension of TE would allow complete usage of the $-\pi$ to $+\pi$ range of phases for improved vein-gray matter phase contrast (Fig 2.2B). It would also allow the TE to approach TE_{opt} for improved vein-gray matter magnitude contrast.

To facilitate phase wrapping due to extending the TE to $TE_{-4\pi/3}$ and potentially due to non-zero extravascular phase accrual we propose a new phase transformation we refer to as the tri-segment phase transformation (Fig 2.3D). Using the tri-segment phase

transformation together with a TE of $TE_{-4\pi/3}$ we expect to see an increase in vein-gray matter magnitude contrast of $\sim 5\%$ (Table 2.1). We also expect to see an increase in phase contrast linearly proportional to the increase in TE (Eq [A.1.3]). To determine the combined magnitude and phase contrast gained by extending TE to $TE_{-4\pi/3}$, we compared the vein-gray matter contrast of SWV images scanned using $TE_{-\pi}$ and $TE_{-4\pi/3}$ at 3T. To determine if accounting for phase wrapping improves vein-gray matter contrast we also compared SWV images based on the asymmetric phase transformation to those based on the tri-segment phase transformation proposed here.

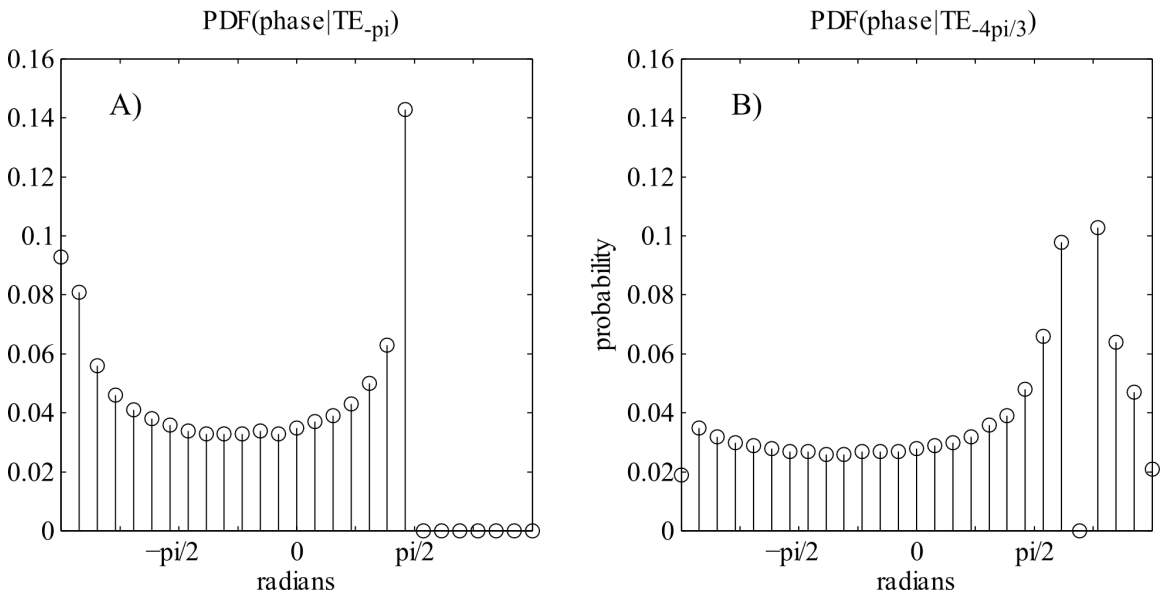


Figure 2.2. Intravascular phase probability distributions. A) The expected probability distribution of intravascular phase throughout cortex when $TE = TE_{-\pi}$ for $-\pi$ intravascular phase accrual in veins parallel to B_0 . This is assuming the orientation distribution of veins relative to B_0 is isotropic (i.e. a flat probability distribution for ψ in Eq [A.1.1]). B) Same as (A) except $TE = TE_{-4\pi/3}$ for $-4\pi/3$ intravascular phase accrual.

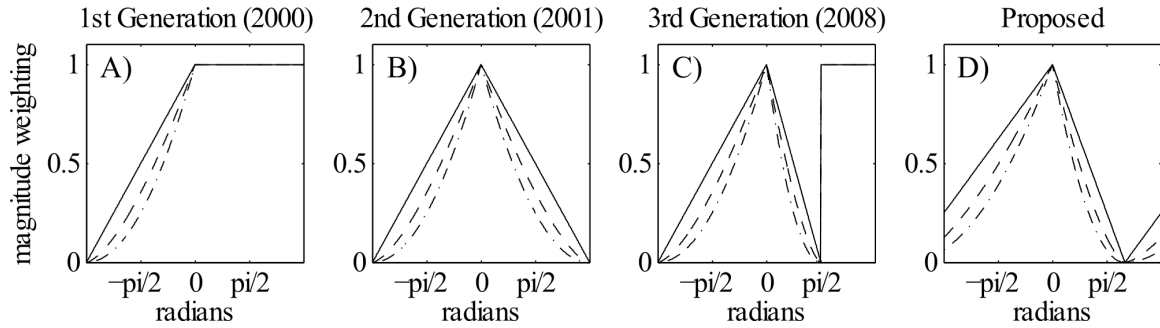


Figure 2.3. Phase transformations. A) Penalty for voxels with negative phase only (Reichenbach et al., 2000) B) Symmetric penalty for voxels with non-zero phase (Reichenbach and Haacke, 2001) C) Asymmetric penalty for voxels with non-zero phase less than $+\pi/2$ (Brainovich et al., 2008) D) Tri-segment asymmetric penalty for voxels with non-zero phase accounting for phase wrapping. Dashed and dash-dotted lines represent the original transformations raised to the 1.5th and 2nd power, respectively. Higher powers increase the sensitivity of SWV to phase accrual.

2.2 Methods

Susceptibility weighted venograms

All MR data were collected with whole-head radiofrequency array coils on the 3 Tesla Siemens (Erlangen, Germany) Magnetom Tim Trio scanner at UC Berkeley. Procedures were approved by the UC Berkeley Committee for the Protection for Human Subjects and performed on two subjects who gave written informed consent.

Two 3D gradient-echo venograms were collected for each subject with flip angle 15° , TR 45ms, voxel size $0.92 \times 0.92 \times 2 \text{ mm}^3$, and FOV $234 \times 234 \times 128 \text{ mm}^3$. The first set of venograms used $TE = TE_{-\pi} = 28 \text{ ms}$ while the second set used $TE = TE_{-4\pi/3} = 35 \text{ ms}$. Flow compensation was used to ensure phase values were not contaminated by flow (Reichenbach et al., 1998).

Image processing was based on custom code written in Matlab (The Mathworks, Natick, MA), except for phase unwrapping which was done using PRELUDE (Jenkinson,

2003) in FSL (Smith et al., 2004; Woolrich et al., 2009). Large scale phase wrapping due to field inhomogeneities was first eliminated using PRELUDE followed by homodyne filtering (Noll et al., 1991) on a slice by slice basis (Figs 2.4A-C; see Hammond et al., 2008 for a similar procedure). A filter size of 96 gave best results. Phase masks (Fig 2.4D) were then generated using the tri-segment phase transformation proposed here (Fig 2.3D). Taking into account phase wrapping, intravascular phase accrued by B₀ parallel and perpendicular veins begin to alias at $+2\pi/3$. Thus, our tri-segment phase transformation was implemented as:

$$\begin{aligned} \text{magWeight} &= \text{phase}/(4\pi/3)+1; & \text{for phase} \leq 0 \\ \text{magWeight} &= -\text{phase}/(2\pi/3)+1; & \text{for } 0 < \text{phase} \leq 2\pi/3 \\ \text{magWeight} &= \text{phase}/(4\pi/3)-1/2; & \text{for phase} > 2\pi/3 \end{aligned}$$

Element-wise multiplication of the phase masks (Fig 2.4D) with the magnitude images (Fig 2.4E) yielded vein-gray matter contrast enhanced susceptibility weighted magnitude images (Fig 2.4F). Finally, minimum intensity projection (mIP) was performed on the susceptibility weighted magnitude images in the axial plane across three slices (6 mm projections, Fig 2.4G). This further improved visibility of veins across slices. Results are shown in Figs 2.6-9. For comparison we also created venograms based on the asymmetric phase transformation (Fig 2.3C).

Matching Transformations

The asymmetric phase transformation is naturally more sensitive to phase accrual in the range of $-\pi$ and $+\pi/2$ than the tri-segment phase transformation proposed here. To

ensure that both transformations would be about equally sensitive (except in the phase wrapping interval greater than $+\pi/2$), we raise each phase transformation to an appropriate power before applying them to the phase images (Fig 2.5). We examined a range of potential exponents from one to three. The asymmetric and tri-segment phase transformations were most comparable if they were raised to the 1.5th and 2nd power, respectively. With these exponents the asymmetric phase transformation remained slightly more sensitive to most phase accruals less than $+\pi/2$. This way the results would not be biased toward our tri-segment phase transformation.

Quantifying contrast to noise gains

Using our tri-segment phase transformation to account for phase wrapping, we expect that extending the TE from $TE_{-\pi} = 28\text{ms}$ to $TE_{-4\pi/3} = 35\text{ms}$ will enhance vein-gray matter contrast. To quantify this enhancement, we calculated the magnitude, phase, and SWV CNR gains for large vein containing voxels. Magnitude CNR gain was calculated as $[(1-\text{mag}(TE_{-4\pi/3}))-(1-\text{mag}(TE_{-\pi}))] / (1-\text{mag}(TE_{-\pi})) * 100\%$, where $\text{mag}(TE)$ is the magnitude intensity of the large vein containing voxel normalized to the mean intensity of surrounding gray matter at the specified TE. Phase CNR gain and SWV CNR gain were calculated in the same way using the corresponding phase values and susceptibility weighted magnitude intensities, respectively. Note, noise is not explicitly modeled in CNR gain calculations because the noise term cancels out.

To demonstrate the importance of accounting for phase wrapping in a phase transformation, we also calculated the SWV CNR gain between susceptibility weighted

magnitude intensities produced using the tri-segment and the asymmetric phase transformations with $TE = TE_{-4\pi/3}$. In this case, SWV CNR gain was calculated as $[(1 - SWV(\text{tri-seg})) - (1 - SWV(\text{asym}))] / (1 - SWV(\text{asym})) * 100\%$, where $SWV(\text{tri-seg})$ and $SWV(\text{asym})$ are the susceptibility weighted magnitude intensities of the large vein containing voxel based on the tri-segment and asymmetric phase transformations, respectively.

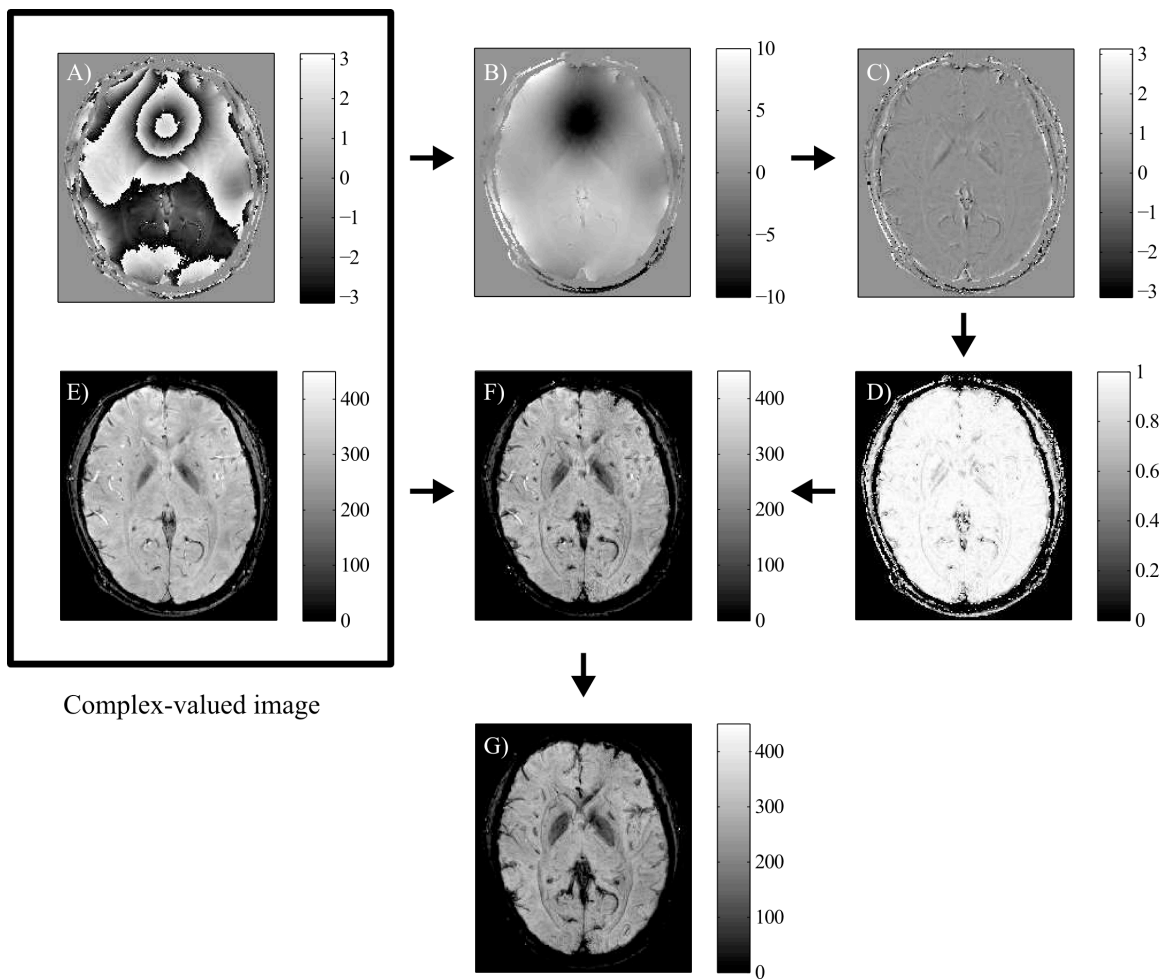


Figure 2.4. Steps in susceptibility weighted venography (SWV). A) Raw phase image. B) PRELUDE unwrapped phase image. C) Homodyne filtered phase image. D) Phase mask.

E) Magnitude image. F) Susceptibility weighted magnitude image. G) Susceptibility weighted venography image. Large-scale phase wrapping is first unwrapped by processing the raw phase image with PRELUDE. This unwrapped phase is homodyne filtered resulting in the final phase image. The phase mask is generated by applying the desired phase transformation to this phase image. The original magnitude image is then multiplied element-wise with the phase mask. The result is the contrast-enhanced susceptibility weighted magnitude image. Finally, minimum intensity projection across a sliding window of axial slices is taken to yield the susceptibility weighted venogram.

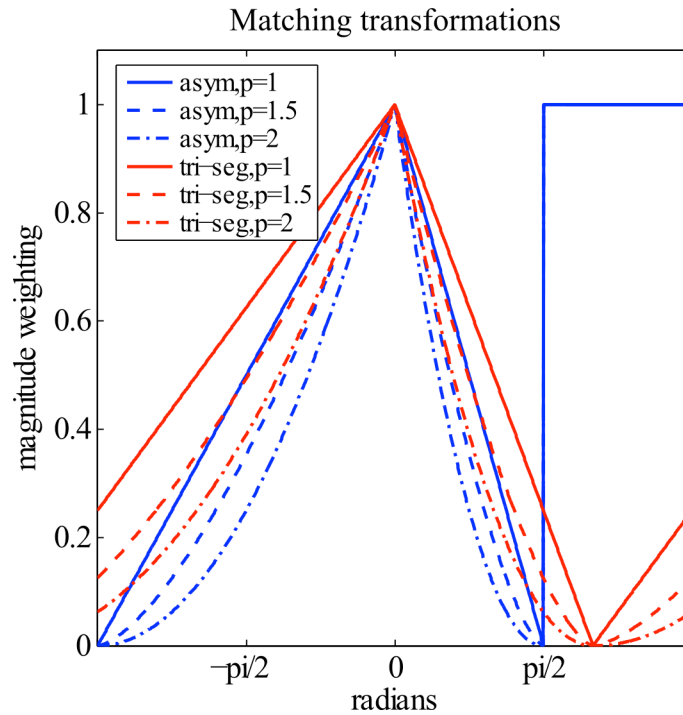


Figure 2.5. Phase transformation matching. The asymmetric phase transformation is naturally more sensitive to phase accrual between $-\pi$ and $+\pi/2$ than the tri-segment phase transformation. To fairly compare the two, we raised the asymmetric phase transformation and the tri-segment phase transformation to the 1.5th and 2nd power, respectively. Solid lines show the original phase transformations. Dashed and dashed dotted lines show the phase transformations raised to the 1.5th and 2nd power, respectively. After applying the power correction, the two transformations are very similar. However, the asymmetric phase transformation remains slightly more sensitive to most phase accruals in the $-\pi$ to $+\pi/2$ interval.

2.3 Results

Effect of extended TE

To determine if extending TE from $TE_{-\pi}$ to $TE_{-4\pi/3}$ increases vein-gray matter contrast, we first visually compared the vein-gray matter contrast of susceptibility weighted venograms obtained using the two TEs and the asymmetric phase transformation. [Fig 2.6A](#) shows a typical axial slice of a venogram obtained using $TE_{-\pi}$. [Fig 2.6B](#) shows the corresponding slice obtained using $TE_{-4\pi/3}$. As expected, the overall signal intensity of the extended TE venogram is reduced relative to that of the shorter TE. At the same time, the vein-gray matter contrast is enhanced with the extended TE relative to that of the shorter TE. These results suggest that previous SWV studies using $TE_{-\pi}$ sacrificed vein-gray matter contrast to prevent intravascular phase from wrapping.

To quantify the effect of extending TE from $TE_{-\pi}$ to $TE_{-4\pi/3}$, we plotted the cross section of voxel values in and around a typical vein near parallel with B_0 . We computed the vein-gray matter contrast-to-noise ratio (CNR) gain for the central voxel of the vein scanned. [Fig 2.7A](#) shows the magnitude intensities along the cross section of the vein scanned with $TE = TE_{-\pi} = 28\text{ms}$ (blue) and with $TE = TE_{-4\pi/3} = 35\text{ms}$ (red). The vertical dashed line indicates the center of the vein where CNR gain was calculated. CNR gain was calculated to be 37% for this vein (see Methods for details). This is roughly seven times greater than the expected magnitude CNR gain of ~5% ([Table 2.1](#)) which was calculated using the standard assumption of only intravascular venous blood within the voxel (no partial volume effects). Because the size of the CNR gain is so large, it is unlikely to be a result of variations of $T2^*$ values (Koopmans et al., 2008). Instead, this result suggests that for large veins $T2^*$ decay is not purely exponential (Haacke et al.,

1995; Nishimura, 1996; see Discussion for details).

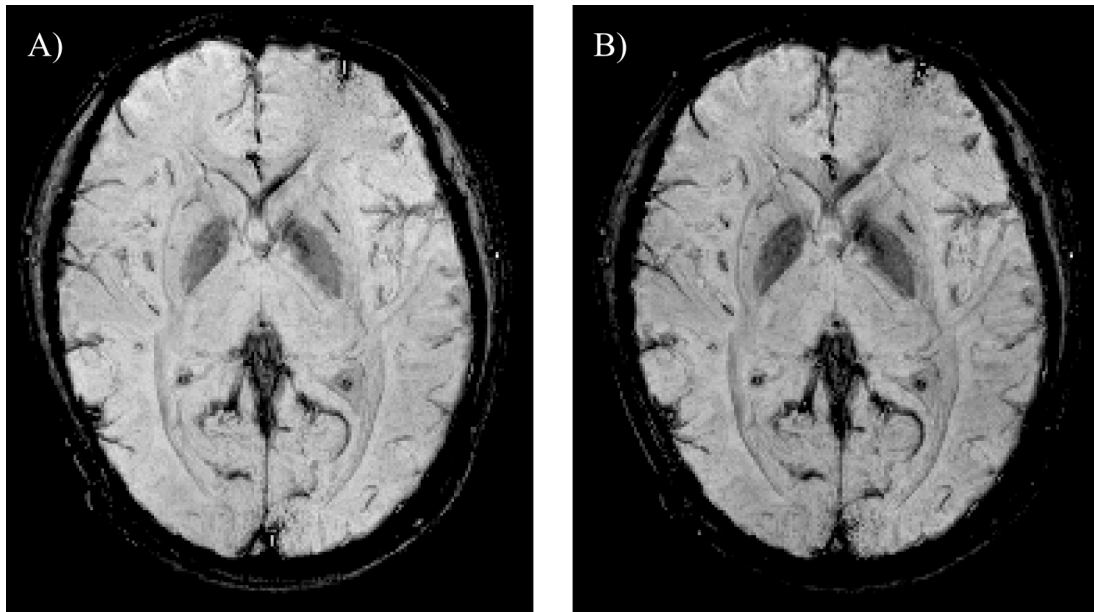


Figure 2.6. Effect of extending TE on vein-gray matter contrast. A) Typical axial slice of a susceptibility weighted venogram with $TE = TE_{-pi} = 28\text{ms}$ using the asymmetric phase transformation. B) Same as (A) but with $TE = TE_{-4pi/3} = 35\text{ms}$. Vein-gray matter contrast is greater with $TE_{-4pi/3}$ than with TE_{-pi} .

[Fig 2.7B](#) shows the phase values along the cross section of the vein (same format as [Fig 2.7A](#)). Phase CNR gain was calculated to be an astonishing 136%. This is roughly five times greater than the expected phase gain of $(TE_{-4pi/3} - TE_{-pi}) / TE_{-pi} * 100\% = 25\%$.

This result suggests that for large veins phase may not accrue linearly with TE ([Eq \[A.1.3\]](#)). Such a nonlinear relationship is possible if the extravascular phase sampled by the voxel does not sum to zero (see Discussion for details). [Fig 2.7C](#) shows the susceptibility weighted magnitude intensities ([Fig 2.4F](#)) along the cross section of the vein (same format as [Fig 2.7A](#)). SWV CNR gain was calculated to be 45%. From these results it is clear that extending the TE from TE_{-pi} to $TE_{-4pi/3}$ significantly improves the

vein-gray matter contrast for phase, magnitude, and susceptibility weighted magnitude images beyond theoretical predictions. These results suggest that extravascular susceptibility gradients do not always sum to zero which can result in increased sensitivity of vein-gray matter contrast to TE (see Discussion for details).

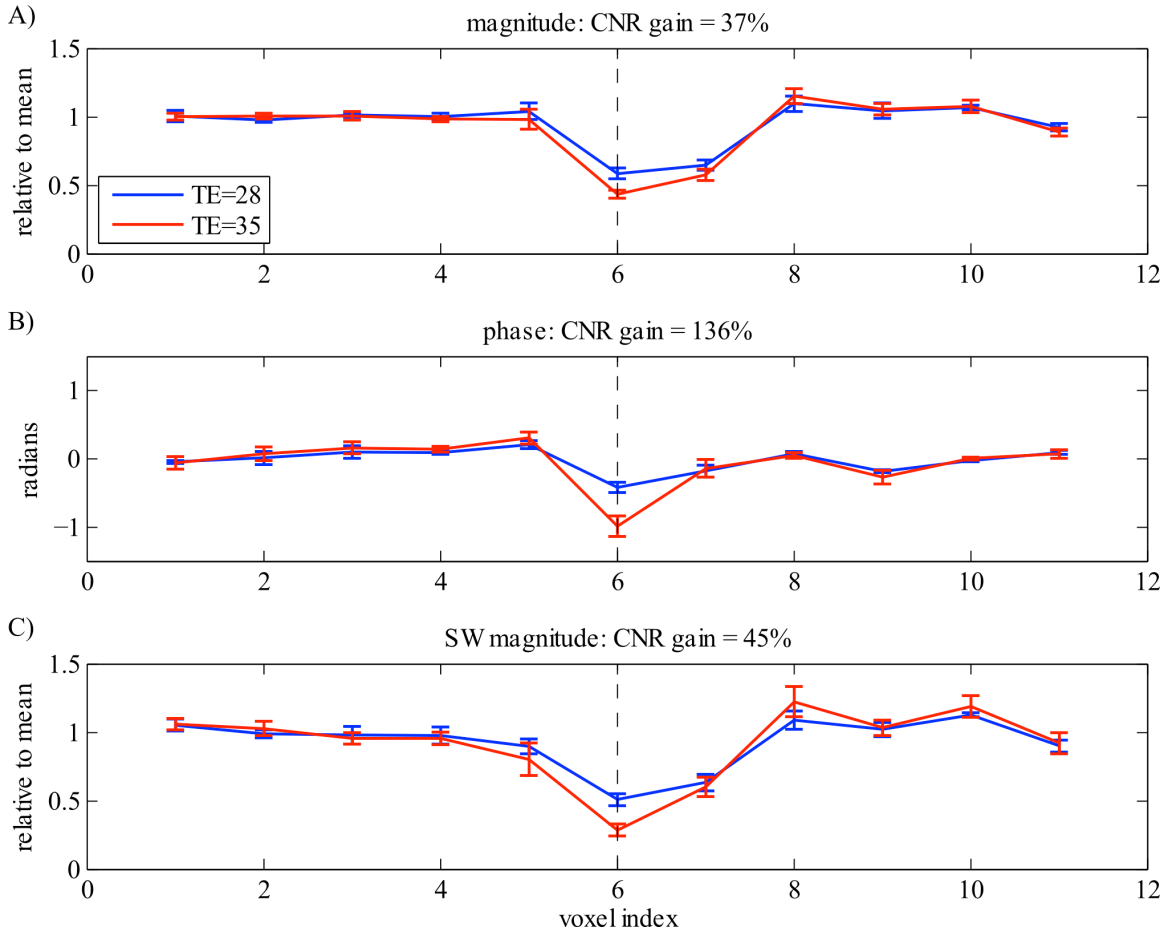


Figure 2.7. Mean cross section of voxel values in and around a typical vein near parallel with B_0 . A) Mean magnitude intensities relative to the mean gray matter intensity using $TE = TE_{-\pi} = 28\text{ms}$ (red) and extended $TE = TE_{-4\pi/3} = 35\text{ms}$ (blue). The vertical dashed line indicates the center of the vein where CNR gain was calculated. CNR gain was calculated as $[(1-\text{mag}(TE_{-4\pi/3})) - (1-\text{mag}(TE_{-\pi}))] / (1-\text{mag}(TE_{-\pi})) * 100\%$ and equaled 37% for this vein. B) Same format as the (A) but for the corresponding voxel phase values. CNR gain here was 136%. C) Same format as (A) but for the corresponding susceptibility

weighted magnitude voxel intensities. CNR gain here was 45%. Using the extended TE significantly improves vein-gray matter contrast for phase, magnitude, and susceptibility weighted magnitude images. Error bars are SE across four adjacent cross sections of the same vein.

Effect of phase transformation type

To determine if accounting for phase wrapping in a phase transformation improves vein-gray matter contrast, we first visually compared susceptibility weighted venograms based on the asymmetric phase transformation to venograms based on the tri-segment phase transformation using $TE = TE_{-4\pi/3}$. Fig 2.8A shows a typical axial slice of a susceptibility weighted venogram based on the asymmetric phase transformation. Within the slice are several phase wrapping artifacts that appear as phase-mask unpenalized bright voxels surrounded by heavily phase-mask penalized dark voxels (see voxels within red squares in Fig 2.8A). The areas containing the artifacts are shown enlarged in Fig 2.8B. Fig 2.8C shows these same areas but processed using the tri-segment phase transformation which accounts for phase wrapping in the $+\pi/2$ to $+\pi$ interval. By using the tri-segment phase transformation the phase wrapping artifacts are eliminated. Phase wrapping artifacts also appeared in the venograms collected using $TE = TE_{-\pi}$ when the asymmetric phase transformation was used. However with this shorter TE, the artifacts were generally smaller and fewer in number (Fig 2.6A). These results emphasize the importance of phase transformations that take into account phase wrapping, especially when using larger TEs for enhanced vein-gray matter contrast.

To quantify the effect of accounting for phase wrapping in the tri-segment phase transformation, we plotted the cross section of voxel values in and around a typical vein

near perpendicular with B_0 . Fig 2.9A shows the magnitude intensities along the cross section of the vein scanned with $TE = TE_{-4\pi/3} = 35\text{ms}$ (red). Fig 2.9B shows the phase intensities along the cross section of the same vein. The horizontal black line indicates the $+\pi/2$ phase value above which the asymmetric phase transformation deviates from the tri-segment phase transformation. Fig 2.9C shows the susceptibility weighted magnitude intensities along the cross section of the vein. Because the phase of this vein is within the $+\pi/2$ to $+\pi$ range, the susceptibility weighted magnitude intensity of the vein based on the asymmetric phase transformation is unpenalized (blue). However, the tri-segment phase transformation correctly penalizes the magnitude intensity of the vein (red). The vertical dashed line indicates the center of the vein where CNR gain was calculated. The CNR gain between the tri-segment and the asymmetric phase transformation for the central voxel of this vein was 37% (see Methods for details). These results demonstrate that accounting for phase wrapping is necessary to correctly weight veins with phase values wrapping in the $+\pi/2$ to $+\pi$ range. Such venous phase values are more common at longer TEs such as $TE_{-4\pi/3}$ although they can also exist at shorter TEs due to extravascular susceptibility gradients (Fig A.1.1).

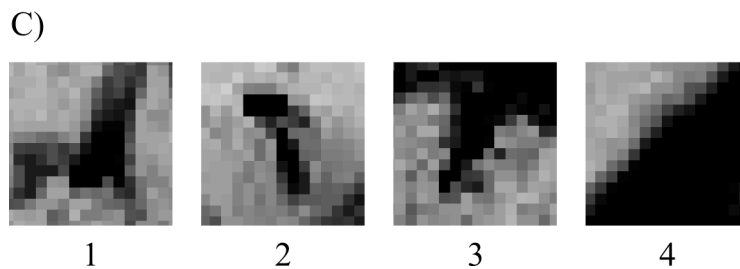
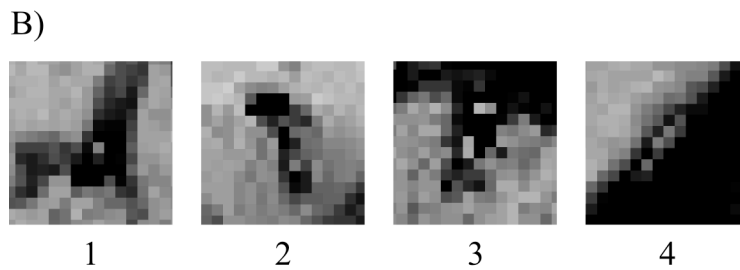
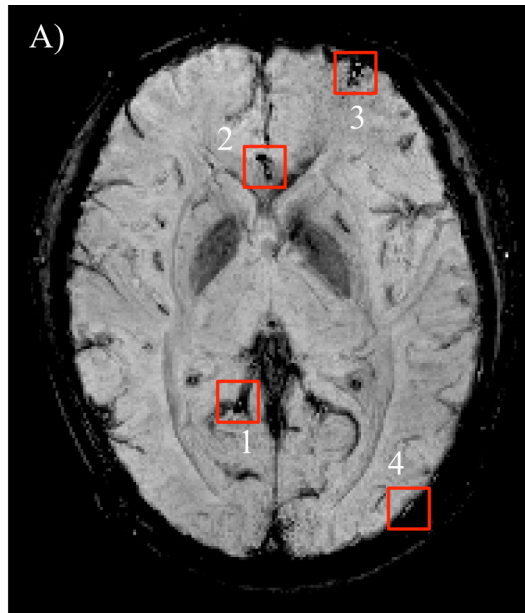


Figure 2.8. Effect of phase transformation on phase wrapping artifacts. A) SWV with $TE = TE_{-4\pi/3} = 35\text{ms}$ using the asymmetric phase transformation. Red squares indicate regions of the venogram where phase wraps in the $+\pi/2$ to $+\pi$ range. These regions exhibit phase wrapping artifacts which appear as phase-mask unpenalized bright voxels surrounded by heavily phase-mask penalized dark voxels. B) The regions marked by the red squares in (A) enlarged for detail. C) Same as (B) but using the tri-segment phase transformation. The tri-segment phase transformation eliminates the phase wrapping artifacts.

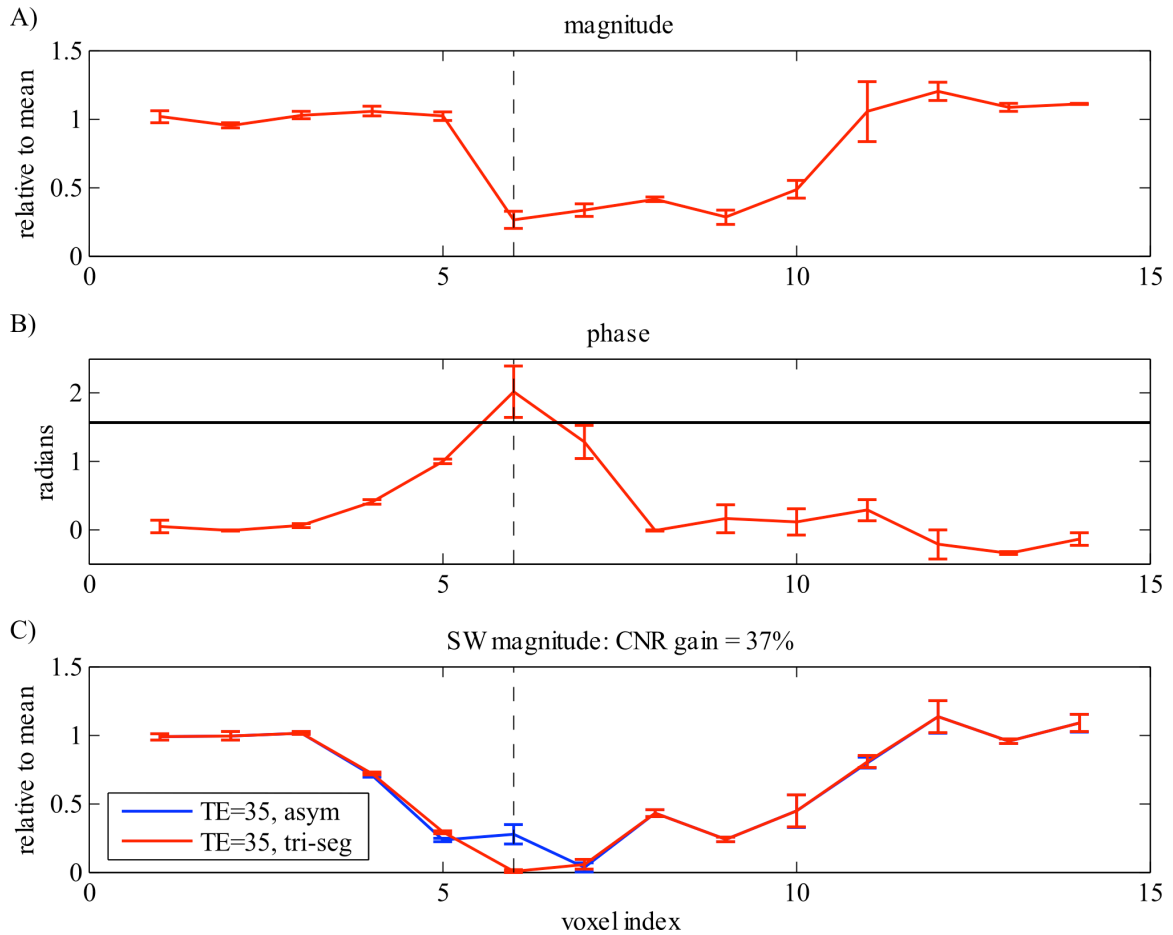


Figure 2.9. Mean cross section of voxel values in and around a typical vein near perpendicular with B_0 . A) Mean magnitude intensities relative to the mean gray matter intensity using extended TE = $TE_{-4\pi/3}$ = 35ms (red). B) Same format as the (A) but for the corresponding voxel phase values. The horizontal black line indicates the $+\pi/2$ phase value above which the asymmetric phase transformation deviates from the tri-segment phase transformation. C) Same format as (A) but for the corresponding susceptibility weighted magnitude voxel intensities based on the asymmetric phase transformation (blue) and the tri-segment phase transformation (red). The vertical dashed line indicates the center of the vein where CNR gain was calculated. CNR gain was calculated as $[(1-SWV(\text{tri-seg}))-(1-SWV(\text{asym}))] / (1-SWV(\text{asym})) * 100\%$ and equaled 37% for this vein. Using the tri-segment phase transformation significantly improves vein-gray matter contrast when phase values wrap into the $+\pi/2$ to $+\pi$ range. Error bars SE across three adjacent cross sections of the same vein.

2.4 Discussion

We presented a novel phase transformation for susceptibility weighted venography. This phase transformation, referred to as the tri-segment phase transformation, properly weights susceptibility weighted magnitude intensities even in the presence of phase wrapping. By using the tri-segment phase transformation we were able to extend the TE beyond $TE_{-\pi}$ and enhance vein-gray matter contrast in susceptibility weighted venograms. These increases in vein-gray matter contrast were much larger than predicted, suggesting that extravascular susceptibility gradients contribute to vein-gray matter contrast.

Non-optimality of $TE_{-\pi}$

As mentioned earlier, previous SWV studies used $TE_{-\pi}$ to prevent phase wrapping. In the presence of phase wrapping the phase transformations of these studies would be invalid. Our results demonstrate that by using the tri-segment phase transformation TE does not need to be limited by phase wrapping. Previous studies have also motivated the use of $TE_{-\pi}$ as a TE for optimal vein-gray matter magnitude contrast (Reichenbach et al., 2000; Reichenbach and Haacke, 2001). We argue that this motivation does not apply to veins in general but only to one special case. The logic is that with $TE = TE_{-\pi}$ dephasing (and thus signal attenuation) is maximized in voxels containing both veins and gray matter. However, this argument only holds for veins near parallel to B_0 (Fig A.1.1) and yields sub-optimal dephasing for veins at all other orientations. For maximal dephasing across veins at all orientations, we suggest the use of a TE that generates a phase distribution that spans the entire $-\pi$ to $+\pi$ range of phases (e.g. $TE_{-4\pi/3}$ or even TE_{opt} ;

Fig 2.2).

The only concern with using the entire range of phases may be phase wrapping. However, it is unclear why venograms should be limited to this phase wrapping restriction. In susceptibility weighted venography, phase is primarily used to distinguish vein from non-vein. In fact, in all previously proposed phase transformations and the one proposed here (Fig 2.3), the common logic is that voxels with greater phase accrual are more likely to contain a vein. Under this logic, it would be beneficial for the intravascular phase of veins parallel to B_0 to accrue beyond $-\pi$. This way phase contrast between gray matter and veins of most orientations can increase. This solution will be optimal as long as the overall level of distortion and drop out are acceptable given the extended TE.

If a phase transformation that accounts for phase wrapping is used, then as long as the phase of venous voxels do not alias too much (i.e. they do not approach the zero phase of gray matter) the venous voxels will still be penalized. Therefore, we suggest that longer TEs such as $TE_{-4\pi/3}$ or TE_{opt} (Table 2.1) be used for susceptibility weighted venography, along with phase transformations that take into account phase wrapping for optimal vein-gray matter contrast.

Partial volume effect as a function of TE

In quantifying the effect of extending the TE used in SWV (Fig 2.8) we discovered a nonlinear relationship between phase and TE. This is surprising because in a standard single-compartment model of susceptibility gradient strength within a voxel, theory predicts a linear relationship between phase and TE (Nishimura, 1996; Eq [A.1.3]). A

non-linear relationship between phase and TE greatly increases the importance of TE choice for susceptibility weighted imaging and potentially allows for a super-linear increase in phase contrast with a linear increase in TE.

This non-linear phase-TE relationship was found mainly in central voxels of veins whose diameter is roughly the size of a voxel. Thus it is likely that the non-linearity is due to partial volume effects that can be simulated using a two-compartment model of susceptibility gradient strength within a voxel. In a single-compartment model, the field shift due to a susceptibility gradient is constant within a voxel. Under this model, the normalized voxel signal \hat{r} as a function of time t (assuming a frequency offset of b Hz) can be expressed as:

$$\hat{r} = \hat{x} \cdot \cos(bt) + \hat{y} \cdot \sin(bt) \quad . \quad [2.1]$$

In this case, the net phase of this voxel can be expressed as:

$$phase(\hat{r}) = \arctan(\sin(bt)/\cos(bt)) = bt \quad [2.2]$$

which increases linearly with time and therefore TE.

In contrast, a two-compartment model divides a voxel into two compartments of constant but different susceptibility field shifts. In this model, protons in each compartment will tend to precess at different or even opposing frequencies. Given the spatial distribution of susceptibility gradients in and around veins (Fig A.1.1), the two-compartment model more accurately reflects voxels sampling from this distribution than the single-compartment model. Under the two compartment model, each compartment of the voxel signal, \hat{r}_1 and \hat{r}_2 , can be expressed as:

$$\hat{r}_1 = a(\hat{x} \cdot \cos(bt) + \hat{y} \cdot \sin(bt)) \quad \text{and} \quad [2.3]$$

$$\hat{r}_2 = \hat{x} \cdot \cos(-t) + \hat{y} \cdot \sin(-t) \quad . \quad [2.4]$$

For simplicity, the magnitude (specified by $a > 0$) and frequency (specified by $b > 0$) of \hat{r}_1 is taken to be relative to \hat{r}_2 which is of unit length and opposing unit frequency.

The net voxel signal is then expressed as:

$$\hat{r}_{net} = \hat{r}_1 + \hat{r}_2 = \hat{x} \cdot (a \cos(bt) + \cos(t)) + \hat{y} \cdot (a \sin(bt) - \sin(t)) \quad . \quad [2.5]$$

The net phase of this voxel can be written as:

$$phase(\hat{r}_{net}) = \arctan\left(\frac{a \sin(bt) - \sin(t)}{a \cos(bt) + \cos(t)}\right) \quad . \quad [2.6]$$

Note the net phase of a voxel under the two-compartment model no longer increases linearly with time as it did in Eq [2.2] under the single-compartment model (except when $b = -1$). This non-linear phase-time relationship is plotted in Figs 2.10A-B for various a and b values. Fig 2.10A plots the case when $b = 1$ and a varies between $\frac{1}{4}$ and 4. Fig 2.10B plot the case when $a = 2$ and b varies between $\frac{1}{2}$ and 2. The solid red and blue lines show the single-compartment phase of \hat{r}_1 as a function of TE when $b = 1$ and -1 , respectively. As a approaches 1, the non-linearity becomes more severe and approaches a step function. Under the two-compartment model, phase would initially accrue sub-linearly over time when the two compartments are roughly in phase. As the two compartments become increasingly out of phase, phase would begin to accrue super-linearly over time until the two compartments become in phase again.

To determine under what conditions the non-linearity of Eq [2.6] could produce the phase gain we observed as TE increased from $TE_{-\pi}$ to $TE_{-4\pi/3}$ (roughly seven times greater than that predicted by the single-compartment model), we calculated the derivative of the net phase of the two-compartment model with respect to time. After applying some

calculus and trigonometry, the time derivative of Eq [2.6] can be expressed as:

$$\frac{d \text{ phase}(\hat{r}_{net})}{dt} = \frac{1}{1+P^2} \cdot \frac{dP}{dt} \quad \text{where} \quad [2.7]$$

$$P = \frac{a \sin(bt) - \sin(t)}{a \cos(bt) + \cos(t)} \quad \text{and} \quad [2.8]$$

$$\frac{dP}{dt} = \frac{a^2 b - 1 + a(b-1)\cos((b+1)t)}{(a \cos(bt) + \cos(t))^2} \quad [2.9]$$

Figs 2.10C-D show Eq [2.7] plotted against TE for various values of a and b . Note, as a approaches 1, Eq [2.7] approaches a train of delta functions. When b approaches -1, Eq [2.7] approaches -1 signifying a linear phase-time relationship. Fig 2.10C plots the case when $b = 1$ and a varies between $\frac{1}{4}$ and 4. Fig 2.10D plots the case when $a = 2$ but b varies between $\frac{1}{2}$ and 2. The solid red and blue lines show the single-compartment time derivative of phase for \hat{r}_1 as a function of TE when $b = 1$ and -1, respectively. In general this non-linearity is such that the time derivative of phase becomes smaller when the two components are in phase and much larger when the components are out of phase. Figs 2.10C-D demonstrate that a voxel containing roughly equal magnitude weightings ($a \sim 1$) of two components with opposing frequencies ($b \sim 1$) generates non-linear phase-time relationships. Non-linear phase-time relationships are also generated in a voxel in which one component has relatively larger magnitude ($a > 1$) and higher frequency ($b > 1$). These non-linearities are strong enough to produce our reported relative phase gains of 137% if not greater. These results suggest that including partial volume effects between intravascular and extravascular susceptibility gradients is important for determining the TE that generates maximum phase vein-gray matter contrast.

In quantifying the effect of extending the TE used in SWV (Fig 2.8), we also discovered an additional nonlinearity in the relationship between magnitude and TE. This is surprising because in a standard one compartment model (no partial voluming), theory predicts an exponential decay of magnitude signal with TE (see Appendix A.2 and Fig 2.1; Nishimura, 1996). From this exponential decay, we expected that vein-gray matter contrast should increase by ~5% when extending the TE from the standard TE = TE_{-pi} to TE = TE_{-4pi/3}. However, in practice we found that vein-gray matter contrast increased much more than this: ~37%, over seven times the predicted gain. This result suggests an additional non-linear magnitude-TE relationship and further demonstrates the importance of TE choice in susceptibility weighted imaging.

Given that this added non-linearity was found mainly in central voxels of veins with diameter roughly the size of a voxel, it is likely that it is also due to partial volume effects. To test this, we calculated the magnitude signal dependence on TE under the two-compartment model by taking the magnitude of \hat{r}_{net} in Eq [2.5]. Figs 2.10E-F show magnitude plotted against TE for various values of a and b . The solid red and blue lines show the single-compartment vector magnitude of \hat{r}_1 as a function of TE when $b = 1$ and -1 , respectively. For simplicity exponential decay is not modeled, i.e. T2* >> TE. Intuitively the magnitude of \hat{r}_{net} is largest for TEs when the two components \hat{r}_1 and \hat{r}_2 are in phase and smaller when the components are out of phase. Increasing TE in the range of TEs where the slope of the curves in Fig 2.10E-F are negative will increase vein-gray matter contrast more than that predicted by exponential decay alone. When the frequency shifts of the two components are opposite ($b = 1$; Fig 2.10E), the slope is

negative for TE values between TE_{-pi} and $2TE_{-pi}$. This is consistent with both the symmetry of the extravascular phase shifts and with the increase in magnitude CNR observed when extending TE_{-pi} to $TE_{-4pi/3}$. In the case when $b = 1$ and the magnitude of the two components are equal ($a = 1$; black curve in Fig 2.10E), it is possible for the two components to be completely out of phase and the magnitude of \hat{r}_{net} to be zero. This additional magnitude-TE non-linearity is certainly strong enough to produce a relative magnitude gain of 37%. These results suggest that including partial volume effects between intravascular and extravascular susceptibility gradients is important for determining the TE that generates maximal vein-gray matter contrast.

There are several possible reasons that these non-linear magnitude and phase-TE relationships were not reported in previous studies. Those studies might not have had appropriate data available (scans at multiple TEs taken from the same subject) or, they might not have analyzed vein-gray matter CNR differences in the magnitude and phase images prior to SWV preprocessing. It is also possible that they selected voxels for analysis that had no partial volume non-linearities.

Broadening of detected veins with SWV

Previous SWV studies noted that extending the TE and using phase masks to weight magnitude venograms broadens the apparent diameter of detected veins (Reichenbach et al., 2000; Reichenbach and Haacke, 2001). This broadening is a concern for studies aiming to obtain precise measurements of vein diameter. In such cases, discretion should be used when determining the TE and amount of phase masking to

apply. However, in fMRI studies it is important to obtain the effective extent of veins with the same TE that is used to collect the fMRI data. Given that the TE used in fMRI studies is usually longer than $TE_{-\pi}$, the tri-segment phase transformation proposed in this study will be necessary to account for wrapping in the venograms.

Recently, studies have encouraged the use of both magnitude and phase images in the analysis of fMRI data for improved statistical power (Rowe and Logan, 2004; Rowe, 2005; Lee et al., 2007). For these studies, weighting magnitude venograms with phase masks is especially appropriate. This allows for both the magnitude and phase extents of veins to be accounted for when determining their effective size and contribution to fMRI experiments.

Conclusions

Our findings support the use of TEs greater than $TE_{-\pi}$ (the TE for $-\pi$ radians of intravascular phase accrual) and phase transformations that take into account phase wrapping for improved vein-gray matter contrast. We also find that the choice of TE can have a non-linear effect on vein-gray matter contrast not only in susceptibility weighted images but also phase and magnitude images. These results suggest that consideration of extravascular susceptibility gradients may be important for determining the TE that generates maximal vein-gray matter contrast. Future work will have to be done to determine how these non-linear relationships with TE depend on the spatial resolution and orientation of veins scanned.

This work on extended TE, phase wrapped venography allows for the collection of

venograms using the same TE as those used in fMRI studies. This allows the diameter of veins to better reflect their spatial extent and contribution to fMRI experiments. As the technology for collecting T2* weighted gradient-echo EPI images continues to improve, we suspect that the spatial resolution of fMRI images will eventually be high enough to be considered a venogram in itself. Such data would be highly valuable as the venograms would have exactly the same distortions and registration properties as the functional images. This would make the quantification of venous contributions to fMRI experiments much more accurate than current methods.

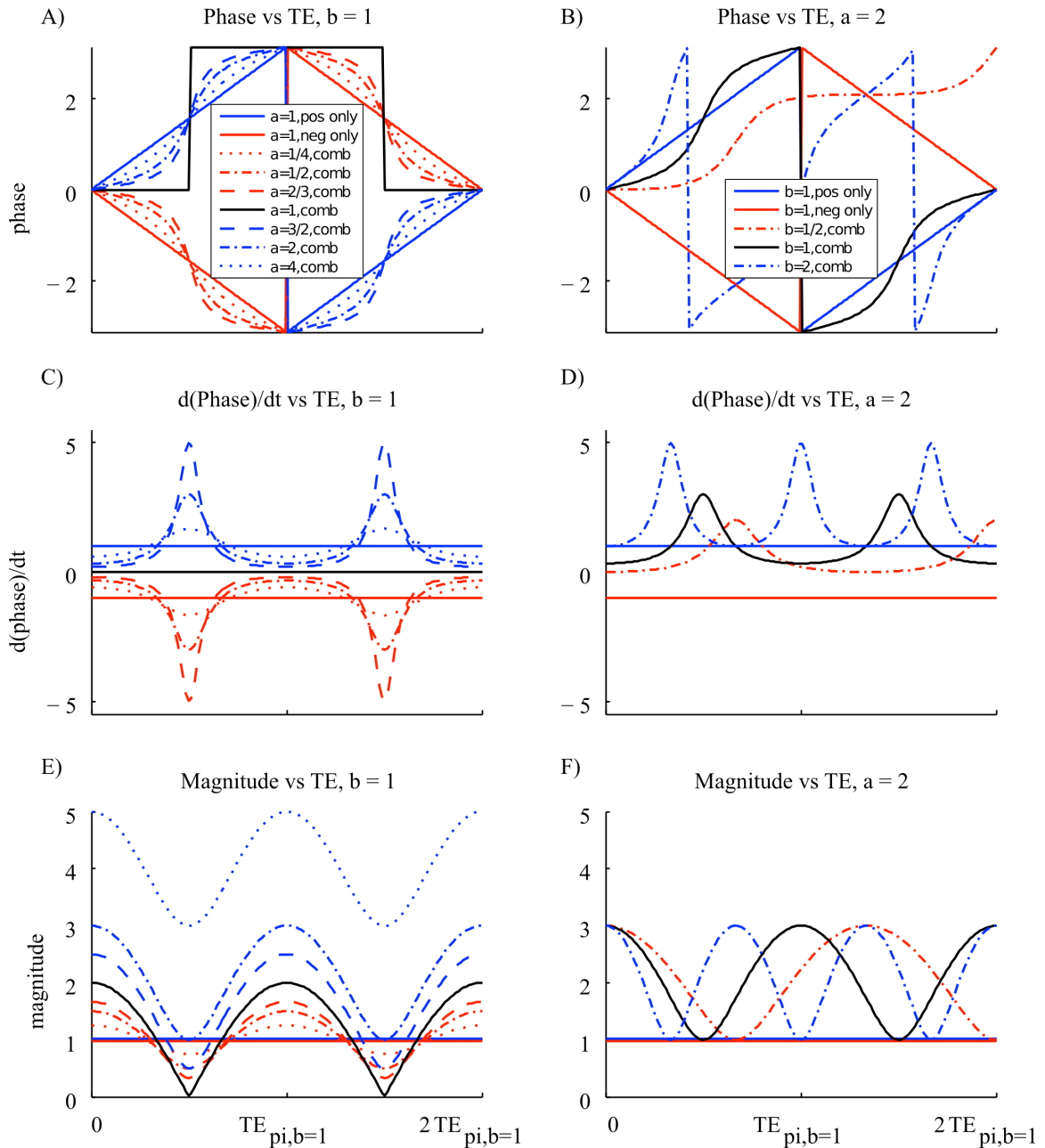


Figure 2.10. Phase and magnitude as a function of TE assuming partial volume effects in a two-compartment model. A) The non-linear phase-time relationship is plotted for $b = 1$ and a varying from $\frac{1}{4}$ to 4. The solid red and blue lines show the single-compartment phase of \hat{r}_1 as a function of TE when $b = 1$ and -1 , respectively. As a approaches 1, the non-linearity becomes more severe approaching a step function. B) Same as (A) but for $a = 2$ and b varying from $\frac{1}{2}$ to 2. C) The time derivative of phase (Eq [2.7]) plotted against TE for $b = 1$ and a varying from $\frac{1}{4}$ to 4. Note, as a approaches 1, the derivative approaches a train of delta functions. D) Same as (C) but for $a = 2$ and b varying from $\frac{1}{2}$

to 2. Note when b approaches -1 , the derivative approaches -1 (linear phase-time relationship). In general the time derivative of phase becomes smaller when the two components are in phase and much larger when the components are out of phase. E) The non-linear magnitude-time relationship plotted against TE for $b = 1$ and a varying from $\frac{1}{4}$ to 4. In general magnitude is largest when the two components are in phase and smaller when the components are out of phase. F) Same as (E) but for $a = 2$ and b varying from $\frac{1}{2}$ to 2.

Chapter 3: Combining phase and magnitude components for improved source localization in complex-valued fMRI

Blood oxygen level dependent (BOLD) signals recorded using fMRI are complex-valued, but most fMRI studies discard the phase component. Some studies have considered using both the magnitude and phase components of the BOLD signal. However, because the main source of task-related phase changes are large draining veins it has been thought that including phase would bias BOLD activity away from sites of neural activity and decrease overall information available in the BOLD signal. Here we propose a new method for combining magnitude and phase that minimizes large vein bias. Given the pattern of magnetic field distortions near large draining veins, task-related magnitude and phase changes will likely occur in neighboring voxels. Thus, we minimize bias by combining the magnitude component of individual voxels with the phase component of the neighboring voxel most correlated with it (correlation is determined using a separate data set). We call this technique: source-localized magnitude-phase combination fMRI (spamfMRI). To evaluate this method we recorded visually-evoked BOLD activity in posterior and ventral occipital-temporal visual cortex from four subjects. The visual stimuli consisted of 240 seconds of movie clips repeated ten times each. We compared four different ways of measuring BOLD activity: magnitude, phase, within voxel combination of magnitude and phase, and our source-localized phase adjacent magnitude combination. For each version we computed the F -statistic (11,108) of each voxel using the mean responses evoked by twelve movie clips. To ensure that

including phase does not decrease overall information available in the BOLD signal we also examined whether each version affected classification performance for each clip. Our results show that including the phase component of complex-valued fMRI significantly increases the F -statistics across the population of voxels by roughly 115% ($p < 0.01$). Our results also show, for the first time, that including phase significantly improves classification of natural movie stimuli ($p < 0.01$). Furthermore, we show that our spamfMRI method increases both mean F -statistic and categorization performance over what is obtained by merely combining magnitude and phase within individual voxels ($p < 0.01$). Finally, we show that our approach minimizes bias toward large draining veins. Our findings suggest that using both magnitude and phase is the most efficient way to measure BOLD activity.

3.1 Background

In magnetic resonance imaging (MRI), images are complex-valued due to spatial inhomogeneities in the magnetic field. Thus, in functional magnetic resonance imaging (fMRI), voxel timecourses are also complex-valued and can be decomposed into magnitude and phase components (Fig 3.1) (Menon, 2002; Rowe and Logan, 2004). Most fMRI studies only use the magnitude component as their measure of BOLD activity and discard the phase component (Bandettini et al., 1993; Cox et al., 1995). However, recent complex-valued fMRI studies have shown that the phase component can also be used as a measure of BOLD activity (Rowe, 2005; Lee et al., 2007). In addition to having task-related magnitude changes, the BOLD signal can also exhibit task-related phase changes

(Fig 3.2). In these studies, combining both phase and magnitude components increased the functional signal-to-noise ratio (fSNR) of the BOLD signal. fSNR here is defined as the repeatability of task-related BOLD activity quantified by the F -statistic.

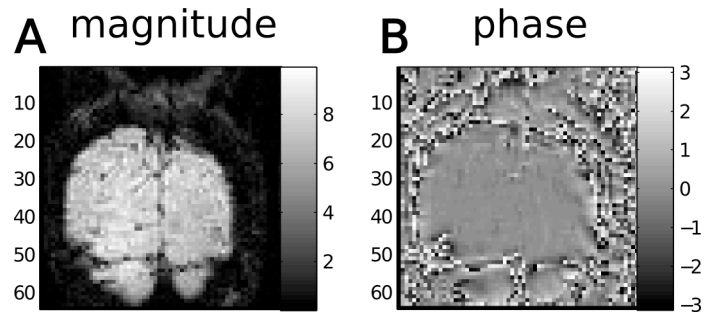


Figure 3.1. Coronal slice of a complex-valued fMRI volume. A) Magnitude component. B) Phase component.

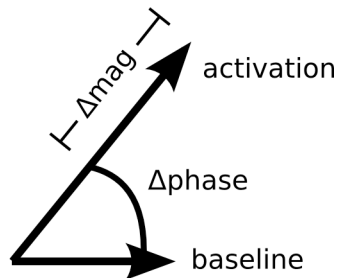


Figure 3.2. Task-related phase and magnitude changes in the complex plane.

Other studies have shown that task-related phase changes come from large draining veins (Menon, 2002; Nencka and Rowe, 2007). These studies suggest that combining phase and magnitude components in complex-valued fMRI increases bias of BOLD activity toward large veins and away from actual sites of neural activity. This increased bias of BOLD activity to large veins may also reduce overall information

available in the BOLD signal as larger veins pool over larger areas of cortex (Duvernoy, 1999; Turner, 2002). In order to reduce BOLD activity bias toward large veins, a few studies have proposed to use the phase component of complex-valued fMRI to penalize estimates of task-related magnitude changes (Menon, 2002; Nencka and Rowe, 2007). Menon (2002) penalized estimates of task-related magnitude changes based on the degree of temporal correlation between magnitude and phase in a given voxel. Nencka and Rowe (2007) penalized the estimates of task-related magnitude changes based on the size of phase variance in a given voxel. Analogous to the the way spin-echo fMRI reduces fSNR relative to gradient-echo fMRI (Boxerman et al., 1995; Duong et al., 2003), these penalized magnitude methods of measuring BOLD activity also reduce fSNR relative to the standard magnitude measure of BOLD activity. Until now, no study has yet to combine both magnitude and phase for increased fSNR while minimizing large vein bias.

Virtually all complex-valued fMRI studies to this date combine magnitude and phase within individual voxels, neglecting the spatial locations of voxels with respect to large veins (Menon, 2002; Rowe, 2005; Lee et al., 2007) . However, it is known from venography and early BOLD fMRI studies that both phase and magnitude vary as a function of position in and around veins (Ogawa et al., 1993; Haacke et al., 1995). [Fig 3.3A](#) depicts the magnetic field off resonance distribution around the cross section of a 2mm diameter vein perpendicular to the main magnetic field (simulated using the fMRI scan parameters used in this study (see Methods) and assuming a blood oxygenation of 0.54). For a voxel that encompasses a large vein roughly the size of the voxel, magnitude fSNR tends to be high while phase fSNR tends to be low. This is because for these voxels

(like the one outlined in black in [Fig 3.3A](#)) the sampled field distortions vary strongly and symmetrically around 0 Hz. However, for voxels adjacent to the vein, magnitude fSNR will be relatively low while phase fSNR will be high. This is because for these voxels (like those outlined in magenta or blue in [Fig 3.3A](#)) the sampled field distortions vary weakly and tend to be of a single polarity.

In fMRI studies where only the magnitude component of the BOLD signal is used, large vein bias is limited to voxels that contain large veins. In the case depicted in [Fig 3.3](#), this bias would lead to strong BOLD activity in one voxel (the voxel with high magnitude fSNR outlined in black, [Figs 3.3A,B](#)). However, in complex-valued fMRI studies, large vein bias is increased to include the BOLD activity around these veins. In these studies, large vein bias is not limited to voxels containing large veins but is further extended to voxels adjacent to the large veins where phase fSNR is high. In the case depicted in [Fig 3.3](#), this bias would lead to BOLD activity in not one, but five voxels (the voxel containing the vein outlined in black plus the voxels adjacent to the vein outlined in blue and magenta [Figs 3.3A-D](#).)

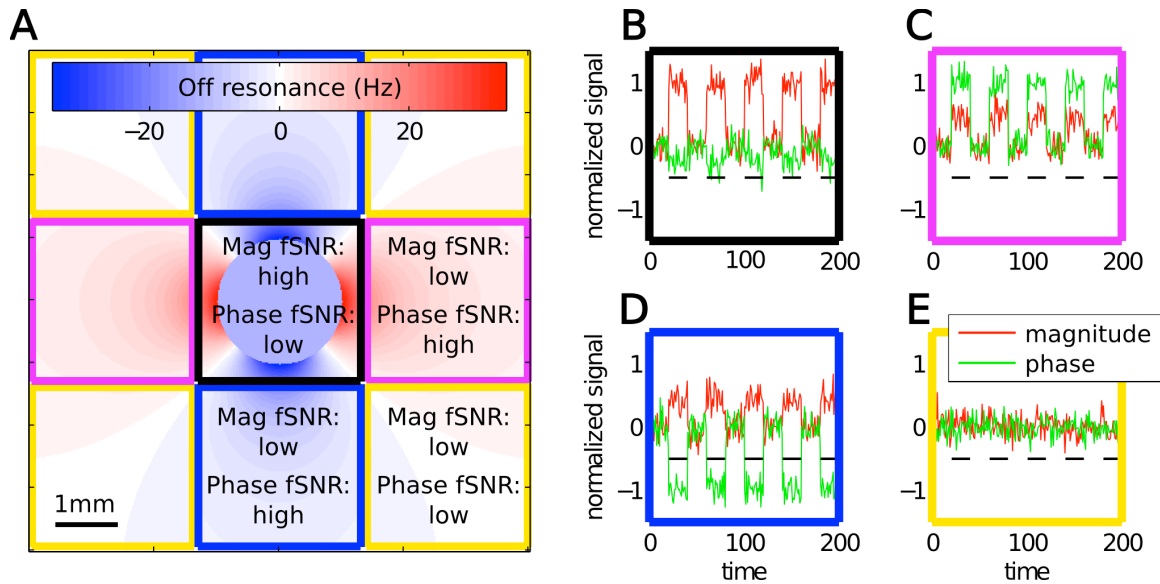


Figure 3.3. Magnitude and phase fSNR as a function of voxel position around the cross section of a large vein perpendicular to the main magnetic field. A) Magnetic field off resonance distribution around a large vein in units of Hz. This distribution is sampled by nine voxels. The voxel outlined in black covers the entire cross section of the vein. This voxel has high magnitude fSNR but low phase fSNR because the field distortions sampled by it vary strongly and symmetrically around 0 Hz. The voxels outlined in magenta and blue sample from the field distribution adjacent to the vein. These voxels have low magnitude fSNR but high phase fSNR because the field distortions sampled by them vary weakly and tend to be of a single polarity. The voxels outlined in yellow sample the portions of the field distribution that are mostly on resonance. These voxels have very little magnitude and phase fSNR. B) Simulated magnitude and phase timecourses for the voxel outlined in black in (A). The magnitude timecourse is in red, while the phase timecourse is in green. The black dashes indicate stimulus-on periods. C) Same format as in (B) but for a voxel outlined in magenta D) Same format as in (B) but for a voxel outlined in blue. Note, for this voxel, the phase timecourse is negatively correlated with the magnitude timecourse because the field distortions sampled by this voxel are mostly negative. E) Same format as in (B) but for a voxel outlined in yellow. Simulations were done assuming a typical blood oxygenation fraction change from 0.54 to 0.8. For simplicity, T2* decay effects were ignored.

We propose to utilize the spatial distribution of magnitude and phase fSNR to minimize BOLD activity bias toward large veins, while maximizing fSNR of the measured BOLD signal. The large vein bias in complex-valued fMRI stems from the

mislocalization of task-related phase changes to voxels adjacent to the source of the task-related phase changes (large veins). To minimize this bias, we propose to combine the magnitude component of individual voxels (which do not suffer from the source mislocalization just described) with the phase component of the neighboring voxel most correlated with it. We call this technique: source-localized magnitude-phase combination fMRI (spamfMRI). With this technique, the phase component is correctly applied to voxels containing the source of the task-related phase changes – large veins. Note, spamfMRI does not require the collection of venograms or the locations of veins to be predetermined. It uses the objective criterion of correlation between magnitude and phase timecourses to determine between which neighboring voxels the magnitude and phase components should be combined.

3.2 Methods

To evaluate spamfMRI we recorded visually-evoked BOLD activity in posterior and ventral occipital-temporal visual cortex from four subjects. We compared our spamfMRI method of measuring BOLD activity to three control methods: magnitude, phase, and a within voxel combination of magnitude and phase fMRI (combMRI). combMRI is exactly the same as spamfMRI except that it does not allow for combination of phase and magnitude components across neighboring voxels.

Stimuli

Stimuli were color natural movies drawn from the Apple QuickTime HD gallery

(<http://www.apple.com/quicktime/guide/hd/>) and YouTube (<http://www.youtube.com/>).

The original high-definition movies were cropped to be square. The square movie frames were then spatially down-sampled to 512 by 512 pixels. Movies were displayed using a VisuaStim LCD goggles system (20x20 degrees, 15 Hz). A colored fixation spot (4 pixels or 0.16 degree square) was presented on top of the movies. The color of the fixation spot changed three times per second to ensure that it was visible regardless of the color of the movie. Different movies were presented during collection of training and validation data sets.

MRI parameters

The experimental protocol was approved by the UCB Committee for the Protection for Human Subjects. Functional scans were conducted at UCB using a 4 Tesla Varian INOVA scanner (Varian, Inc., Palo Alto, CA) with a quadrature transmit/receive surface coil (Midwest RF, LLC, Hartland, WI). Scans were obtained using T2*-weighted gradient-echo EPI: TR 1s, TE 28ms, flip angle 56°, voxel size 2.0 x 2.0 x 2.5 mm³, and FOV 128x128 mm². The slice prescription covered 18 coronal slices beginning at the posterior pole and covering the posterior portion of occipital cortex.

Data collection

Functional data were collected from four human subjects. All subjects were healthy and had normal or corrected-to-normal vision. The data were collected in four separate 10 minute runs (2400 seconds total). Each run was constructed by concatenating

10 separate one minute movie clips and each one minute clip consisted of several smaller 10-20 second long movies. The one minute movie clips were randomly interleaved across the four runs while ensuring that each one minute clip was presented 10 times. Subjects fixated on a small spot at the center of the screen while movies were presented.

Data preprocessing

fMRI data were preprocessed as described in earlier publications (Kay et al., 2008; Naselaris et al., 2009) with the exception that both magnitude and phase components were used. Motion correction was performed using SPM '99 (<http://www.fil.ion.ucl.ac.uk/spm>), supplemented by additional custom Matlab (The Mathworks, Natick, MA) algorithms. Motion parameters were calculated from the magnitude images and then subsequently applied to magnitude and phase images separately for reslicing. Prior to motion correction of the phase images, large scale phase wrapping due to field inhomogeneities was removed with homodyne filtering (Noll et al., 1991; Reichenbach and Haacke, 2001) on a slice by slice basis. Following motion correction, for each ten minute run and each individual voxel, drift in both magnitude and phase timecourses were removed by fitting a third-degree polynomial. The timecourses were then z-scored (normalized to mean 0.0 and standard deviation 1.0).

The 240 seconds of distinct movie stimuli were divided into 24 x 10 second movie clips. For computational simplicity, the response to each clip was estimated as the mean BOLD activity over the 10 seconds of the clip. The responses to the first 12 movie clips were used as the training dataset. The responses to the second 12 movie clips were

used as the validation dataset. The training dataset was used to determine the optimal weighting of magnitude and phase components in combfMRI and spamfMRI. This dataset was also used to select high fSNR voxels from each method of measuring BOLD activity for evaluation in the validation dataset. This prevented circularity in our combfMRI and spamfMRI methods.

Data analysis

We compared four different ways of measuring BOLD activity: magnitude, phase, within voxel combination of magnitude and phase fMRI (combfMRI), and our source-localized phase adjacent magnitude combination fMRI (spamfMRI). The combfMRI measure of BOLD activity for the i th voxel at time t is given by:

$$S_i^{comb}(t) = S_i^m(t) + r \frac{F_i^p}{F_i^m} S_i^p(t) \quad [3.1]$$

where $\{S^m S^p\}$ are the z-scored magnitude and phase components of the complex-valued BOLD signal, $\{F^m F^p\}$ are the F -values calculated from the magnitude and phase components respectively and r is the sign of the correlation between S^m and S^p (correlation and F -values were determined from the training data set). Because task-related phase changes are on the order of 0.1 radians (Menon, 2002; Lee et al., 2007) we can linearly combine the magnitude and phase components. In this linear combination, the phase component is scaled by the ratio of fSNRs: F^p/F^m and multiplied by -1 one if found to be negatively correlated with the magnitude component. The optimality of this weighted sum is derived in Appendix A.3. The combfMRI method is similar to that used in prior complex-valued fMRI studies (Rowe, 2005; Lee et al., 2007) in that it does not

take into account the spatial distribution of magnitude and phase around large veins.

The spamfMRI measure of BOLD activity for the i th voxel at time t is given by:

$$S_i^{spam}(t) = S_i^m(t) + r \frac{F_{k^*}^p}{F_i^m} S_{k^*}^p(t) \quad [3.2]$$

where k^* is the index of the voxel whose phase component is most correlated with the magnitude component of voxel i . In this study, we limit k^* to be within the seven-voxel neighborhood of voxels adjacent to and including voxel i . This is exactly the same as Eq [3.1] except that the phase component used for the i th voxel may come from a neighboring voxel.

To ensure that including phase did not decrease overall information available in the BOLD signal we also examined whether each method affected classification performance for each clip using linear discriminant analysis (McLauchlan, 1992). The voxels used in the classification were selected from the training dataset as the top n fSNR voxels. To avoid bias to any one method, the voxels were chosen separately for each method of measuring BOLD activity. Standard error was determined by leave-one-repeat out cross-validation.

3.3 Results

spamfMRI yields optimal fSNR

We computed the F -statistic (11,108) of each voxel using the responses evoked by the 12 validation movie clips. This was done separately for each of the four methods of measuring BOLD activity: magnitude, phase, combfMRI, and spamfMRI. Fig 3.4 shows typical F -values on the ventral portion of one coronal slice of one subject thresholded at

$F > 10$, $p < 10^{-6}$ (Bonferroni corrected). For reference, the magnitude and phase components at one time point for the entire coronal slice is shown in Fig 3.1. Although the fSNR of the phase component (Fig 3.4 B) is much weaker than that of the magnitude component (Fig 3.4A), combining magnitude and phase within individual voxels using combfMRI increases fSNR and the number of voxels above threshold (Fig 3.4C). However, by taking into account the distribution of magnitude and phase fSNR around large veins using spamfMRI, we achieve even greater increases of fSNR and number of voxels above threshold (Fig 3.4 D).

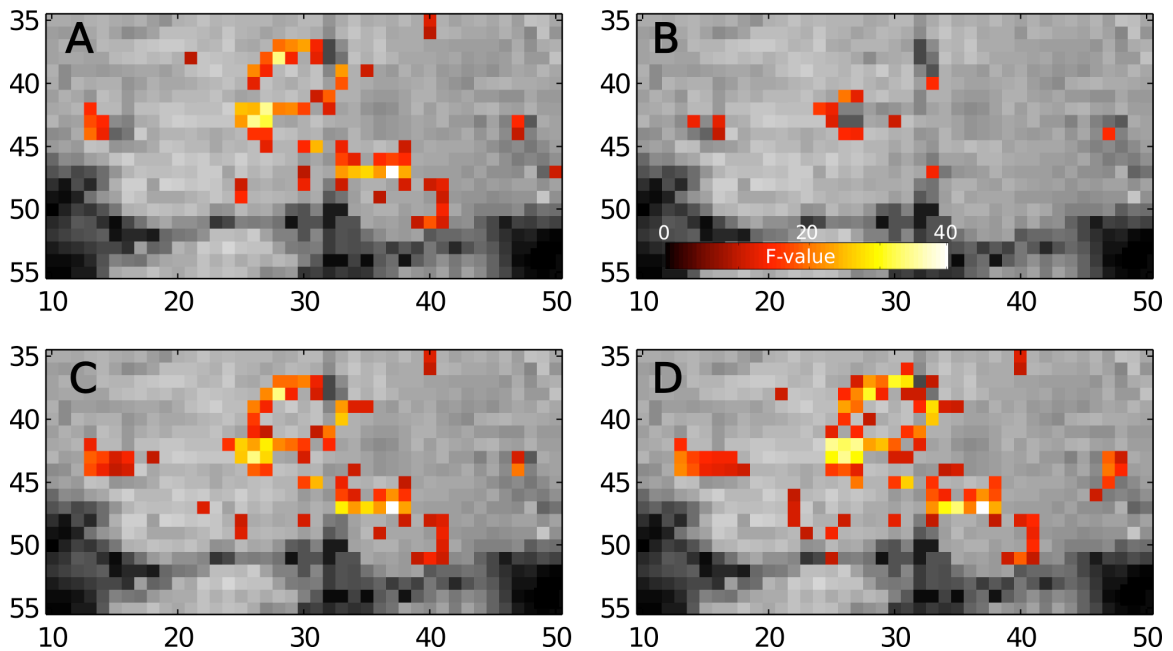


Figure 3.4. Typical fSNR calculated of the four measures of BOLD activity. A) Magnitude, B) Phase, C) combfMRI and D) spamfMRI. F -values are thresholded at $F > 10$, $p < 10^{-6}$ (Bonferroni corrected).

To further quantify the fSNR of each of the four methods of measuring BOLD

activity, we plotted the phase, combfMRI, and spamfMRI F -values against the magnitude F -values for voxels of a typical subject (Figs 3.5A,B,D). To avoid circularity, voxels plotted are those with significant magnitude or phase training F -values ($F > 10$). The F -values plotted are validation F -values. From Fig 3.5A it can be seen that fSNR tends to be much higher for the magnitude measure of BOLD activity than for the phase measure. However, the voxels that do have high phase fSNR tend to have low magnitude fSNR. This independent distribution of magnitude and phase fSNR is consistent with the large vein source of task-related phase changes (Fig 3.3). By comparing Fig 3.5B to Fig 3.5A it can be seen that combining magnitude and phase using combfMRI yields large increases in fSNR for voxels with high phase fSNR. However, by increasing the fSNR of voxels with high phase and low magnitude fSNR, combfMRI also increases the bias of BOLD activity toward large veins. By comparing Fig 3.5D to Fig 3.5A it can be seen that combining magnitude and phase using spamfMRI yields large increases in fSNR for almost all voxels. Notably, spamfMRI suppresses the fSNR of voxels with low magnitude but high phase fSNR. This is the large vein bias reducing characteristic of spamfMRI.

Fig 3.5C plots the ratio of mean phase, combfMRI, and spamfMRI F -values to mean magnitude F -value for data averaged across subjects. Error bars are SE. The phase alone had only 31 +/- 0.3 % the fSNR of the magnitude measure of BOLD activity. Both combfMRI and spamfMRI significantly ($p < 10^{-7}$ Wilcoxon signed rank test) improved fSNR relative to that of the magnitude measure of BOLD activity (by 9 +/- 2 % and 14 +/- 2%, respectively). spamfMRI also significantly increased mean fSNR relative to that of combfMRI ($p < 0.01$). The mean increase in fSNR using spamfMRI is equivalent to

collecting 14% more data in the standard fMRI experiment that only uses the magnitude component of the BOLD signal. Note our measure of fSNR is a ratio of variances so it scales linearly with (rather than to the square root of) the amount of data collected.

These results show the fSNR advantage of using spamfMRI to take into account the spatial distribution of magnitude and phase fSNR around large veins. These results also suggest that spamfMRI reduces large vein bias that is present in complex-valued fMRI methods that do not take into account the location of voxels relative to large veins.

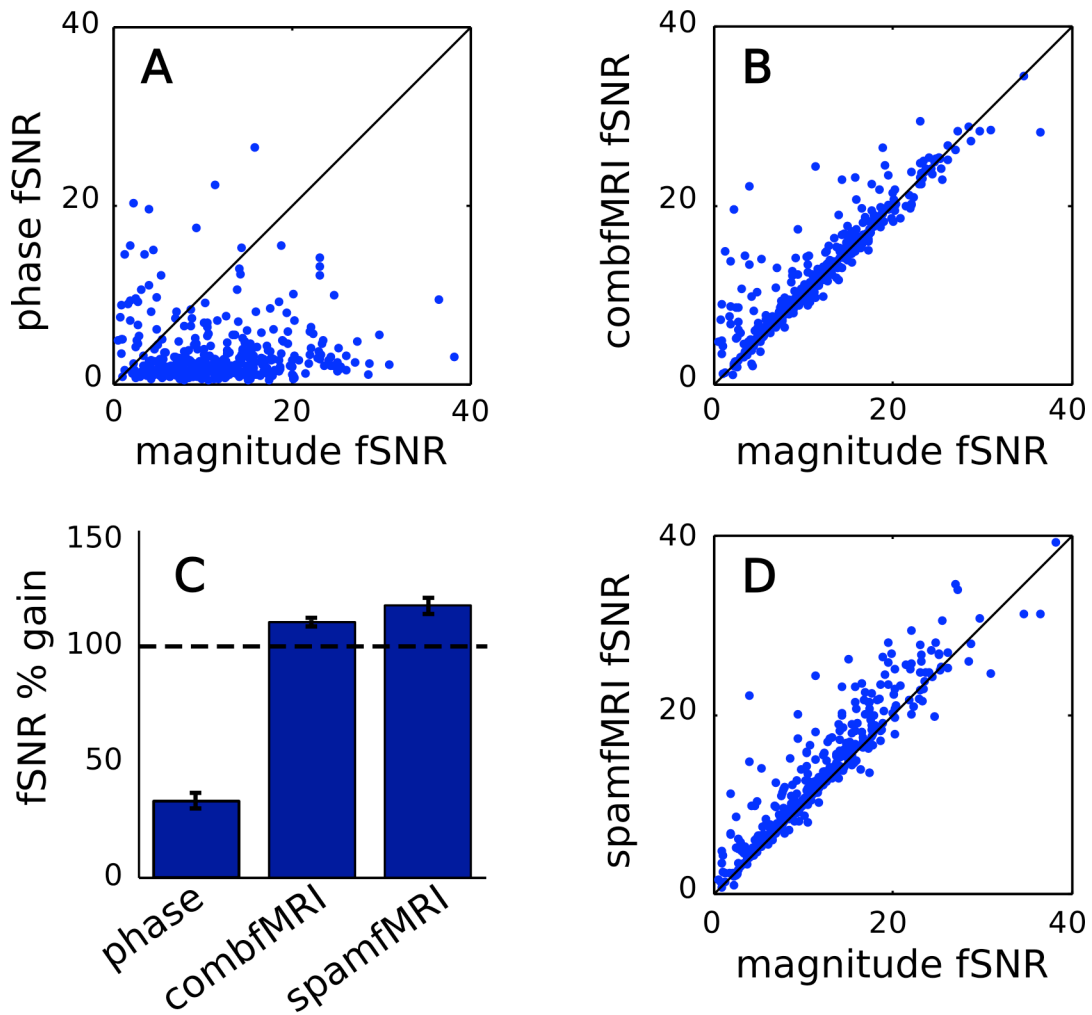


Figure 3.5. Typical fSNR improvement relative to magnitude fSNR. A,B,D) F -values for phase, combfMRI and spamfMRI plotted against magnitude F -values, respectively. combfMRI significantly improves F -values over magnitude F -values ($p < 10^{-7}$ Wilcoxon signed rank test). spamfMRI significantly improves F -values over combfMRI F -values ($p < 10^{-6}$). C) Ratio of mean phase, combfMRI, and spamfMRI F -values to mean magnitude F -value. Data are averaged across subjects. Error bars are SE.

spamfMRI reduces large vein bias

To further characterize the bias reduction properties of spamfMRI we examined the spatial distribution of fSNR around large veins in our data. Fig 3.6A shows typical magnitude and phase F -values overlaid on the ventral portion of one slice. Voxels with high phase but low magnitude F -values are colored green. Voxels with high magnitude but low phase F -values are red. Voxels with high magnitude and phase F -values are yellow. As expected given the spatial distribution of magnitude and phase fSNR around large veins, there are very few yellow voxels. Near the center of the slice, high magnitude fSNR voxels (red) are surrounded by high phase fSNR voxels (green), indicative of a large vein. Upon examination of the magnitude component of the slice Fig 3.6C, it can be seen that voxels low in intensity coincide with the high magnitude fSNR voxels. This further confirms the position of the large vein (Reichenbach et al., 1998).

Fig 3.6B demonstrates the large bias reduction characteristic of spamfMRI. spamfMRI reduces bias of BOLD activity to large veins by attributing task-related phase changes found in voxels adjacent to large veins to the source of the phase changes - the large veins. In Fig 3.6 voxels outlined in white indicate the two voxels adjacent to the large vein depicted in Fig 3.6C. These voxels are highly significant ($F > 10$) in both the

phase and combfMRI methods of measuring BOLD activity (Fig 3.4B-C, 3.6B). But because these voxels are spatially offset from the large vein source they increase the spatial extent of BOLD activity generated by the vein. With spamfMRI these voxels are not significant. Instead, spamfMRI attributes the phase changes in these voxels to adjacent voxels with correlated magnitude components that likely overlap with the large vein. The fSNR benefits of this reassignment can be seen in Fig 3.4 and Fig 3.5. Consequently, many voxels with sub-threshold magnitude fSNR become significant with spamfMRI. Fig 3.6D shows the percentage of voxels significant ($F > 10$) for all methods of measuring BOLD activity (except phase) averaged across subjects. The color scheme is the same as in Fig 3.6B. Measuring BOLD activity using the magnitude component accounts for 68 +/- 0.6% of significant voxels. Using spamfMRI to measure BOLD activity accounts for an additional 26 +/- 0.9% of all significant voxels. combfMRI accounts for 14 +/- 0.8% of significant voxels, 6 +/- 1.0% of which are voxels high in phase fSNR but low in magnitude fSNR. This 6% not accounted for by either the magnitude or spamfMRI measures of BOLD activity is the large vein bias removed when using spamfMRI. Note, although these percentages were derived using a significance threshold of $F > 10$, various thresholds were tested all which gave similar results.

spamfMRI yields optimal classification performance

To ensure that including phase from large veins did not decrease overall information available in the BOLD signal we also examined whether each method affected classification performance. Classification was performed on the 12 validation

movie clips using linear discriminant analysis (McLauchlan, 1992). For a given method of measuring BOLD activity, the top n fSNR voxels were used to evaluate classification performance. Fig 3.7A shows classification accuracy for one subject as a function of the number of voxels included in the classifier. For all subjects and methods tested (magnitude, combfMRI, and spamfMRI), peak classification accuracy was achieved with roughly 40-50 voxels. Including more than 50 voxels reduced classification performance due to the lower fSNR of the included voxels and overfitting given the limited number of repeats and number of clips to classify (Dougherty and Brun, 2006). Therefore, we compared classification accuracy across methods at $n = 40$ voxels. For the subject shown in Fig 3.7A combfMRI was found to improve classification performance relative to the magnitude method ($p < 0.01$) going from 87% to 88% correct. spamfMRI allowed for 90% of the 12 clips to be correctly classified. This was significantly better than the performance of combfMRI ($p < 0.001$). Chance performance was $1/12 = 8\%$.

Absolute percent improvement in classification performance by including phase tended to be larger for subjects with poorer classification performance. Therefore, to compare the effect of the method used on classification performance across subjects, we computed the percent error reduction of the combfMRI and spamfMRI methods relative to the magnitude method. For the subject in Fig 3.7A percent error of the magnitude method at $n = 40$ is $100-87 = 13\%$. Percent error reduction for spamfMRI would then be $(90-87)/13*100\% = 23\%$. Across all subjects, the average percent error reduction for combfMRI and spamfMRI was significantly different from zero percent ($p < 0.01$, 5% and 16% respectively). spamfMRI also significantly improved classification percent

error reduction over combfMRI ($p < 0.01$). These results suggest that including the phase component from large veins actually increases the overall information contained in the BOLD signal. These results also suggest that considering the distribution of phase and magnitude fSNR around large veins is essential for optimal use of the complex-valued BOLD signal.

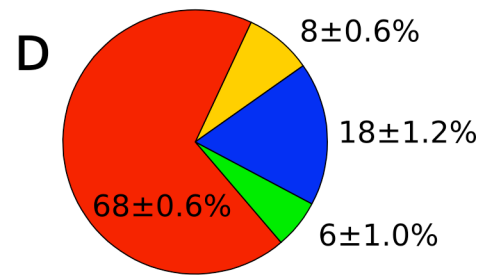
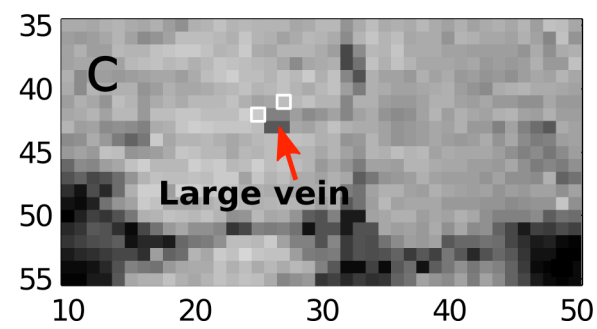
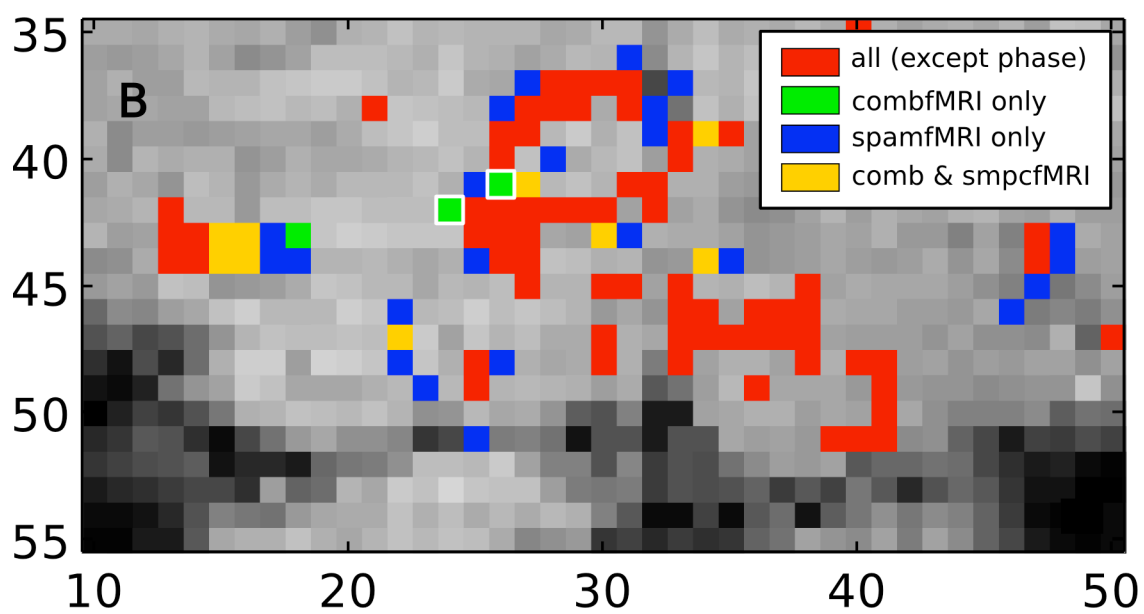
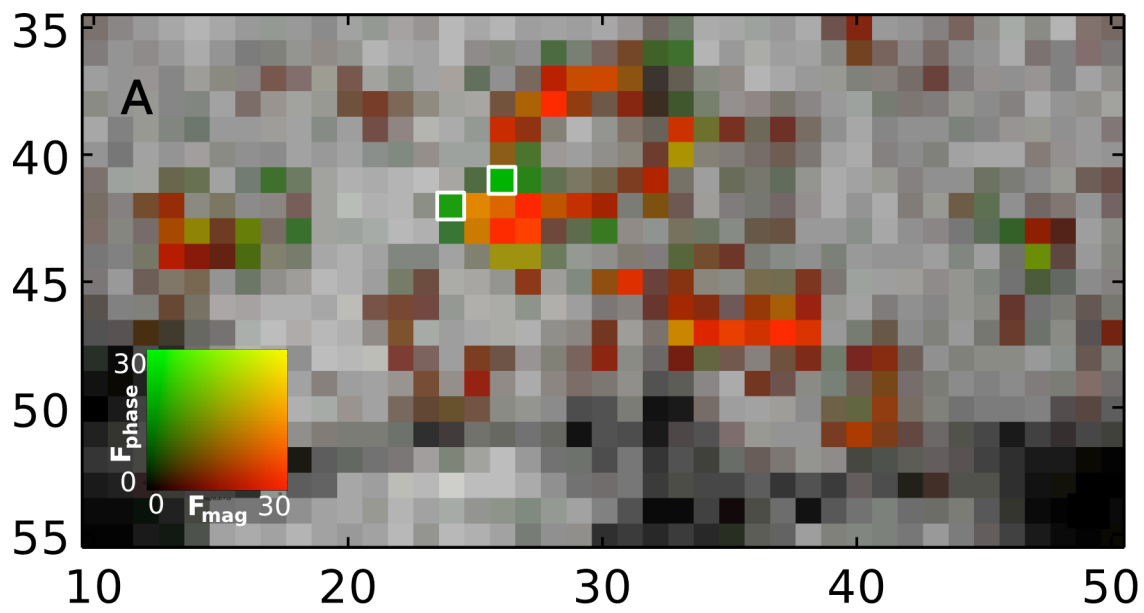


Figure 3.6. Bias reduction using spamfMRI. A) Typical magnitude and phase F -values overlaid on one slice. Green: high phase, red: high magnitude, yellow: high phase and magnitude fSNR. The lack of yellow voxels reflects independence of phase and magnitude fSNR. B) Significant voxels ($F > 10$) of all methods tested except phase. Red: all methods except phase, green: combfMRI only, blue: spamfMRI only, yellow: combfMRI and spamfMRI only. The combfMRI method increases bias to large veins (green voxels). C) Reference EPI slice. Large veins appear as dark voxels. D) Percentage of significant voxels from each method averaged across subjects. Legend same as in (B). Error is given as SE. The voxels outlined in white indicate the two voxels with highest phase F -values in the slice. These voxels adjacent to the large vein are significant using combfMRI but not significant when using spamfMRI.

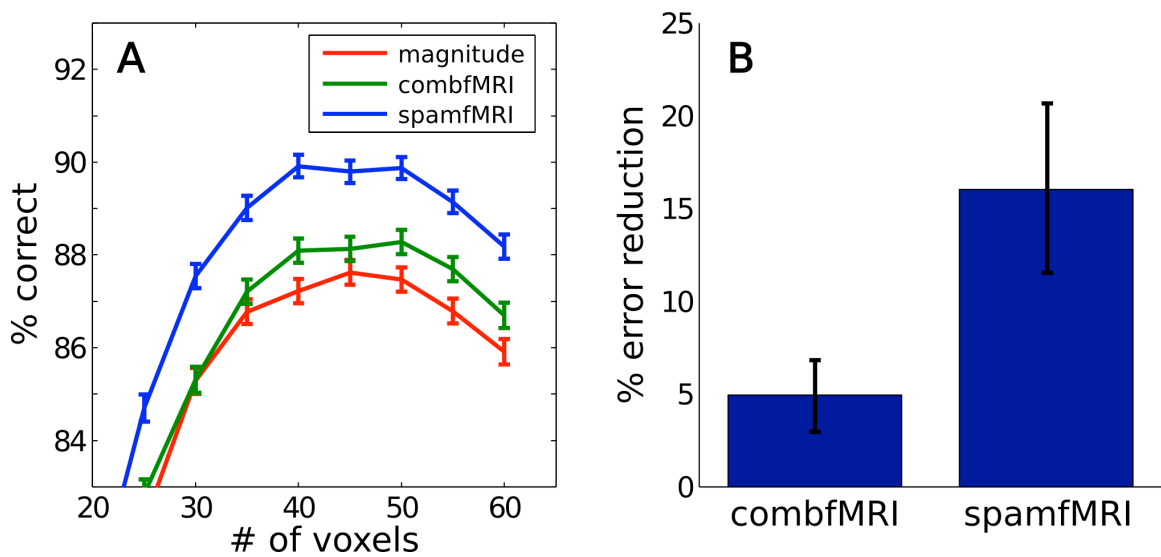


Figure 3.7. Classification performance. A) Typical classification accuracy (12 movie clips) as a function of number of voxels used for magnitude, combfMRI and spamfMRI methods. The top n F -value voxels (selected from the training dataset) were used. combfMRI improves classification performance over the magnitude method ($p < 0.01$). spamfMRI improves performance over combfMRI ($p < 0.001$). Error bars shown are cross-validated SEM. B) Classification percent error reduction relative to magnitude classification performance. Data are averaged across subjects. Error bars are SE.

3.4 Discussion

Assumptions of spamfMRI

Our spamfMRI method makes two key assumptions about the BOLD signal. The

first assumption is that magnitude and phase components of the BOLD signal are independent estimates of a single timecourse (see Appendix A.3 for details). As long as magnitude and phase are estimates of a single timecourse and have some amount of noise independent from each other, our weighted sum of magnitude and phase will yield an fSNR improved measure of BOLD activity. Previous studies on the noise of magnitude and phase components of the BOLD signal makes this first assumption a reasonable one (Petridou et al., 2009). This assumption is important because it drastically reduces the number of parameters to fit in our spamfMRI measure of BOLD activity. Previous complex-valued fMRI studies fit separate stimulus parameters for real and imaginary components of their data. Thus, although they doubled the amount of data by including the phase component of the BOLD signal, they also doubled the number of parameters that need to be fit (Rowe, 2005; Lee et al., 2007). Because our spamfMRI method assumes that the magnitude and phase components of the BOLD signal are estimates of a single timecourse, we double the amount of data but only need to fit three more parameters than standard magnitude BOLD fMRI experiments: F^m , F^p and r . In this study, we fit these parameters using a separate (training) dataset to avoid circularity in our methods comparison. However, in practice these parameters do not need to be fit on a separate dataset.

The second assumption spamfMRI makes is that one source of BOLD activity may be large veins on the order of the size of a voxel. For such large veins, high phase fSNR voxels tend to be adjacent to high magnitude fSNR voxels. This implies that voxels of high magnitude fSNR have low phase fSNR while voxels of high phase fSNR have low

magnitude fSNR. Previous complex-valued fMRI studies did not allow for this. Instead, they assumed that veins as a source of BOLD activity were small enough such that the source of the phase and magnitude changes corresponded to the same voxel (assumed only intravascular task-related phase changes) (Menon, 2002; Rowe, 2005).

The results presented here suggests the assumptions of spamfMRI are valid. If the assumptions were invalid, combfMRI would not yield improved fSNR relative to magnitude measures of BOLD activity and spamfMRI would not yield improved fSNR relative to combfMRI measures of BOLD activity.

Spatial unwrapping of phase

Spatial unwrapping of phase is a common preprocessing step in studies using the phase component of MR images (Reichenbach et al., 2000; Hammond et al., 2008). Susceptibility weighted venography studies require spatial phase unwrapping for veins to be discernible in phase images (Hammond et al., 2008). Although this is the first complex-valued fMRI study utilizing spatial phase unwrapping, we assert that spatial unwrapping of phase images is also a crucial preprocessing step for complex-valued fMRI studies. Without spatial unwrapping, phase images are contaminated by slow varying global field inhomogeneities which vary as a function of head motion, breathing, and other non-task-related effects (Reichenbach and Haacke, 2001; Petridou et al., 2009). While such effects can reduce the fSNR of the phase component, they can also introduce artifactual task-related phase changes. This can happen when breathing and/or head motion is correlated with the task. Because these artifactual task-related phase

changes are global in nature, they appear as large regions of high phase fSNR irrespective of underlying tissue type (e.g. gray matter, white matter, or vein) (Rowe, 2005; Rowe et al., 2007). Spatially unwrapping phase images eliminates such artifactual task-related phase changes and ensures that task-related phase changes are due to BOLD effects.

Spatial unwrapping of phase images is also important in complex-valued fMRI because it allows for motion correction of the phase images using the same reslicing algorithms applied to magnitude images. Subject motion has a large effect on fMRI data quality (Hajnal et al., 1994; Thacker et al., 1999). As such virtually all fMRI experiments include a motion correction preprocessing step (Oakes et al., 2005). However, because phase is a circular variable, standard motion correction algorithms cannot be applied directly to phase images. By spatially unwrapping the phase images, most phase values in the brain are close to zero (Fig 3.1B) and phase values can be approximated to be on a linear scale. Thus motion correction of the phase images can be done by reslicing unwrapped phase images based on the motion estimates from the corresponding magnitude images. Omission of the spatial phase unwrapping step would explain why prior complex-valued fMRI studies did not report the use of motion correction. However, complex-valued fMRI experiments could potentially benefit from the development and application of motion correction and co-registration algorithms designed for circular variables.

Finally, by spatially unwrapping phase images, temporal phase unwrapping becomes a less crucial part of data preprocessing. Previous complex-valued fMRI studies relied on temporal phase unwrapping due to temporal discontinuities between phase

values of $-\pi$ and π . However, temporal phase unwrapping is unreliable under low phase SNR conditions (Rowe et al., 2007). With spatial unwrapping, most phase values in the brain are close to zero. Adding the fact that task-related phase changes are on the order of 0.1 radians (Menon, 2002; Lee et al., 2007), the timecourse of spatially unwrapped phase images rarely jump between $-\pi$ and π . Thus spatial unwrapping makes temporal unwrapping of phase in complex-valued fMRI practically unnecessary.

Large vein bias reduction in spamfMRI

It should be emphasized that the spamfMRI method of measuring BOLD activity presented in this study does not reduce large vein bias relative to standard magnitude BOLD fMRI. spamfMRI is designed to minimize large vein bias relative to previous complex-valued fMRI studies by attributing task-related phase changes to neighboring voxels containing the veins that generated the phase changes. It is well known that the majority of the BOLD signal in magnitude fMRI studies comes from large draining veins (Duong et al., 2003; Hulvershorn et al., 2004). In contrast to methods that suppress BOLD activity from large veins, spamfMRI attempts to use this large vein source of BOLD activity as efficiently as possible, while preserving the rest of the magnitude BOLD activity contributed by smaller venules and capillaries.

Although spamfMRI is not a method for reducing bias of BOLD activity toward large veins relative to standard magnitude BOLD fMRI, it does give insight on ways to improve methods that are. Prior methods that use phase information to reduce large vein bias relative to standard magnitude BOLD fMRI (Menon, 2002; Nencka and Rowe,

2007) assumed the source of task-related phase and magnitude changes correspond to the same voxel. Thus, the phase component of a given voxel was only used to penalize the magnitude component of the same voxel. The results of our study suggest that phase fSNR and magnitude fSNR are independent, so that voxels with high phase fSNR tend to be spatially offset from voxels with high magnitude fSNR. Given this spatial distribution of magnitude and phase fSNR, future studies on large vein bias reduction may benefit from considering the neighborhood approach used by spamfMRI.

Magnitude and phase fSNR at higher spatial resolutions

Previous complex-valued fMRI studies reported increasing benefits of complex-valued fMRI at higher spatial resolutions. These benefits also apply to spamfMRI. In general, fSNR per voxel is linearly proportional to voxel volume. Incorporating the phase component of the BOLD signal can help make up for some of the signal loss at higher spatial resolutions. This is especially true in the presence of large veins. Under this condition the relationship between fSNR and voxel volume becomes non-linear (Fig 3.3A). As spatial resolution increases, the field distortions sampled by a given voxel vary less. With less field variation within a voxel, less signal dephasing can take place and thus magnitude fSNR decreases. This decrease in magnitude fSNR is in addition to the linear decrease due to reduced volume of protons within a voxel. But because the field distribution varies less, more net task-related phase changes are possible. Thus some voxels would actually see an increase in phase fSNR as spatial resolution increases. This is analogous to the partial volume effect on magnitude fSNR as a function of voxel size

(Geyer et al., 1999; Geissler et al., 2005; Weibull et al., 2008). Therefore we expect the benefits of spamfMRI to increase when applied to higher resolution fMRI studies.

Simplifying complex-valued fMRI

Previous complex-valued fMRI methods require the use of special complex regression analysis to handle the phase and magnitude (2D) timecourses (Rowe, 2005; Rowe et al., 2007; Lee et al., 2007). However, our spamfMRI method for combining phase and magnitude can be interpreted as utilizing the phase component of BOLD activity to generate an fSNR-enhanced version of the magnitude component. This fSNR-enhanced magnitude component can then be subjected to the exact same statistical analysis performed on standard magnitude measures of BOLD activity. In other words, spamfMRI is compatible with standard magnitude fMRI analysis pipelines.

Conclusions

In this study, we introduced a novel method for measuring complex-valued BOLD activity that takes into consideration the distribution of magnitude and phase fSNR around large veins. We showed that this method, spamfMRI, improves fSNR over previous measures of BOLD activity. We also showed that using spamfMRI to combine magnitude and phase actually increased the overall information available in the BOLD signal as measured by movie clip classification accuracy. Finally we showed that spamfMRI can reduce bias toward large veins by attributing task-related phase changes to neighboring voxels likely to contain the large vein that generated those changes.

As fMRI experiments utilize higher spatial resolutions, the distribution of phase and magnitude fSNR will become important for a wider range of vein sizes. Thus, we expect that the benefits of spamfMRI will only increase when applied to future fMRI studies.

Chapter 4: The vascular contribution to semantic category area localization in BOLD fMRI

Numerous studies have shown that gradient-echo blood oxygen level dependent (BOLD) fMRI is biased toward large draining veins. However, the impact of this large vein bias in the localization and measurement of semantic category areas has not been examined. Here we address this issue by comparing standard magnitude measures of BOLD activity in FFA and PPA to those obtained using a novel method that suppresses the contribution of large draining veins: source-localized phase regressor (sPR). Unlike previous suppression methods that utilize the phase component of the BOLD signal, sPR yields robust and unbiased suppression of large draining veins even in voxels with no task-related phase changes. This is confirmed in ideal simulated data as well as in FFA/PPA localization data from four subjects. We find that approximately 38% of right PPA, 14% of left PPA, 16% of right FFA, and 6% of left FFA voxels predominantly reflect signal from large draining veins. Surprisingly, with the contributions from large veins suppressed we also find that semantic category representation in PPA actually tends to be lateralized to the left rather than the right hemisphere. Furthermore we find that semantic category areas larger in volume and higher in fSNR tend to have more contributions from large veins. These results suggest that previous studies using gradient-echo BOLD fMRI were biased toward semantic category areas that receive relatively greater contributions from large veins.

4.1 Background

Studies using BOLD fMRI rely on the assumption that differences in strength of task-related BOLD activity reflect differences in strength of underlying neural activity. Comparisons of BOLD activity to neural activity in individual regions of cortex have warranted this assumption (for review see Logothetis and Wandell, 2004). However, studies on the representation of semantic categories often assume that BOLD fMRI can be used to infer neural differences across cortical regions and across subjects. This assumption may be unwarranted. Given the bias of BOLD fMRI toward large veins, BOLD activity differences across cortical regions and across subjects may simply reflect differences in vein size (Lai et al., 1993; Haacke et al., 1994; Kim et al., 1996; Jochimsen et al., 2004).

In spite of the bias toward large veins, fMRI studies comparing BOLD activity across cortical regions have strongly shaped our understanding of semantic representation in the human brain. Early studies suggested that distinct areas of cortex are responsible for the representation of specific semantic categories: faces (Kanwisher et al., 1997), places (Epstein et al., 1998), and body parts (Downing et al., 2001). However, areas selective for other semantic categories have yet to be discovered and much of visual cortex remains to be functionally characterized (Downing et al., 2006; Spiridon et al., 2006; Reddy and Kanwisher, 2006). These results led to the hypothesis that representation of other semantic categories are not represented in cortical areas but by the fine scaled pattern of activity across cortex (Haxby et al., 2001; Ewbank et al., 2005). However, because gradient-echo BOLD fMRI is biased toward large veins, the rarity of

semantic category areas may simply reflect a bias in the distribution of vein size toward specific regions of interest (ROIs).

Studies using gradient-echo BOLD fMRI have also suggested that semantic category representation is right hemisphere lateralized (Kanwisher et al., 1997; Epstein and Kanwisher, 1998; Downing et al., 2006; Spiridon et al., 2006). In these studies, right PPA tends to be larger in size and higher in functional SNR (fSNR, measured using appropriate *t*-value contrasts) than left PPA. FFA tends to be even more right hemisphere lateralized than PPA. In addition to finding right FFA larger in size and higher in fSNR than left FFA, for some subjects the left FFA is not found at all (Kanwisher et al., 1997; Yovel and Kanwisher, 2004; Spiridon et al., 2006). These results suggest that semantic representation in the human brain is heavily right hemisphere lateralized. However, because BOLD fMRI is biased toward large veins, the laterality of semantic representation may simply reflect the general trend that veins are larger in the right hemisphere (Di Chiro, 1972; Durgun et al., 1993; Ayanzen et al., 2000; Stoquart-ElSankari et al., 2009). Thus, we hypothesize that the laterality and apparent paucity of semantic category areas are due to bias in the distribution of vein size toward specific regions of interest (ROIs). If our hypothesis is true, ROIs larger in size and higher in fSNR will have larger contributions from large veins.

To evaluate this hypothesis we first develop a novel method for suppressing the large vein contribution to BOLD activity: source-localized phase regressor (sPR). We then measure ROI size and fSNR with and without large vein suppression to quantify the amount of large vein contribution to individual ROIs. sPR builds upon the phase

regressor (PR) large vein suppression method developed by Menon (2002) with two key improvements (see Large vein suppression methods for details). First, sPR utilizes an unbiased least squares loss function to avoid the overcorrection of large vein contributions reported by Nencka and Rowe (2007). Second, sPR utilizes task-related phase changes in neighboring voxels to suppress large vein contributions in voxels with poor phase fSNR. Thus sPR is able to suppress large veins roughly the size of a voxel, as well as those near the magic angle (i.e. the angle, $\sim 54^\circ$, between a vein and B_0 which results in zero intravascular phase accrual; Reichenbach et al., 2000; Menon, 2002). Together, these improvements allow sPR to yield robust, unbiased suppression of large vein contributions even in voxels with no task-related phase changes.

The first portion of our study validates the sPR method by comparing it to the original PR method under various simulated magnitude and phase fSNR conditions. Through this simulation we demonstrate that sPR yields robust and unbiased suppression of large vein contributions. The second portion of our study compares standard magnitude measures of BOLD activity in FFA and PPA to those obtained using sPR large vein suppression. Through this study, we quantify the large vein contributions to individual ROIs and reveal the relationship between ROI size, fSNR and large vein contributions. We also discuss how our results affect interpretation of BOLD activity measured using gradient-echo BOLD fMRI.

4.2 Large vein suppression methods

Previous studies have developed methods for suppressing large vein contributions

to BOLD activity using standard gradient-echo pulse sequences (Menon, 2002; Nencka and Rowe, 2007). In contrast to most BOLD fMRI studies that only use the magnitude component of the BOLD signal, these large vein suppression methods utilize the entire complex-valued BOLD signal: both magnitude and phase components (Fig 4.1). Taking note that task-related phase changes come exclusively from large veins, these large vein suppression techniques penalize task-related magnitude changes based on the amount of task-related phase changes in a given voxel. These techniques are attractive because they do not require pulse sequence modification or reductions in spatial/temporal resolution. However, these techniques have limitations. Nencka and Rowe (2007) cautioned against the use of these large vein suppression techniques given their tendency to over- or under-correct for large vein contributions. Furthermore, these large vein suppression techniques assume that voxels containing large veins will have high phase fSNR. This assumption begins to breakdown for large veins roughly the size of a voxel as well as for veins near the magic angle (Reichenbach et al., 2000; Menon, 2002). Because these large vein suppression methods depend on task-related phase changes, low phase fSNR voxels will be poorly suppressed.

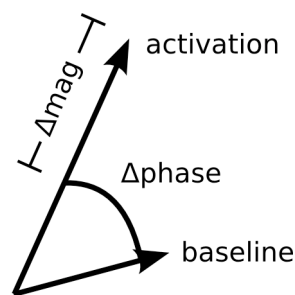


Figure 4.1. Task-related phase and magnitude changes in the complex plane.

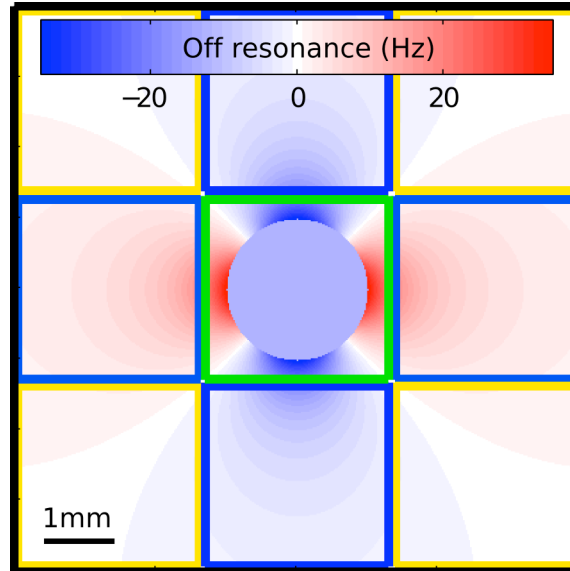


Figure 4.2. Magnetic field off resonance distribution around the cross section of a large vein perpendicular to the main magnetic field. This is a simulation calculated using the venogram scan parameters in our study and assuming a typical blood oxygenation fraction of 0.54 (Haacke et al., 1995). The distribution is sampled by ten voxels: nine small and one large. The small voxel outlined in green covers the entire cross section of the vein but samples only a limited portion of the off resonance distribution. This voxel has high magnitude fSNR but low phase fSNR because the field distortions sampled by it vary strongly and symmetrically around 0 Hz. The small voxels outlined in blue sample from the field distribution adjacent to the vein. These voxels have low magnitude fSNR but high phase fSNR because the field distortions sampled by them vary weakly and tend to be of a single polarity. The voxels outlined in yellow sample portions of the field distribution that are mostly on resonance. These voxels have very little magnitude and phase fSNR. The large voxel outlined in black covers the entire cross section of the vein and samples most of the off resonance distribution. This voxel, as the one outlined in green, has high magnitude fSNR but low phase fSNR. Large voxels adjacent to this voxel outlined in black would sample mostly on resonance portions of the field distribution. They would have very little magnitude and phase fSNR.

To address these limitations, we developed our own unbiased and robust method

for large vein suppression based on the phase regressor (PR) method of Menon (2002). As in Menon (2002), we define the large vein suppressed microvascular BOLD signal, S^{micro} , as the magnitude component of the BOLD signal, S^m , minus the large vein macrovascular BOLD signal, S^{macro} . Thus, S^{micro} can be mathematically expressed as:

$$S^{micro} = S^m - S^{macro} \quad [4.1]$$

S^{macro} is defined as the linear least-squares fit of the phase component of the BOLD signal, S^p , to the magnitude component, S^m . Mathematically, S^{macro} can be expressed as:

$$S^{macro} = b_0^* + b_1^* S^p \quad [4.2]$$

where

$$b_0^*, b_1^* = \arg \min_{b_0, b_1} L(b_0, b_1) \quad [4.3]$$

In Menon (2002) the chi squared loss function was used:

$$L_{ChiSq}(b_0, b_1) = \sum_{t=1}^N (S^m(t) - b_0 - b_1 S^p(t))^2 / (\sigma_m^2 + b_1^2 \sigma_p^2) \quad [4.4]$$

Minimizing L_{ChiSq} with respect to b_0 and b_1 yields the PR measure of BOLD activity for the i th voxel at time t given by:

$$S_i^{PR}(t) = S_i^m(t) - b_1^* S_i^p(t) \quad [4.6]$$

where

$$b_1^* = -B + \sqrt{(B^2 - 4AC)} / (2A) \quad [4.7]$$

$$A = r \sum (S^m)^2 / 2 \quad , \quad [4.8]$$

$$B = \sum (S^p)^2 - r \sum S^m \quad , \quad [4.9]$$

$$C = -(\sum (S^p S^m) + r \sum (S^m)^2) / 2 \quad , \quad [4.10]$$

and

$$r = \text{sign}(\text{corr}(S^m, S^p)) \quad . \quad [4.11]$$

S^m and S^p are the z-scored magnitude and phase components of the complex-valued BOLD signal, respectively. $\text{corr}(S^m, S^p)$ is the temporal correlation between S^m and S^p and is calculated from a separate run in our FFA/PPA localization experiment. The PR method derived here is identical to the method used in Menon (2002) except that a linear (as opposed to quartic) b_1 term is used in the denominator of the loss function. This allows us to express b_1^* in closed form. However, because L_{ChiSq} includes b_1 in the denominator, b_1^* and therefore S^{macro} tends to be overestimated. To address this, we used the unbiased ordinary least squares loss function:

$$L_{OLS}(b_0, b_1) = \sum_{t=1}^N (S^m(t) - b_0 - b_1 S^p(t))^2 \quad . \quad [4.12]$$

Because L_{OLS} does not include b_1 in the denominator, it does not overestimate S^{macro} .

To address the poor suppression of large veins roughly the size of a voxel and those near the magic angle, we take advantage of the magnitude and phase fSNR distribution around such veins (Fig 4.2). Voxels that contain a large vein roughly the size of a voxel (as the one outlined in green in Fig 4.2) have high magnitude but low phase

fSNR. This is because the field distortions sampled by these voxels vary strongly and symmetrically around 0 Hz. Intravascular task-related phase changes in these voxels will contribute minimally due to the short T2* of venous blood relative to that of the parenchyma (Reichenbach and Haacke, 1998). Thus, using the weak task-related phase changes in these voxels yields poor suppression. However, voxels adjacent to veins (as the ones outlined in blue in Fig 4.2) have low magnitude but high phase fSNR. This is because the field distortions sampled by these voxels vary weakly and tend to be of a single polarity. By using the high phase fSNR from these vein-adjacent voxels, we can correctly suppress BOLD activity from large vein containing voxels with poor phase fSNR. Because veins are the source of the high phase fSNR in the vein-adjacent voxels, we call our novel technique: source-localized phase regressor (sPR).

Minimizing L_{OLS} with respect to b_0 and b_1 yields the sPR measure of BOLD activity for the i th voxel at time t given by:

$$S_i^{sPR}(t) = S_i^m(t) - \text{corr}(S_i^m, S_{k^*}^p) S_{k^*}^p(t) \quad [4.13]$$

where k^* is the index of the voxel whose phase component is most correlated with the magnitude component of voxel i . In our simulation study, we limit k^* to be i (a one-voxel neighborhood) so that the difference in loss function between PR and sPR is directly compared. However, in order to suppress large vein containing voxels with poor phase fSNR in our FFA/PPA localization study we allow k^* to be within the seven-voxel neighborhood of voxels adjacent to and including voxel i .

4.3 Computer simulation study

To verify that sPR suppresses BOLD activity from large veins without overcorrection, here we compare PR and sPR suppression of simulated complex-valued BOLD activity.

Methods

Simulated BOLD activity was generated with 14 alternating 16 second stimulus-off and stimulus-on blocks using Matlab (The Mathworks, Natick, MA). For simplicity, the hemodynamic response function was modeled as a unit impulse function with zero delay. The expected fSNR of both magnitude and phase timecourses was varied from 0 to 10 in steps of 0.1. Expected fSNR is defined as: $(\mu_{on} - \mu_{off}) / \sigma_{noise}$, where μ_{on} and μ_{off} are the expected responses to stimulus-on and stimulus-off conditions, respectively and σ_{noise} is the expected standard deviation of the normally distributed noise. For each method of suppression, one simulation was done for each pair of magnitude and phase fSNR yielding a total of $2 \times 101 \times 101 = 20402$ simulations. fSNR of the simulated large vein suppressed BOLD activity was calculated as

$(\bar{S}_{on} - \bar{S}_{off}) / (\text{std}(S_{on})/2 + \text{std}(S_{off})/2)$, where \bar{S}_{on} and \bar{S}_{off} are the mean responses to stimulus-on and stimulus-off conditions, respectively. Averaging across repeated simulations was not done to preserve the random effect of noise under low fSNR conditions.

Results

To study the effect of loss function on large vein suppression, we compared PR

and sPR suppression of simulated complex-valued BOLD activity. This was done for various magnitude and phase fSNR conditions. Fig 4.3 shows the simulation of large vein suppression in a voxel containing a large vein. In this regime, both the phase and magnitude fSNR are high (t -value = 5.16, t -value = 5.08, respectively; Figs 4.3A,B). The linear fits of phase to magnitude using L_{ChiSq} (blue) and L_{OLS} (cyan) loss functions are plotted in Fig 4.3B. Using L_{ChiSq} yields larger absolute fits (e.g. larger b_1^* values). In this regime, both PR (blue, Fig 4.3C) and sPR (cyan, Fig 4.3D) yield good suppression of BOLD activity. However, PR exhibits slightly stronger suppression than sPR (t -value = 0.25 versus t -value = 0.50, respectively).

Fig 4.4 shows the simulation of large vein suppression in a voxel with no large vein contribution. In this regime, phase fSNR is low while magnitude fSNR is high (t -value = -0.10, t -value = 5.21, respectively; Figs 4.4A,B). The linear fits of phase to magnitude using L_{ChiSq} (blue) and L_{OLS} (cyan) loss functions are plotted in Fig 4.4B. Using L_{ChiSq} in this regime also yields larger absolute fits (e.g. larger b_1^* values). Both PR (blue, Fig 4.4C) and sPR (cyan, Fig 4.4D) yield good preservation of the magnitude BOLD activity. This is the desired effect in this regime because there is no large vein contribution. However, PR does exhibit some unwanted suppression while sPR does not (t -value = 4.38 versus t -value = 5.16, respectively).

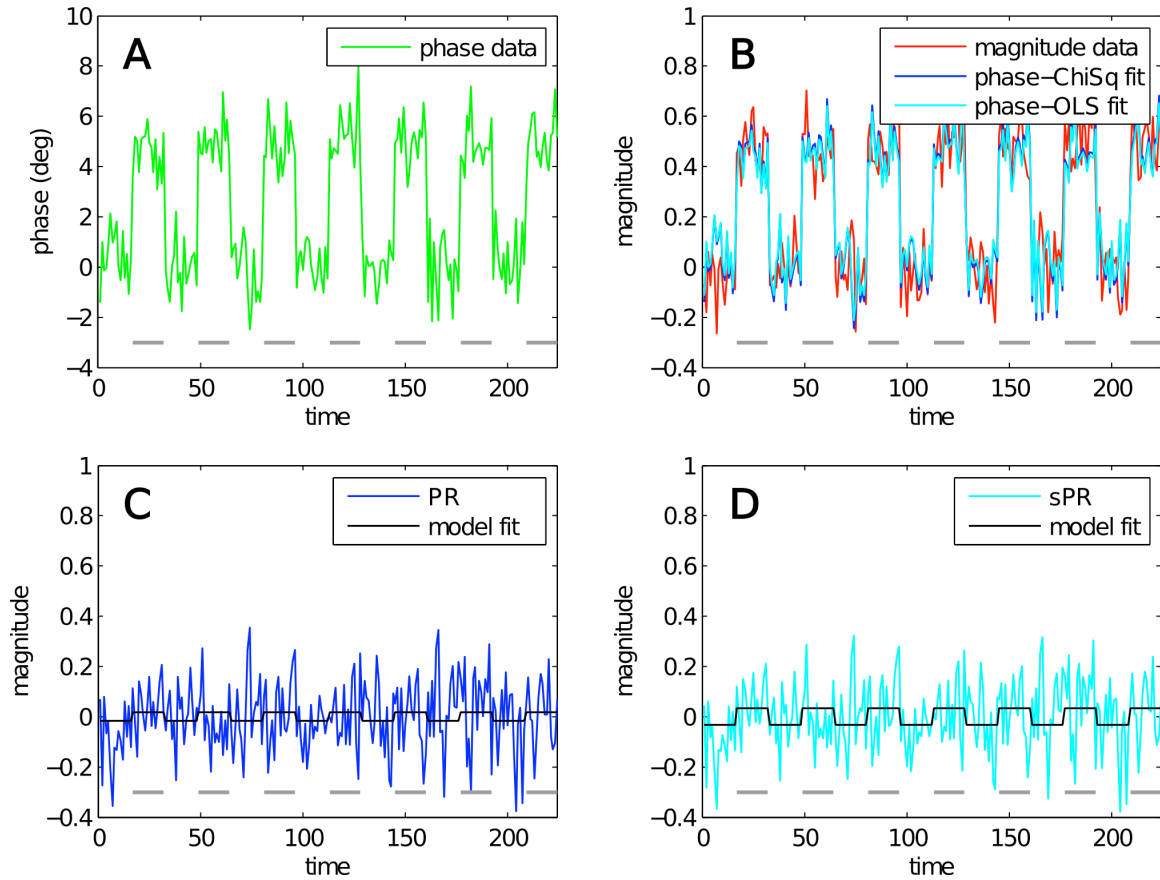


Figure 4.3. Simulated large vein suppression in a voxel containing a large vein. In this regime, both phase and magnitude fSNR are high. A) Phase timecourse is plotted in green (t -value = 5.16). Gray dashes indicate stimulus-on periods. B) Magnitude timecourse is plotted in red (t -value = 5.08). Linear fits of phase to magnitude using L_{ChiSq} and L_{OLS} are plotted in blue and cyan, respectively. Using L_{ChiSq} yields larger absolute fits (e.g. larger b_1^* values). C) PR large vein suppressed timecourse is plotted in blue (t -value = 0.25). PR model fit timecourse is plotted in black. D) sPR large vein suppressed timecourse is plotted in cyan (t -value = 0.50). sPR model fit timecourse is plotted in black. In this regime, both PR and sPR show good suppression of BOLD activity. PR exhibits slightly stronger suppression than sPR.

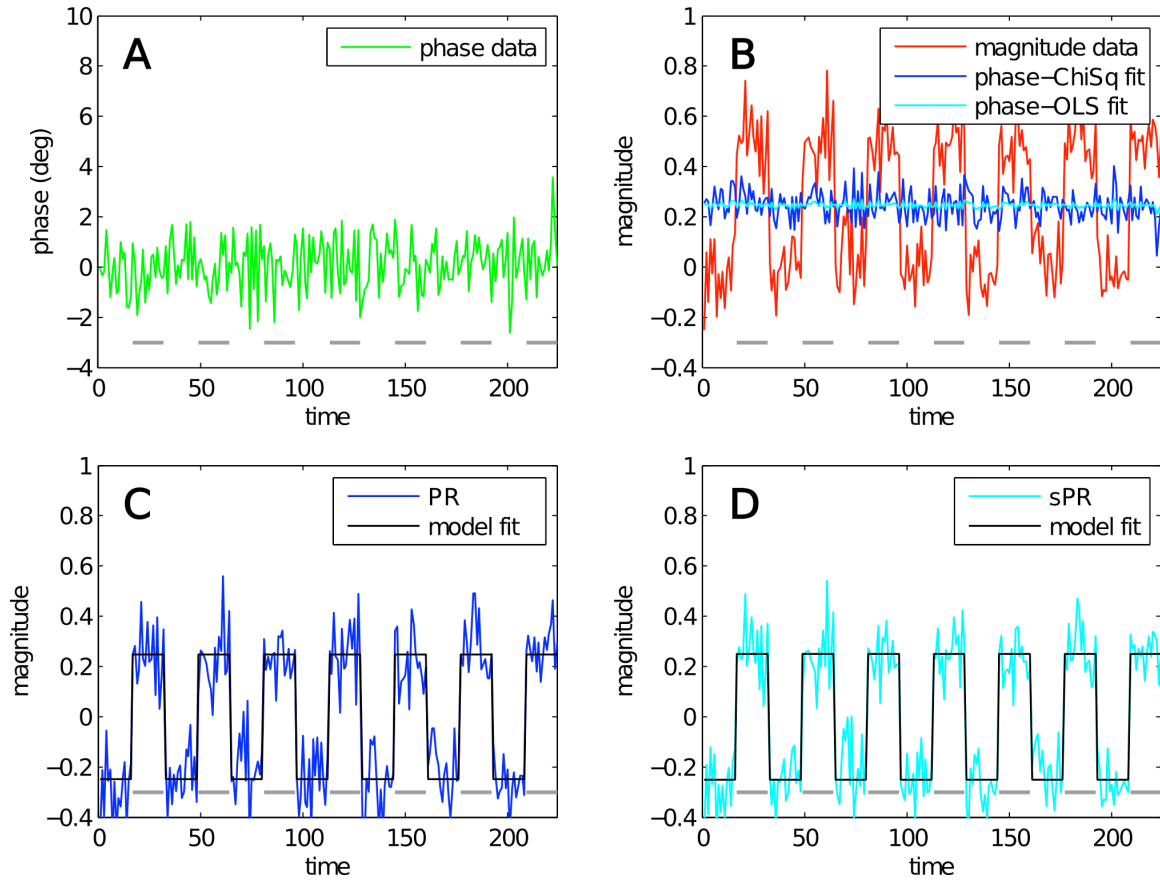


Figure 4.4. Simulated large vein suppression in a voxel with no large vein contribution. In this regime, phase fSNR is low but magnitude fSNR is high. A) Phase timecourse is plotted in green (t -value = -0.10). Gray dashes indicate stimulus-on periods. B) Magnitude timecourse is plotted in red (t -value = 5.21). Linear fits of phase to magnitude using L_{ChiSq} and L_{OLS} are plotted in blue and cyan, respectively. Using L_{ChiSq} yields larger absolute fits (e.g. larger b_1^* values). C) PR large vein suppressed timecourse is plotted in blue (t -value = 4.38). PR model fit timecourse is plotted in black. D) sPR large vein suppressed timecourse is plotted in cyan (t -value = 5.16). sPR model fit timecourse is plotted in black. In this regime, both PR and sPR show good preservation of magnitude BOLD activity. sPR exhibits slightly better preservation than PR.

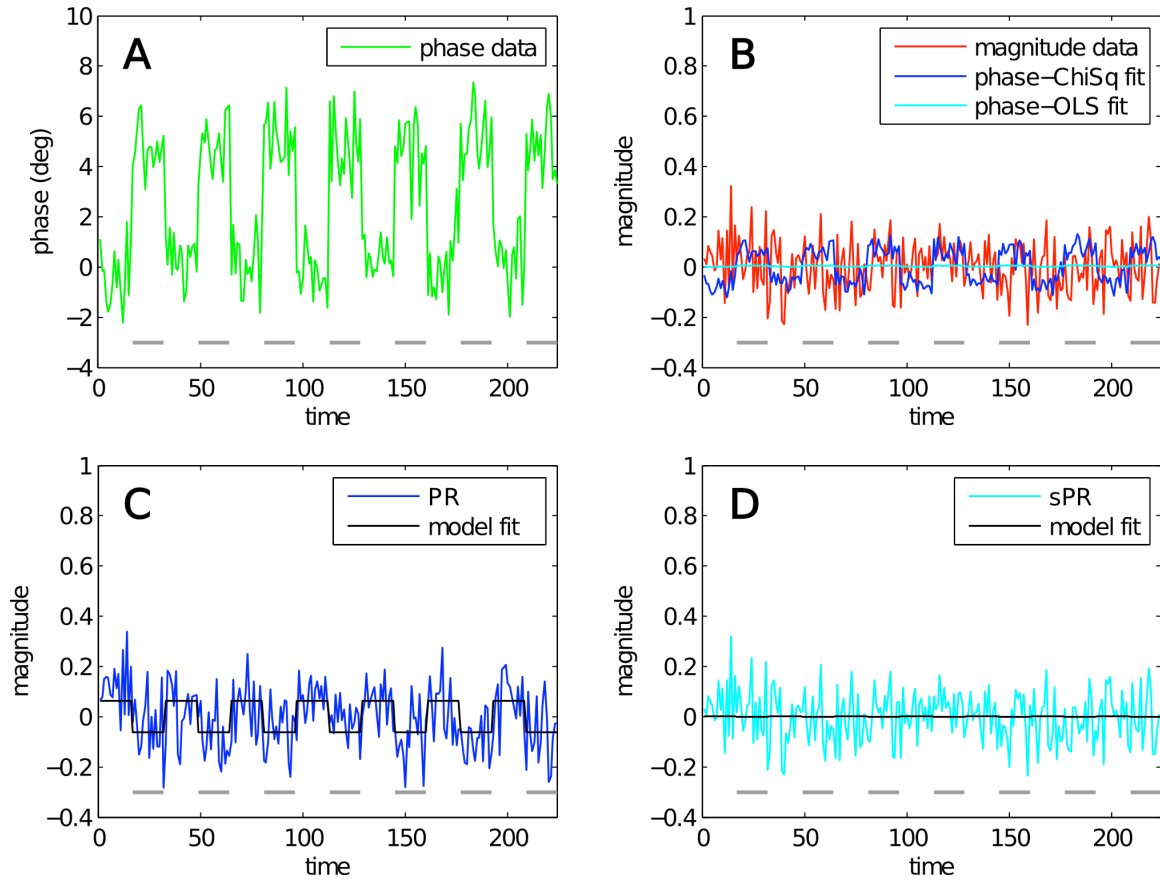


Figure 4.5. Simulated large vein suppression in a voxel adjacent to a large vein. In this regime, phase fSNR is high but magnitude fSNR is low. A) Phase timecourse is plotted in green (t -value = 4.55). Gray dashes indicate stimulus-on periods. B) Magnitude timecourse is plotted in red (t -value = 0.02). Linear fits of phase to magnitude using L_{ChiSq} and L_{OLS} are plotted in blue and cyan, respectively. Using L_{ChiSq} yields larger absolute fits (e.g. larger b_1^* values). C) PR large vein suppressed timecourse is plotted in blue (t -value = -1.22). PR model fit timecourse is plotted in black. D) sPR large vein suppressed timecourse is plotted in cyan (t -value = -0.02). sPR model fit timecourse is plotted in black. In this regime, PR overestimates b_1^* resulting in artifactual BOLD activity. sPR yields unbiased estimates of b_1^* and correctly estimates the large vein suppressed BOLD timecourse as the magnitude timecourse.

Fig 4.5 shows the simulation of large vein suppression in a voxel adjacent to a large vein. In this regime, phase fSNR is high while magnitude fSNR is low (t -value =

4.55, t -value = 0.02, respectively; Figs 4.5A,B). Using L_{ChiSq} in this regime clearly results in overestimation of b_1^* (blue, Fig 4.5B). Because in this simulation both magnitude and phase t -values are positive, the overestimation of b_1^* generates artifactual negative BOLD activity (blue, t -value = -1.22, Fig 4.5C). Using L_{OLS} does not result in overestimation of b_1^* (cyan, Fig 4.5B). Instead, sPR yields a large vein suppressed timecourse almost identical to the magnitude timecourse (cyan, t -value = -0.02, Fig 4.5D). In this regime, this is the desired effect because there is little task-related magnitude BOLD activity to suppress.

The results of applying PR and sPR on simulated complex-valued BOLD activity under a range of magnitude and phase fSNR conditions is shown in Fig 4.6. The expected fSNR for both magnitude and phase timecourses was varied from 0 to 10 in steps of 0.1. Averaging across repeated simulations was not done to preserve the random effect of noise under low magnitude fSNR conditions. Under the conditions when large veins contribute to BOLD activity (high phase, high magnitude fSNR conditions) both PR and sPR yield robust suppression of fSNR (Figs 4.6A,B). Under the conditions when large veins do not contribute to BOLD activity (low phase fSNR conditions) both PR and sPR methods preserve magnitude fSNR. However, under the conditions when a voxel is adjacent to a large vein (high phase, low magnitude fSNR conditions) PR overcorrects yielding artifactual positive or negative fSNR (Fig 4.6A). sPR does not exhibit this overcorrection (Fig 4.6B). These results demonstrate that sPR provides robust and unbiased suppression without introducing artifactual BOLD activity. Given these results, we use sPR to suppress large vein contributions to BOLD activity in our FFA/PPA

localization experiment.

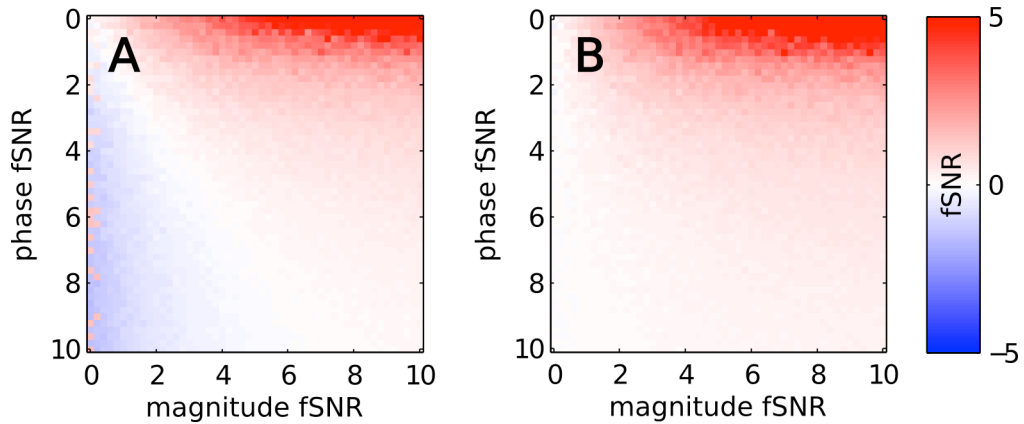


Figure 4.6. Simulated large vein suppression as a function of phase and magnitude fSNR plotted for A) PR and B) sPR. PR overcorrects for large vein contributions. This results in artifactual non-zero t -values at low magnitude fSNRs. sPR does not overcorrect for large vein contributions.

4.4 FFA/PPA localization study

Here we investigate the impact of large vein bias on the localization and measurement of semantic category areas. To do this, we compare standard magnitude measures of BOLD activity in FFA and PPA to those obtained using sPR large vein suppression. Through this study, we quantify the large vein contributions to individual ROIs and reveal the relationship between ROI size, fSNR and large vein contributions.

Methods

All MR data were collected with a whole-head volume radio frequency coil on the 4 Tesla Varian (Palo Alto, CA) INOVA scanner at UC Berkeley and reconstructed using Recon Tools written by the Berkeley Imaging Center. Procedures were approved by the

UC Berkeley Committee for the Protection for Human Subjects and performed on four subjects who gave written informed consent.

FFA/PPA Localization

FFA and PPA were localized using standard methods (Spiridon et al., 2006). The stimuli consisted of images from three categories: inanimate objects, human faces, and places. Each category contained 20 colored exemplars downloaded from the public Caltech 256 database (http://www.vision.caltech.edu/Image_Datasets/Caltech256/). Stimuli were presented at 500x500 pixels, extending across 20° of the visual field. A white fixation point was visible at all times.

Four subjects were scanned for two 384 second runs. The first run was set aside and used only to estimate the temporal correlation between magnitude and phase components. These temporal correlations were then applied to the responses of the second run for calculation of the sPR measure of BOLD activity and *t*-value contrasts. This prevented circularity in our sPR method. Each run consisted of six sets of four 16 second blocks. In a given set, each of the first three blocks consisted entirely of exemplars from one of the three categories shown 0.8 seconds apart. The fourth block was blank to compensate for hemodynamic delay. The order of categories in the first three blocks were pseudo-random such that each category was presented six times per run. While fixating, subjects performed a one-back attention task throughout the runs to ensure alertness. In the one-back task an image was randomly shown twice in a row, signaling the subject to press a button. To localize FFA and PPA in each subject, *t*-values

taking into account a six second hemodynamic delay were calculated for every voxel in the fMRI volume for the following contrasts: faces vs inanimate objects and places vs inanimate objects. FFA and PPA in both left and right hemispheres were defined for the large vein suppressed and magnitude measures of BOLD activity as the largest cluster of significant voxels (t -value > 3 , $p < 0.005$) in the ventral temporal cortex of each hemisphere.

The scanning protocol consisted of 36 coronal slices collected using standard gradient-echo EPI with voxel size $2.25 \times 2.25 \times 2.5 \text{ mm}^3$, FOV $144 \times 144 \text{ mm}^2$, flip angle 72° , TR 2s, and TE 28ms. Motion correction was performed using SPM 99 (<http://www.fil.ion.ucl.ac.uk/spm>), supplemented by additional custom Matlab (The Mathworks, Natick, MA) algorithms. Motion parameters were calculated from the magnitude volumes and then subsequently applied to both magnitude and phase volumes separately for reslicing. Prior to motion correction of the phase images, large scale phase wrapping due to field inhomogeneities was removed on a slice by slice basis using homodyne filtering (Noll et al., 1991; Reichenbach and Haacke, 2001). For each run and each individual voxel, drift in both magnitude and phase voxel timecourses was removed by fitting a third-degree polynomial. The timecourses were then z-scored (normalized to mean 0.0 and standard deviation 1.0).

Quantification of large vein contributions to ROIs

To quantify the amount of large vein contribution to individual ROIs, we computed the normalized size of each ROI after large vein suppression. Normalized ROI

size is defined as the ratio of ROI size with and without large vein suppression.

Mathematically normalized ROI size can be expressed as:

$$N_{norm} = N_{sPR} / N_{mag} ,$$

where N_{sPR} and N_{mag} are the number of voxels in a given ROI using sPR and the standard magnitude measure of BOLD activity, respectively. The percentage of voxels with large vein contributions can then be calculated as $(1 - N_{norm}) * 100\%$. The normalized ROI size, rather than the ROI size difference, was used to allow comparison of ROI size across subjects.

Correlation between ROI size, fSNR and large vein contributions

To correlate the amount of large vein contribution to the size and fSNR of individual ROIs, we computed two metrics quantifying the amount of large vein contribution to individual ROIs. The first metric was the ROI size difference (measured in number of voxels) with versus without sPR large vein suppression. Values close to zero indicate no large vein contribution. Larger negative values indicate more large vein contributions. The ROI size difference metric measures the number of voxels that are significant (t -value > 3 , $p < 0.005$) after large vein suppression. Thus it fails to capture suppression in voxels that remain significant (Fig 4.7). In order to capture the suppression in all voxels of an ROI, the second metric used was the difference between mean ROI t -values with versus without sPR large vein suppression. Values close to zero indicate no large vein contribution. Larger negative values indicate more large vein contributions. This metric is equally sensitive to suppression of both low and high magnitude t -values.

The correlations between these two metrics, ROI size and ROI fSNR without large vein suppression were calculated.

Quantification of hemisphere laterality

To quantify the hemisphere laterality of FFA and PPA we calculated an ROI size laterality index and an fSNR laterality index for each subject's FFA and PPA separately.

For a given subject and ROI, ROI size laterality is defined as:

$$N_{lat}^{ROI} = (N_r^{ROI} - N_l^{ROI}) / (N_r^{ROI} + N_l^{ROI}) ,$$

where N_r^{ROI} and N_l^{ROI} are the number of voxels in an ROI in the right and left

hemispheres, respectively. For a given subject and ROI, fSNR laterality is defined as:

$$t_{lat}^{ROI} = (\bar{t}_r^{ROI} - \bar{t}_l^{ROI}) / (\bar{t}_r^{ROI} + \bar{t}_l^{ROI}) ,$$

where \bar{t}_r^{ROI} and \bar{t}_l^{ROI} are the mean t -values of an ROI (as defined without large vein suppression) in the right and left hemispheres, respectively. For both indices, positive values indicate right hemisphere laterality and negative values indicate left hemisphere laterality. To determine if hemisphere laterality could be due to a lateral bias in vein size, these indices were calculated with and without sPR large vein suppression.

Venograms

Susceptibility weighted venograms were collected and preprocessed using standard methods (Reichenbach and Haacke, 2001). Venograms were collected for ground truth on the location of veins and to insure that our large vein suppression method was indeed targeting large veins. The 2D gradient-echo venogram scan parameters were:

voxel size $1.0 \times 1.0 \times 1.0 \text{ mm}^3$, FOV $192 \times 192 \text{ mm}^2$, flip angle 75° , TR 4.21s, TE 26ms. The slice prescription covered 96 coronal slices of the most posterior portion of the brain matching the spatial coverage of our fMRI data. Homodyne filtering was done on a slice by slice basis in Matlab to remove large scale phase wrapping due to field inhomogeneities. Minimum intensity projection was performed in the axial plane on a sliding slab of three slices to match the spatial resolution of the fMRI experiment. Finally, the venograms were manually coregistered to the first functional volume of the fMRI experiment of each subject using custom software.

4.5 Results

sPR reveals large vein contributions to ROIs

Representative t -value contrasts for the localization of PPA is shown in Fig 4.8. The magnitude t -values of the right PPA overlap entirely with a large vein (Fig 4.8A). This large vein as well as others are shown as the low intensity voxels in the venogram of Fig 4.8D (Reichenbach and Haacke, 2001). The phase t -values in this subject are weak in voxels containing the large vein but strong in voxels adjacent to the vein (Fig 4.8B). Given this, it is not surprising that using sPR with only a one-voxel-neighborhood yields poor large vein suppression in right PPA (Fig 4.8C). With the full seven-voxel-neighborhood, sPR is able to utilize the high phase fSNR voxels around the large vein and correctly suppress the t -values in right PPA (Fig 4.8E). This result suggests that consideration of the magnitude and phase fSNR distribution around veins is crucial for the suppression of large vein BOLD activity. For this subject, left PPA appears to lie on a

small vein. Because the vein is small relative to the size of the voxels scanned, sPR only weakly suppresses the t -values in the left PPA of this subject.

Fig 4.9 shows the size of each ROI with relative to without large vein suppression. This normalized measure of ROI size allows us to determine how much smaller specific ROIs are without large vein contributions on average across subjects. sPR large vein suppression significantly reduces the ROI sizes of right PPA, left PPA and right FFA ($p < 0.05$). Specifically, it is estimated that $38 \pm 7\%$ of right PPA, $14 \pm 4\%$ of left PPA, $16 \pm 7\%$ of right FFA, and $6 \pm 8\%$ of left FFA voxels reflect signal predominantly from large draining veins. Notably, large vein contributions to the size of right PPA is significantly greater than the contributions to other ROIs ($p < 0.05$). Left FFA does not have significant large vein contributions. F -tests of these data reveals that the amount of large vein contribution varies significantly across ROIs ($p < 0.05$). These results suggest that the distribution of vein sizes is biased toward specific regions of interest (ROIs).

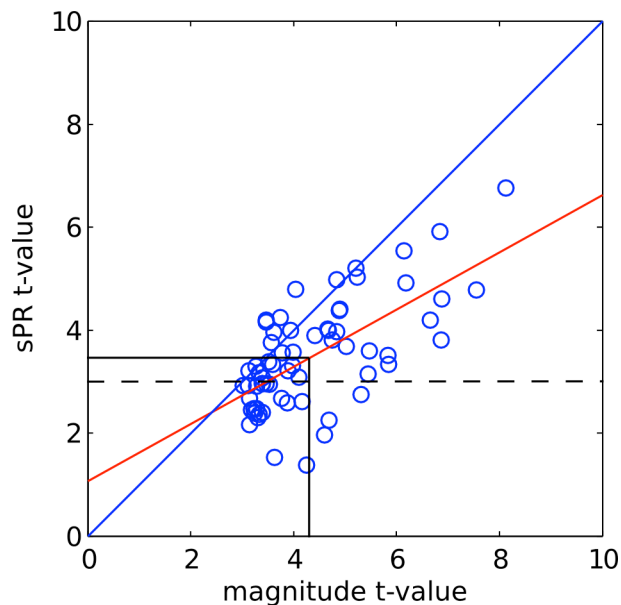


Figure 4.7. sPR t -values plotted against magnitude t -values for right PPA voxels of one typical subject. The linear fit is shown in red. Black lines indicate mean ROI t -values measured using sPR and standard magnitude BOLD fMRI. The dashed line shows the significance level (t -value > 3 , $p < 0.005$). Many high magnitude t -valued voxels are reduced by large vein suppression but remain significant.

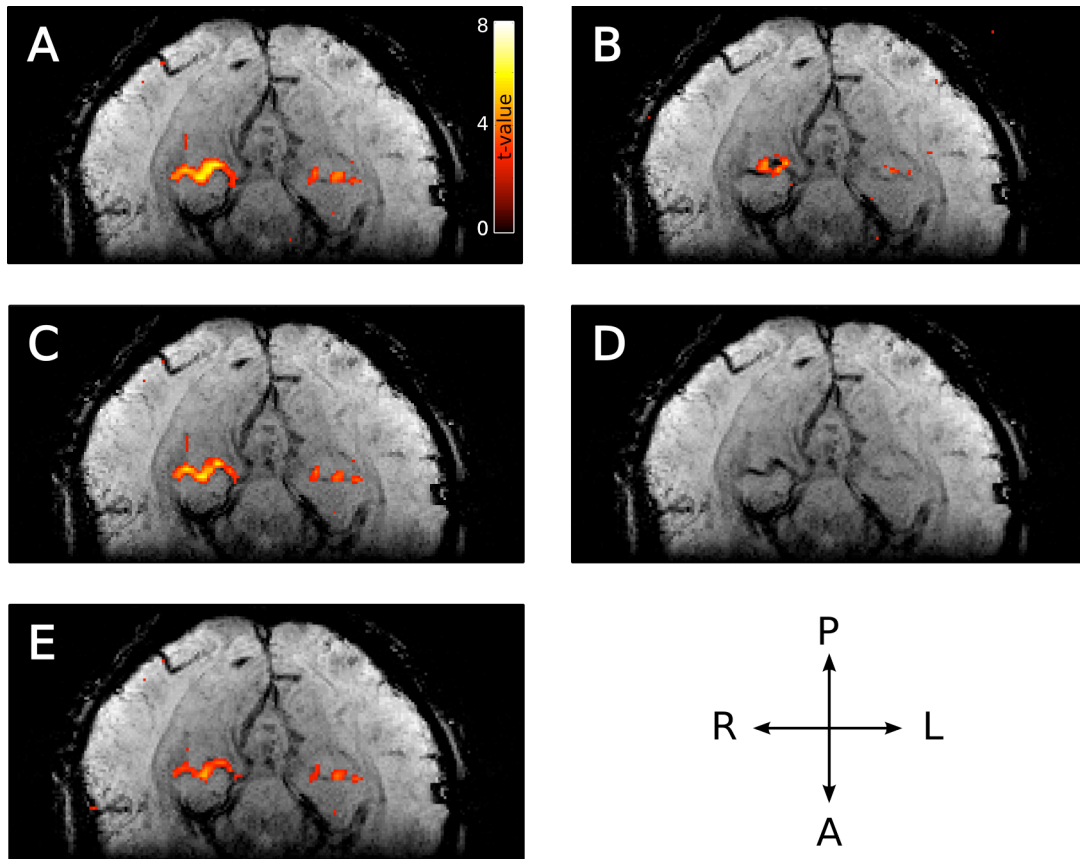


Figure 4.8. Typical PPA t -values with and without large vein suppression overlaid on the corresponding venogram. A) Magnitude t -values. The majority of right PPA coincides with a large vein. B) Phase t -values (absolute value). The majority of high phase t -valued voxels lie adjacent to the vein. C) Large vein suppressed t -values using sPR with a one-voxel-neighborhood. In this case, sPR fails to suppress the large vein contributions to right PPA because most of the high phase t -values lie adjacent to the vein. D) Corresponding venogram slice. E) Large vein suppressed t -values using sPR with the full seven-voxel-neighborhood. In this case, sPR utilizes the phase component of the BOLD activity from neighboring voxels to correctly suppress the large vein contributions to right PPA. The vein contributing to left PPA is too small to be suppressed using sPR.

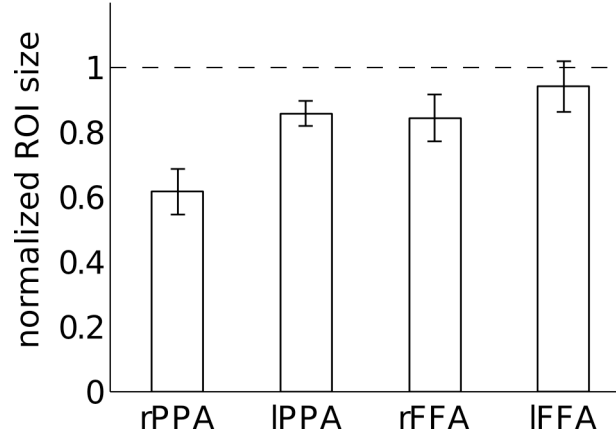


Figure 4.9. Quantification of large vein contributions to specific ROIs. Normalized ROI size is calculated for each ROI as the ratio of ROI size with and without sPR large vein suppression. sPR significantly reduces ROI size for right PPA, left PPA and right FFA ($p < 0.05$). Specifically, $38 \pm 7\%$ of right PPA, $14 \pm 4\%$ of left PPA, $16 \pm 7\%$ of right FFA, and $6 \pm 8\%$ of left FFA voxels predominantly reflect signal from large draining veins. Error bars are SEM across subjects.

Large vein contributions as a function of ROI size and fSNR

To determine if prior studies on semantic representation were biased toward large veins, we calculated the correlation between large vein contributions, ROI size and ROI fSNR. Each ROI of each subject was treated as a separate data point. Fig 4.10A shows the correlation between ROI size and the difference in ROI size with versus without large vein suppression ($r = -0.48$, $p < 0.05$). Fig 4.10B shows the correlation between mean ROI t -value and the difference in mean ROI t -value with versus without large vein suppression ($r = -0.59$, $p < 0.01$). These results suggest that across cortical regions and subjects, ROIs larger in size and higher in fSNR tend to have larger contributions from large veins.

Large vein contributions to hemisphere laterality

To determine if the laterality of semantic representation simply reflects larger veins in the right hemisphere we computed laterality indices of FFA and PPA with and without large vein suppression (Fig 4.11). Positive laterality values indicate right hemisphere lateralization. Negative values indicate left hemisphere lateralization. Consistent with previous studies, without large vein suppression we find that both PPA and FFA are right hemisphere lateralized in both size ($N_{lat}^{PPA} = 0.09 \pm 0.11$, $N_{lat}^{FFA} = 0.34 \pm 0.03$, Fig 4.11A) and fSNR ($t_{lat}^{PPA} = 0.03 \pm 0.02$, $t_{lat}^{FFA} = 0.02 \pm 0.02$, Fig 4.11B). However, with large vein suppression we find that PPA is not right but left hemisphere lateralized in size ($N_{lat}^{PPA} = -0.15 \pm 0.14$) and fSNR ($t_{lat}^{PPA} = -0.02 \pm 0.02$). These differences in ROI size and fSNR lateralization with versus without large vein suppression are significant ($p < 0.02$ and $p < 0.05$, respectively). With large vein suppression, we find that FFA is still right hemisphere lateralized in size ($N_{lat}^{FFA} = 0.26 \pm 0.05$) and fSNR ($t_{lat}^{FFA} = 0.01 \pm 0.03$) although less so than without suppression ($p = 0.08$ and $p = 0.18$, respectively). These results suggest that the degree of right hemisphere laterality of semantic category representation in the human brain is biased by larger contributions from large veins in the right hemisphere. This is consistent with the tendency for veins to be larger in the right hemisphere (Di Chiro, 1972; Durgun et al., 1993; Ayanzen et al., 2000; Stoquart-ElSankari et al., 2009).

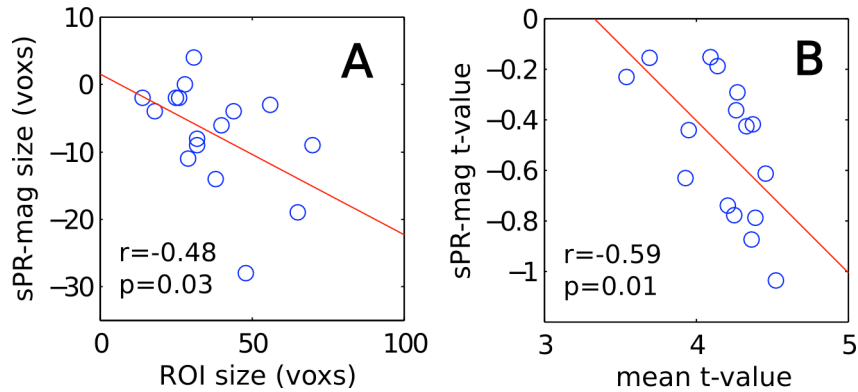


Figure 4.10. Correlation between ROI size, mean t -value and large vein contribution across ROIs of all subjects. Each data point represents a single ROI from a single subject. A) Difference in ROI size with versus without sPR large vein suppression plotted against ROI size ($r = -0.48$, $p < 0.05$). B) Difference in mean ROI t -value with versus without sPR large vein suppression plotted against mean ROI t -value ($r = -0.59$, $p < 0.01$). These results suggest that ROIs larger in size and higher in fSNR tend to have larger contributions from large veins.

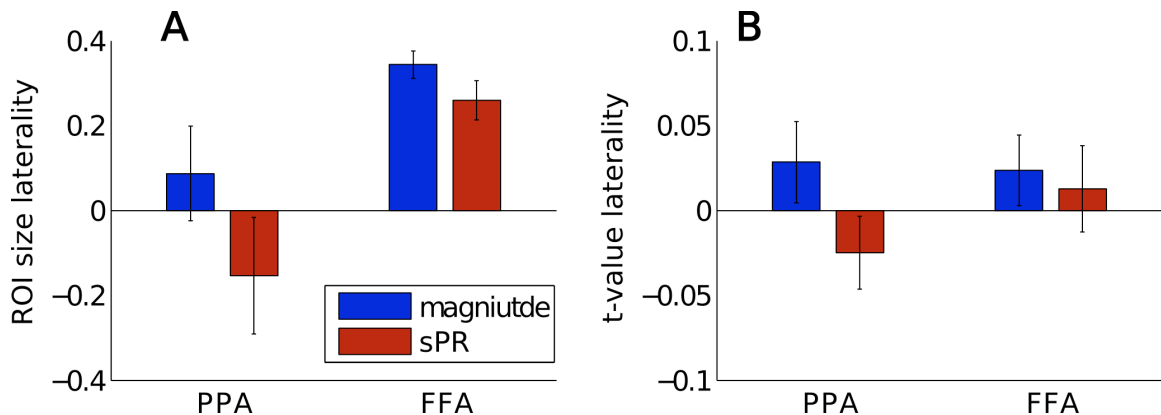


Figure 4.11. Hemisphere laterality with and without large vein suppression. Positive values indicate right hemisphere lateralization. Negative values indicate left hemisphere lateralization. A) Size laterality measured as the ratio of hemispheric difference to hemispheric sum of ROI size. Large vein suppression significantly reduces right hemisphere size laterality in PPA ($p < 0.02$, paired t -test) but not significantly in FFA ($p = 0.08$). B) fSNR laterality measured as the ratio of hemispheric difference to hemispheric sum of mean ROI t -value. Large vein suppression significantly reduces right hemisphere fSNR laterality in PPA ($p < 0.05$) but not significantly in FFA ($p = 0.18$). Error bars are SEM across subjects.

4.6 Discussion

The results of our study challenge the assumption that gradient-echo BOLD fMRI can be used to infer neural differences across cortical regions and across subjects.

Previous studies used this assumption to suggest that semantic representation is right hemisphere lateralized and that semantic category areas are rare (for review see Reddy and Kanwisher, 2006). Given the large vein bias demonstrated in this study, these well known properties of semantic category representation must be reevaluated.

Our results on the relationship between ROI size, fSNR and large vein contributions provide important insight into the lateralization of semantic category representation (Kanwisher et al., 1997; Epstein and Kanwisher, 1998; Downing et al., 2006; Spiridon et al., 2006). Our finding that right PPA has more large vein contributions than left PPA (Fig 4.9) suggests that the degree of right hemisphere laterality of PPA reported in prior studies was biased by hemispheric differences in vein size. Calculation of PPA laterality indices with large vein suppression reveals that PPA may actually be left hemisphere lateralized (Fig 4.11). We also find that FFA is less right hemisphere lateralized after large vein suppression. Together, these results suggest gradient-echo BOLD fMRI should not be used to infer laterality of semantic representation without accounting for hemispheric differences in vein size (Di Chiro, 1972; Durgun et al., 1993; Ayanzen et al., 2000; Stoquart-ElSankari et al., 2009).

Furthermore, our results provide important insight into the rarity of semantic category areas (Downing et al., 2006; Spiridon et al., 2006). As mentioned previously,

studies of FFA often report subjects with no detectable left FFA. Our finding that left FFA has no significant large vein contribution suggests that semantic category areas difficult to detect, such as left FFA, may not reflect absence of neural representation. Instead, difficulty or inability to detect certain ROIs using gradient-echo BOLD fMRI may reflect a vascular bias away from those ROIs. This would not be surprising given recent physiological evidence for the existence of left FFA. One study reported that over 90% of visually responsive neurons responded selectively to faces in a face selective region in the left hemisphere of a macaque monkey (Tsao et al., 2006). That study also reported that face-selective neurons were equally numerous and equally face-selective in both hemispheres. Another study (Tsao et al., 2008) showed strong bilateral face-selective activity in 9 of 10 macaque monkeys using contrast-enhanced fMRI. Importantly, this fMRI method does not depend on the gradient-echo BOLD contrast which is biased toward large veins. Instead, it uses monocrySTALLINE iron oxide nanoparticles (MION) to enhance cerebral blood volume functional contrast which is more specific to the microvasculature (Mandeville and Marota, 1999; Vanduffel et al., 2001). These results suggest that the rarity of semantic category areas reported in previous studies may simply reflect large vein bias toward specific ROIs.

The results of this study emphasizes the fact that BOLD fMRI measures neural activity only indirectly, through the cortical vasculature. Current understanding of cortical vasculature organization with respect to underlying neurons is poor and there have been few experimental studies on this subject (Gardner, 2010; Harel et al., 2010). Some studies have shown that functional grouping of microvasculature is correlated with functional

grouping of neurons in the rat barrel cortex (Woolsey et al., 1996; Berwick et al., 2008). The relationship between the functional organization of microvasculature and neurons has been further tightened by studies demonstrating the plasticity of cortical capillary density across several weeks (Pichiule and LaManna, 2002; LaManna et al., 2004). Other studies proposed that venous functional organization exists on a larger scale across cortical columns (Gardner, 2010; Shmuel et al., 2010; Kriegeskorte et al., 2010; Op de Beeck et al., 2010). These studies suggest that larger venules and veins receive drainage from similarly tuned neurons across several cortical columns. This would allow low resolution BOLD fMRI to resolve stimulus information represented at the sub-voxel scale (e.g. stimulus orientation).

The results of this study suggest that functional organization between venous vasculature and neurons (referred to as venous functional organization) may exist, and that it may vary considerably at the scale of cortical areas. Previous studies have reported greater vascularization in primary visual cortex (V1) than in area V2 (Duvernoy et al., 1981; Zheng et al., 1991; Logothetis and Wandell, 2004). However, to our knowledge this is the first study that demonstrates vascular differences across semantic category areas.

By using methods that take into account or remove the contributions from large veins the problems of large vein bias are avoided. Such methods may reveal new semantic category areas and allow for more complete functional characterization of visual cortex. Fortunately, advances in fMRI methodology including the sPR method presented here can provide robust and efficient suppression of BOLD activity from large veins (Yacoub et al 2001, Duong et al 2003, Vanzetta et al 2004, Hulvershorn 2004). We

expect that future studies using these methods at higher field and higher spatial resolution will be important for improving our understanding of semantic category representation in the human brain.

Conclusions

In this chapter, we presented sPR as a novel, robust and unbiased method for suppressing large vein contributions to BOLD activity. By measuring ROI size and fSNR with and without large vein suppression we quantified the amount of large vein contribution to semantic category areas FFA and PPA. We showed that larger ROIs higher in fSNR tend to have more large vein contributions. These results support our hypothesis that the apparent paucity and laterality of semantic category areas reflect bias in the distribution of vein size toward specific ROIs. We are reminded that it is important to account for the cortical vasculature when interpreting results of studies using gradient-echo BOLD fMRI.

Appendices

A.1 Susceptibility Weighted Venography Theory

For a vein modeled as a cylinder filled with venous blood whose radius is much shorter than its length, intra and extra-vascular susceptibility magnetic field shifts, ΔB_{intra} and ΔB_{extra} , can be written as (Ogawa et al., 1993):

$$\Delta B_{intra} = 2 \cdot \pi \cdot \chi_{do} \cdot (1 - Y) \cdot Hct \cdot B_o \cdot \left(\cos^2 \psi - \frac{1}{3} \right) \quad [A.1.1]$$

$$\Delta B_{extra} = 2 \cdot \pi \cdot \chi_{do} \cdot (1 - Y) \cdot Hct \cdot B_o \cdot \sin^2 \psi \cdot \left(\frac{a}{r} \right)^2 \cdot \cos 2\rho \quad [A.1.2]$$

where $\chi_{do} = 0.18 \cdot 10^{-6}$ is the susceptibility difference between deoxygenated and oxygenated blood (Ogawa and Lee, 1990; Weisskoff and Kiihne, 1992), B_o is the applied field strength, ψ is the angle between the vein and B_o , Y is the fractional oxygen saturation of the blood, Hct is the fractional volume of red blood cells, a is the radius of the vein, r is the distance away from the center of the vein in the vessel cross section and ρ is the angle away from B_o in the vessel cross section.

In the presence of a magnetic field B , protons will precess at the Larmor frequency $\omega = B \cdot \gamma$, where γ is the gyromagnetic ratio (for protons $\gamma = 42.58 \cdot 2 \cdot \pi$ Mrads/Tesla). [Fig A.1.1A](#) shows the expected frequency shifts relative to the frequency of gray matter in the transverse plane of a vein with $Hct = 0.4$, $Y = 0.56$, $B_o = 4$ Tesla and $a = 0.5$ mm. Given that phase is the time integral of frequency, phase shifts due to static magnetic field shifts can be written as:

$$\Delta phase(TE) =$$

$$-\int_0^{TE} \Delta \omega \cdot dt = -\int_0^{TE} \Delta B \cdot \gamma \cdot dt = -\Delta B \cdot \gamma \cdot TE \quad [\text{A.1.3}]$$

where TE is the time from the RF pulse to the collection of the center of k -space. [Fig A.1.1B](#) shows the expected phase distribution given the TE that allows $-\pi$ radians of intravascular phase accrual for veins parallel to B_0 (the standard TE for SWV; Reichenbach and Haacke, 2001; Brainovich et al., 2008).

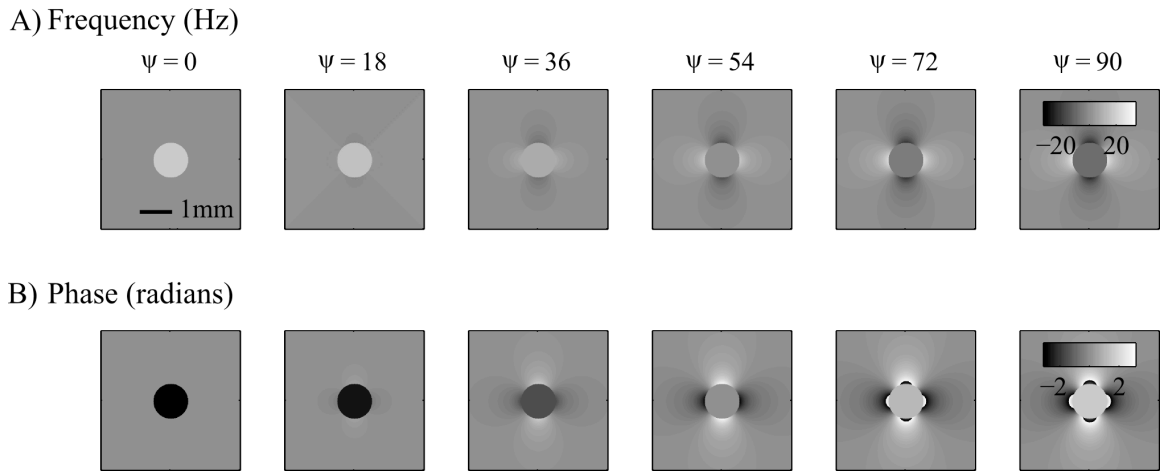


Figure A.1.1 Frequency and phase spatial distributions in and around veins of various orientations relative to B_0 . A) The expected frequency shifts relative to the frequency of gray matter in the transverse plane of a vein. Frequency was calculated as $f = \omega / (2\pi) = B \cdot \gamma / (2\pi)$, given Hct = 0.4, Y = 0.56, $B_0 = 4$ Tesla, $\chi_{do} = 0.18 \times 10^{-6}$, and $a = 0.5$ mm. B) The expected phase distribution given a TE that allows $-\pi$ radians of intravascular phase accrual for veins parallel to B_0 .

Due to the symmetry of the extravascular phase distribution, for veins much smaller than a voxel, extravascular phase shifts sum to zero. Therefore, in SWV it is standard to consider only intravascular phase for weighting magnitude intensities (Reichenbach et al., 2000). From [Eq \[A.1.2\]](#) and [Fig A.1.1B](#), we expect maximally negative intravascular phase accrual from veins parallel to B_0 and maximally positive

intravascular phase accrual from veins perpendicular to B_0 . In the case when TE is set for $-\pi$ intravascular phase accrual for veins parallel to B_0 ($TE_{-\pi} = 28\text{ms}$ for $B_0 = 3$ Tesla), we expect a maximally positive intravascular phase accrual of $\pi/2$ in veins perpendicular to B_0 . Adding the assumption that the orientation distribution of veins relative to B_0 is isotropic (i.e. a flat probability distribution for ψ), Fig 2.2A shows the expected probability distribution of intravascular phase throughout the brain for $TE = TE_{-\pi}$.

A.2 T2* Magnitude Contrast Optimization – TE_{opt}

Given that transverse magnetization decay can be modeled as exponential, optimizing for contrast between two tissue types with equal initial magnetization but different decay constants $T2^*_a$ and $T2^*_b$ requires solving the differential equation:

$\frac{d}{dt}[M_{xy}(0) \cdot e^{-t/T2^*_a} - M_{xy}(0) \cdot e^{-t/T2^*_b}] = 0$. The solution to this equation is:

$$t = TE_{opt} = \ln\left(\frac{T2^*_b}{T2^*_a}\right) \cdot \left(\frac{1}{T2^*_a} - \frac{1}{T2^*_b}\right)^{-1} \quad [\text{A.2.1}]$$

Note this solution is only subtly different from the rule of thumb: $TE_{opt} = T2^*_a$ or $T2^*_b$ because the signal difference peak with respect to TE is very broad in the range of $T2^*_a$ and $T2^*_b$ (Fig 2.1). Given the $T2^*$ values of gray matter and venous blood (Table 2.1), TE values for $-\pi$ intravascular phase accrual ($TE_{-\pi}$) at all clinical field strengths are less than their corresponding values required for optimal vein-gray matter magnitude contrast (TE_{opt}). Magnitude contrasts of $TE_{-\pi}$ venograms are predicted to be ~5% less than those of TE_{opt} venograms at all standard field strength above 1.5T.

A.3 Optimal weighting of magnitude and phase

In this study, we are interested in combining the magnitude and phase components of complex-valued fMRI to yield a single timecourse with optimal fSNR at the voxel level. Assuming functional changes in magnitude and phase both come from the same source (a large vein), we can model the z-scored magnitude and phase responses to a single stimulus as:

$$S^m = \mu + \epsilon_m \quad [\text{A.3.1}]$$

and

$$S^p = r\mu + \epsilon_p \quad [\text{A.3.2}]$$

where

$$\begin{aligned} \epsilon_m \perp \epsilon_p, \quad \epsilon_m \sim N(0, \sigma_m^2), \quad \epsilon_p \sim N(0, \sigma_p^2), \\ r = \text{sign}(\text{corr}(S^m, S^p)) \end{aligned} \quad [\text{A.3.3}]$$

and

$$\sigma_p^2 = b\sigma_m^2 \quad [\text{A.3.4}]$$

The magnitude and phase fSNR can then be expressed respectively as:

$$fSNR^m = \frac{\mu^2}{\sigma_m^2} \quad [\text{A.3.5}]$$

and

$$fSNR^p = \frac{\mu^2}{\sigma_p^2}. \quad [\text{A.3.6}]$$

Because task-related phase changes are on the order of 0.1 radians (Menon, 2002; Lee et al., 2007) we can linearly combine magnitude and phase. We define the optimal weighted

combination of magnitude and phase as:

$$S^{opt} = S^m + r a^* S^p \quad [\text{A.3.7}]$$

where

$$a^* = \arg \max_a \{ fSNR^{opt} \} \quad [\text{A.3.8}]$$

and

$$fSNR^{opt} = \frac{(\mu + a\mu)^2}{\sigma_m^2 + \sigma_p^2} = \frac{(1+a)^2}{1+ba^2} fSNR^m . \quad [\text{A.3.9}]$$

To solve for a^* , we first take the derivative of Eq [A.3.9] with respect to a :

$$\frac{\partial fSNR^{opt}}{\partial a} = \frac{2(1-ba)(1+a)}{(1+ba^2)^2} fSNR^m . \quad [\text{A.3.10}]$$

We then set this equation equal to zero and solve for a to find that:

$$a^* = b^{-1} . \quad [\text{A.3.11}]$$

By plugging Eq [A.3.11] into Eq [A.3.7], we find that:

$$fSNR^{opt} = (1+b^{-1}) fSNR^m \quad [\text{A.3.12}]$$

which is greater than the magnitude fSNR for all values of b since b cannot be negative.

Note that when σ_p^2 equals σ_m^2 ($b = 1$), combining magnitude and phase using Eq [A.3.7] yields an $fSNR^{opt}$ twice as large as $fSNR^m$. This increase in fSNR would be equivalent to doubling the amount of data collected in the magnitude method of measuring BOLD activity.

Note, from Eq [A.3.4], b is simply the ratio of noise variances: σ_p^2 over σ_m^2 .

However, b can also be equivalently expressed as the ratio of fSNRs: $fSNR^p$ over $fSNR^m$ or F^p over F^m as in Eq [3.1] of the main text.

References

- Ayanzen, R. H., Bird, C. R., Keller, P. J., McCully, F. J., Theobald, M. R. and Heiserman, J. E., 2000. Cerebral MR venography: Normal anatomy and potential diagnostic pitfalls. *American Journal of Neuroradiology*. 21, 74-78.
- Bandettini, P. A., Jesmanowicz, A., Wong, E. C. and Hyde, J. S., 1993. Processing strategies for time-course data sets in functional MRI of the human brain. *Magn Reson Med*. 30, 161-173.
- Bandettini, P. A. and Wong, E. C., 1995. Effects of Biophysical and Physiological-Parameters on Brain Activation-Induced $R(2)^*$ and $R(2)$ Changes - Simulations Using a Deterministic Diffusion-Model. *International Journal of Imaging Systems and Technology*. 6, 133-152.
- Bandettini, P. A., Wong, E. C., Jesmanowicz, A., Hinks, R. S. and Hyde, J. S., 1994. Spin-echo and gradient-echo EPI of human brain activation using BOLD contrast: a comparative study at 1.5 T. *NMR Biomed*. 7, 12-20.
- Berwick, J., Johnston, D., Jones, M., Martindale, J., Martin, C., Kennerley, A. J., Redgrave, P. and Mayhew, J. E. W., 2008. Fine detail of neurovascular coupling revealed by spatiotemporal analysis of the hemodynamic response to single whisker stimulation in rat barrel cortex. *Journal of Neurophysiology*. 99, 787-798.
- Boxerman, J. L., Bandettini, P. A., Kwong, K. K., Baker, J. R., Davis, T. L., Rosen, B. R. and Weisskoff, R. M., 1995. The intravascular contribution to fMRI signal change: Monte Carlo modeling and diffusion-weighted studies in vivo. *Magn Reson Med*. 34, 4-10.
- Brainovich, V., Sabatini, U. and Hagberg, G. E., 2008. Advantages of using multiple-echo image combination and asymmetric triangular phase masking in magnetic resonance venography at 3 T. *Magn Reson Imaging*. 27, 23-37.
- Cox, R. W., Jesmanowicz, A. and Hyde, J. S., 1995. Real-Time Functional Magnetic-Resonance-Imaging. *Magnetic Resonance in Medicine*. 33, 230-236.
- Dale, A. M., 1999. Optimal experimental design for event-related fMRI. *Hum Brain Mapp*. 8, 109-114.
- Di Chiro, G., 1972. Venous patterns of cerebral dominance. *N Engl J Med*. 287, 933-934.
- Dougherty, E. R. and Brun, M., 2006. On the Number of Close-to-Optimal Feature Sets. *Cancer Inform*. 2, 189-196.
- Downing, P. E., Chan, A. W., Peelen, M. V., Dodds, C. M. and Kanwisher, N., 2006. Domain specificity in visual cortex. *Cereb Cortex*. 16, 1453-1461.
- Downing, P. E., Jiang, Y. H., Shuman, M. and Kanwisher, N., 2001. A cortical area selective for visual processing of the human body. *Science*. 293, 2470-2473.
- Duong, T. Q., Yacoub, E., Adriany, G., Hu, X., Ugurbil, K. and Kim, S. G., 2003. Microvascular BOLD contribution at 4 and 7 T in the human brain: gradient-echo and spin-echo fMRI with suppression of blood effects. *Magn Reson Med*. 49, 1019-1027.
- Durgun, B., Ilgit, E. T., Cizmeli, M. O. and Atasever, A., 1993. Evaluation by Angiography of the Lateral Dominance of the Drainage of the Dural Venous Sinuses. *Surgical and Radiologic Anatomy*. 15, 125-130.

- Duvernoy, H. M., 1999. [Vascularization of the cerebral cortex]. *Rev Neurol (Paris)*. 155, 684-687.
- Duvernoy, H. M., Delon, S. and Vannson, J. L., 1981. Cortical blood vessels of the human brain. *Brain Res Bull*. 7, 519-579.
- Epstein, R. and Kanwisher, N., 1998. A cortical representation of the local visual environment. *Nature*. 392, 598-601.
- Ewbank, M. P., Schluppeck, D. and Andrews, T. J., 2005. fMR-adaptation reveals a distributed representation of inanimate objects and places in human visual cortex. *Neuroimage*. 28, 268-279.
- Fox, P. T. and Raichle, M. E., 1986. Focal Physiological Uncoupling of Cerebral Blood-Flow and Oxidative-Metabolism during Somatosensory Stimulation in Human-Subjects. *Proceedings of the National Academy of Sciences of the United States of America*. 83, 1140-1144.
- Gao, J. H., Miller, I., Lai, S., Xiong, T. J. and Fox, P. T., 1996. Quantitative assessment of blood inflow effects in functional MRI signals. *Magnetic Resonance in Medicine*. 36, 314-319.
- Gardner, J. L., 2010. Is cortical vasculature functionally organized? *Neuroimage*. 49, 1953-1956.
- Geissler, A., Lanzenberger, R., Barth, M., Tahamtan, A. R., Milakara, D., Gartus, A. and Beisteiner, R., 2005. Influence of fMRI smoothing procedures on replicability of fine scale motor localization. *Neuroimage*. 24, 323-331.
- Geyer, S., Schormann, T., Mohlberg, H. and Zilles, K., 1999. Areas 3a, 3b, and 1 of human primary somatosensory cortex. Part 2. Spatial normalization to standard anatomical space. *Neuroimage*. 11, 684-696.
- Glantz, S. A., 2005. *Primer of biostatistics*. McGraw-Hill.
- Haacke, E. M., Hopkins, A., Lai, S., Buckley, P., Friedman, L., Meltzer, H., Hedera, P., Friedland, R., Klein, S., Thompson, L. and et al., 1994. 2D and 3D high resolution gradient echo functional imaging of the brain: venous contributions to signal in motor cortex studies. *NMR Biomed*. 7, 54-62.
- Haacke, E. M., Lai, S., Yablonskiy, D. A. and Lin, W. L., 1995. In-Vivo Validation of the Bold Mechanism - a Review of Signal Changes in Gradient-Echo Functional Mri in the Presence of Flow. *International Journal of Imaging Systems and Technology*. 6, 153-163.
- Hajnal, J. V., Myers, R., Oatridge, A., Schwieso, J. E., Young, I. R. and Bydder, G. M., 1994. Artifacts due to stimulus correlated motion in functional imaging of the brain. *Magn Reson Med*. 31, 283-291.
- Hammond, K. E., Lupo, J. M., Xu, D., Metcalf, M., Kelley, D. A., Pelletier, D., Chang, S. M., Mukherjee, P., Vigneron, D. B. and Nelson, S. J., 2008. Development of a robust method for generating 7.0 T multichannel phase images of the brain with application to normal volunteers and patients with neurological diseases. *Neuroimage*. 39, 1682-1692.
- Harel, N., Bolan, P. J., Turner, R., Ugurbil, K. and Yacoub, E., 2010. Recent Advances in High-Resolution MR Application and Its Implications for Neurovascular Coupling Research. *Front Neuroenergetics*. 2, 130.

- Haxby, J. V., Gobbini, M. I., Furey, M. L., Ishai, A. and Pietrini, P., 2001. Distinct, overlapping representations of faces and multiple categories of objects in ventral temporal cortex. *Neuroimage*. 13, S891-S891.
- Hu, X. P. and Le, T. H., 1996. Artifact reduction in EPI with phase-encoded reference scan. *Magnetic Resonance in Medicine*. 36, 166-171.
- Hulvershorn, J., Bloy, L., Gualtieri, E. E., Leigh, J. S. and Elliott, M. A., 2005. Spatial sensitivity and temporal response of spin echo and gradient echo bold contrast at 3 T using peak hemodynamic activation time. *Neuroimage*. 24, 216-223.
- Jenkinson, M., 2003. Fast, automated, N-dimensional phase-unwrapping algorithm. *Magn Reson Med*. 49, 193-197.
- Jezzard, P. and Balaban, R. S., 1995. Correction for Geometric Distortion in Echo-Planar Images from B-0 Field Variations. *Magnetic Resonance in Medicine*. 34, 65-73.
- Jezzard, P., Duewell, S. and Balaban, R. S., 1996. MR relaxation times in human brain: Measurement at 4 T. *Radiology*. 199, 773-779.
- Jochimsen, T. H., Norris, D. G., Mildner, T. and Moller, H. E., 2004. Quantifying the intra- and extravascular contributions to spin-echo fMRI at 3 T. *Magn Reson Med*. 52, 724-732.
- Kanwisher, N., McDermott, J. and Chun, M. M., 1997. The fusiform face area: A module in human extrastriate cortex specialized for face perception. *Journal of Neuroscience*. 17, 4302-4311.
- Kay, K. N., Naselaris, T., Prenger, R. J. and Gallant, J. L., 2008. Identifying natural images from human brain activity. *Nature*. 452, 352-355.
- Kim, J. H., Shin, T., Kim, J. S., Kim, H. J. and Chung, S. H., 1996. MR imaging of cerebral activation performed with a gradient-echo technique at 1.5 T: sources of activation signals. *AJR Am J Roentgenol*. 167, 1277-1281.
- Koopmans, P. J., Manniesing, R., Niessen, W. J., Viergever, M. A. and Barth, M., 2008. MR venography of the human brain using susceptibility weighted imaging at very high field strength. *Magma*. 21, 149-158.
- Kriegeskorte, N., Cusack, R. and Bandettini, P., 2010. How does an fMRI voxel sample the neuronal activity pattern: Compact-kernel or complex spatiotemporal filter? *Neuroimage*. 49, 1965-1976.
- Kruger, G., Kastrup, A. and Glover, G. H., 2001. Neuroimaging at 1.5 T and 3.0 T: Comparison of oxygenation-sensitive magnetic resonance imaging. *Magnetic Resonance in Medicine*. 45, 595-604.
- Lai, S., Hopkins, A. L., Haacke, E. M., Li, D., Wasserman, B. A., Buckley, P., Friedman, L., Meltzer, H., Hedera, P. and Friedland, R., 1993. Identification of vascular structures as a major source of signal contrast in high resolution 2D and 3D functional activation imaging of the motor cortex at 1.5T: preliminary results. *Magn Reson Med*. 30, 387-392.
- LaManna, J. C., Chavez, J. C. and Pichiule, P., 2004. Structural and functional adaptation to hypoxia in the rat brain. *Journal of Experimental Biology*. 207, 3163-3169.
- Lee, J., Shahram, M., Schwartzman, A. and Pauly, J. M., 2007. Complex data analysis in high-resolution SSFP fMRI. *Magn Reson Med*. 57, 905-917.
- Levitt, M. H., 2001. Spin dynamics: basics of nuclear magnetic resonance. John Wiley &

- Sons Ltd, West Sussex, England.
- Li, D. B., Wang, Y. and Waight, D. J., 1998. Blood oxygen saturation assessment in vivo using T-2* estimation. *Magnetic Resonance in Medicine*. 39, 685-690.
- Logothetis, N. K. and Wandell, B. A., 2004. Interpreting the BOLD signal. *Annu Rev Physiol*. 66, 735-769.
- Mandeville, J. B. and Marota, J. J., 1999. Vascular filters of functional MRI: spatial localization using BOLD and CBV contrast. *Magn Reson Med*. 42, 591-598.
- McLachlan, G. J., 1992. *Discriminant Analysis and Statistical Pattern Recognition*. John Wiley & Sons, New York, N. Y.
- Menon, R. S., 2002. Postacquisition suppression of large-vessel BOLD signals in high-resolution fMRI. *Magn Reson Med*. 47, 1-9.
- Naselaris, T., Prenger, R. J., Kay, K. N., Oliver, M. and Gallant, J. L., 2009. Bayesian reconstruction of natural images from human brain activity. *Neuron*. 63, 902-915.
- Nencka, A. S. and Rowe, D. B., 2007. Reducing the unwanted draining vein BOLD contribution in fMRI with statistical post-processing methods. *Neuroimage*. 37, 177-188.
- Nishimura, D., 1996. *Principles of Magnetic Resonance Imaging*. Stanford University.
- Noll, D. C., Nishimura, D. G. and Macovski, A., 1991. Homodyne Detection in Magnetic-Resonance-Imaging. *Ieee Transactions on Medical Imaging*. 10, 154-163.
- Oakes, T. R., Johnstone, T., Ores Walsh, K. S., Greischar, L. L., Alexander, A. L., Fox, A. S. and Davidson, R. J., 2005. Comparison of fMRI motion correction software tools. *Neuroimage*. 28, 529-543.
- Ogawa, S. and Lee, T. M., 1990. Magnetic resonance imaging of blood vessels at high fields: in vivo and in vitro measurements and image simulation. *Magn Reson Med*. 16, 9-18.
- Ogawa, S., Menon, R. S., Tank, D. W., Kim, S. G., Merkle, H., Ellermann, J. M. and Ugurbil, K., 1993. Functional brain mapping by blood oxygenation level-dependent contrast magnetic resonance imaging. A comparison of signal characteristics with a biophysical model. *Biophys J*. 64, 803-812.
- Ogg, R. J., Langston, J. W., Haacke, E. M., Steen, R. G. and Taylor, J. S., 1999. The correlation between phase shifts in gradient-echo MR images and regional brain iron concentration. *Magn Reson Imaging*. 17, 1141-1148.
- Op de Beeck, H. P., 2010. Against hyperacuity in brain reading: Spatial smoothing does not hurt multivariate fMRI analyses? *Neuroimage*. 49, 1943-1948.
- Ordidge, R. J., Mansfield, P. and Coupland, R. E., 1981. Rapid biomedical imaging by NMR. *Br J Radiol*. 54, 850-855.
- Petridou, N., Schafer, A., Gowland, P. and Bowtell, R., 2009. Phase vs. magnitude information in functional magnetic resonance imaging time series: toward understanding the noise. *Magn Reson Imaging*. 27, 1046-1057.
- Pfeuffer, J., Van de Moortele, P. F., Ugurbil, K., Hu, X. P. and Glover, G. H., 2002. Correction of physiologically induced global off resonance effects in dynamic echo-planar and spiral functional imaging. *Magnetic Resonance in Medicine*. 47, 344-353.

- Pichiule, P. and Lamanna, J. C., 2002. Angiopoietin-2 and rat brain capillary remodeling during adaptation and deadaptation to prolonged mild hypoxia. *Journal of Applied Physiology*. 93, 1131-1139.
- Reddy, L. and Kanwisher, N., 2006. Coding of visual objects in the ventral stream. *Curr Opin Neurobiol*. 16, 408-414.
- Reichenbach, J. R., Barth, M., Haacke, E. M., Klarhofer, M., Kaiser, W. A. and Moser, E., 2000. High-resolution MR venography at 3.0 Tesla. *J Comput Assist Tomogr*. 24, 949-957.
- Reichenbach, J. R., Essig, M., Haacke, E. M., Lee, B. C., Przetak, C., Kaiser, W. A. and Schad, L. R., 1998. High-resolution venography of the brain using magnetic resonance imaging. *Magma*. 6, 62-69.
- Reichenbach, J. R. and Haacke, E. M., 2001. High-resolution BOLD venographic imaging: a window into brain function. *NMR Biomed*. 14, 453-467.
- Rowe, D. B., 2005. Modeling both the magnitude and phase of complex-valued fMRI data. *Neuroimage*. 25, 1310-1324.
- Rowe, D. B. and Logan, B. R., 2004. A complex way to compute fMRI activation. *Neuroimage*. 23, 1078-1092.
- Rowe, D. B., Meller, C. P. and Hoffmann, R. G., 2007. Characterizing phase-only fMRI data with an angular regression model. *J Neurosci Methods*. 161, 331-341.
- Schmithorst, V. J., Dardzinski, B. J. and Holland, S. K., 2001. Simultaneous correction of ghost and geometric distortion artifacts in EPI using a multiecho reference scan. *Ieee Transactions on Medical Imaging*. 20, 535-539.
- Shmuel, A., Chaimow, D., Raddatz, G., Ugurbil, K. and Yacoub, E., 2010. Mechanisms underlying decoding at 7 T: Ocular dominance columns, broad structures, and macroscopic blood vessels in V1 convey information on the stimulated eye. *Neuroimage*. 49, 1957-1964.
- Slichter, C. P., 1996. Principles of magnetic resonance. Springer - Verlag, Berlin.
- Smith, S. M., Jenkinson, M., Woolrich, M. W., Beckmann, C. F., Behrens, T. E. J., Johansen-Berg, H., Bannister, P. R., De Luca, M., Drobnjak, I., Flitney, D. E., Niazy, R. K., Saunders, J., Vickers, J., Zhang, Y. Y., De Stefano, N., Brady, J. M. and Matthews, P. M., 2004. Advances in functional and structural MR image analysis and implementation as FSL. *Neuroimage*. 23, S208-S219.
- Spiridon, M., Fischl, B. and Kanwisher, N., 2006. Location and spatial profile of category-specific regions in human extrastriate cortex. *Human Brain Mapping*. 27, 77-89.
- Stoquart-ElSankari, S., Lehmann, P., Villette, A., Czosnyka, M., Meyer, M. E., Deramond, H. and Baledent, O., 2009. A phase-contrast MRI study of physiologic cerebral venous flow. *Journal of Cerebral Blood Flow and Metabolism*. 29, 1208-1215.
- Thacker, N. A., Burton, E., Lacey, A. J. and Jackson, A., 1999. The effects of motion on parametric fMRI analysis techniques. *Physiol Meas*. 20, 251-263.
- Tsao, D. Y., Freiwald, W. A., Tootell, R. B. H. and Livingstone, M. S., 2006. A cortical region consisting entirely of face-selective cells. *Science*. 311, 670-674.
- Tsao, D. Y., Moeller, S. and Freiwald, W. A., 2008. Comparing face patch systems in

- macaques and humans. *Proc Natl Acad Sci U S A.* 105, 19514-19519.
- Turner, R., 2002. How much cortex can a vein drain? Downstream dilution of activation-related cerebral blood oxygenation changes. *Neuroimage.* 16, 1062-1067.
- van Gelderen, P., de Zwart, J. A., Starewicz, P., Hinks, R. S. and Duyn, J. H., 2007. Real-time shimming to compensate for respiration-induced B-0 fluctuations. *Magnetic Resonance in Medicine.* 57, 362-368.
- Vanduffel, W., Fize, D., Mandeville, J. B., Nelissen, K., Van Hecke, P., Rosen, B. R., Tootell, R. B. and Orban, G. A., 2001. Visual motion processing investigated using contrast agent-enhanced fMRI in awake behaving monkeys. *Neuron.* 32, 565-577.
- Vanzetta, I., Sloviter, H., Omer, D. B. and Grinvald, A., 2004. Columnar resolution of blood volume and oximetry functional maps in the behaving monkey: Implications for fMRI. *Neuron.* 42, 843-854.
- Wansapura, J. P., Holland, S. K., Dunn, R. S. and Ball, W. S., 1999. NMR relaxation times in the human brain at 3.0 tesla. *Journal of Magnetic Resonance Imaging.* 9, 531-538.
- Weibull, A., Bjorkman, A., Hall, H., Rosen, B., Lundborg, G. and Svensson, J., 2008. Optimizing the mapping of finger areas in primary somatosensory cortex using functional MRI. *Magn Reson Imaging.* 26, 1342-1351.
- Weisskoff, R. M. and Kiihne, S., 1992. MRI susceptometry: image-based measurement of absolute susceptibility of MR contrast agents and human blood. *Magn Reson Med.* 24, 375-383.
- Weisskoff, R. M., Zuo, C. S., Boxerman, J. L. and Rosen, B. R., 1994. Microscopic susceptibility variation and transverse relaxation: theory and experiment. *Magn Reson Med.* 31, 601-610.
- Woolrich, M. W., Jbabdi, S., Patenaude, B., Chappell, M., Makni, S., Behrens, T., Beckmann, C., Jenkinson, M. and Smith, S. M., 2009. Bayesian analysis of neuroimaging data in FSL. *Neuroimage.* 45, S173-S186.
- Woolsey, T. A., Rovainen, C. M., Cox, S. B., Henegar, M. H., Liang, G. E., Liu, D. Q., Moskalenko, Y. E., Sui, J. and Wei, L., 1996. Neuronal units linked to microvascular modules in cerebral cortex: Response elements for imaging the brain. *Cerebral Cortex.* 6, 647-660.
- Yacoub, E., Harel, N. and Ugurbil, K., 2008. High-field fMRI unveils orientation columns in humans. *Proc Natl Acad Sci U S A.* 105, 10607-10612.
- Yacoub, E., Shmuel, A., Logothetis, N. and Ugurbil, K., 2007. Robust detection of ocular dominance columns in humans using Hahn Spin Echo BOLD functional MRI at 7 Tesla. *Neuroimage.* 37, 1161-1177.
- Yacoub, E., Shmuel, A., Pfeuffer, J., Van de Moortele, P. F., Adriany, G., Andersen, P., Vaughan, J. T., Merkle, H., Ugurbil, K. and Hu, X. P., 2001. Imaging brain function in humans at 7 Tesla. *Magnetic Resonance in Medicine.* 45, 588-594.
- Yovel, G. and Kanwisher, N., 2004. Face perception: domain specific, not process specific. *Neuron.* 44, 889-898.
- Zheng, D., LaMantia, A. S. and Purves, D., 1991. Specialized vascularization of the primate visual cortex. *J Neurosci.* 11, 2622-2629.


UCSF Library Release

Publishing Agreement

It is the policy of the University to encourage the distribution of all theses, dissertations, and manuscripts. Copies of all UCSF theses, dissertations, and manuscripts will be routed to the library via the Graduate Division. The library will make all theses, dissertations, and manuscripts accessible to the public and will preserve these to the best of their abilities, in perpetuity.

Please sign the following statement:

I hereby grant permission to the Graduate Division of the University of California, San Francisco to release copies of my thesis, dissertation, or manuscript to the Campus Library to provide access and preservation, in whole or in part, in perpetuity.

	2/28/2011
_____ Author Signature	_____ Date